MECHANICS AND CHARGING OF NANOPARTICLE AGGLOMERATES

A DISSERTATION
SUBMITTED TO THE FACULTY OF THE GRADUATE SCHOOL
OF THE UNIVERSITY OF MINNESOTA
BY

WEON GYU SHIN

IN PARTIAL FULFILLMENT OF THE REQUIREMENTS
FOR THE DEGREE OF
DOCTOR OF PHILOSOPHY

Dr. David Y. H. Pui, Adviser

June 2009

Acknowledgements

I would like to express my warmest gratitude to my advisor Dr. David Y. H. Pui for his patience, support, generosity, and guidance throughout my PhD study at the University of Minnesota. He is a great scientist, engineer, instructor, and leader. Due to his supports, the time spent in my pursuit for PhD degree has been the most productive and learning experience of my life.

I would like to sincerely thank Prof. Heinz Fissan and Prof. George W. Mulholland for helping me address numerous theoretical and experimental challenges throughout this study. Their consitent supports, insight, knowledge, and experience are invaluable in carrying out this research.

I also would like to sincerely thank Prof. Peter H. McMurry for his allowing me to use Aerosol Particle Mass (APM) analyzer for my experiments. I am also grateful to the examination committee: Prof. Jeffrey T. Roberts, Prof. Uwe Kortshagen, and Prof. Trian Dumitrica for their invaluable comments.

Thanks to all my colleagues in the Particle Thechnology Laboratory and Mechanical engineering for their help. Special thanks go to Drs. Seong Chan Kim, Jing Wang, Chaolong Qi and Kenjiro Iida for their help with comments, Jacob Scheckman for his help with APM, and Nick Stanley for his help with English correction of my writings. I also thank Bob Nelson and Robin Russell in ME machine shop for their help, Drs. John Nelson, Ozan Ugurlu, and Bob Hafner in the Characterization Facility for their helpful comments, and Maynard Havlicek in TSI, Inc for his help with fixing instruments.

I gratefully acknowledge the Department of Mechanical Engineering at the University of Minnesota, Center for Filtration Research at the University of Minnesota, TSI, Inc, and the Chemical Company BASF SE, Germany for financial support for my PhD course. I also acknowledge the University of Minnesota Graduate School for Doctoral Dissertation Fellowship during 2008-2009.

I am grateful to David Mekala, Daniel Johnson, Chene Malek, and Howard Reitz for their friendship and prayers while staying in Minnesota. I also thank Yuseung Choi, Ki-Joong Kim, Jungkeun Lee, and Dr. Young Lae Kim for their cheers.

In addition to these, I cannot thank my family enough for their support, which has been the best. I would like to express my deepest gratitude to my wife, Sejin Choi and my son, Jonghyun for their sacrifice and encouragements. Whether good or bad, they have always been together with me and a strong motivation for the completion of my PhD degree. I also sincerely acknowledge my parents and parents-in-law for their continuous prayers and all the supports to complete this course successfully. I also sincerely thank my two brothers, two brothers-in-law, and four sisters-in-law, my grandmother, and relatives for their cheers and prayers.

Above all, I would like to thank my Lord and Savior, Jesus Christ. He is my loving God and my fortress, my stronghold and my deliverer, and my shield.

To my lovely wife and son

Abstract

This thesis consists of two parts. The first part concerns studies on mechanics of real agglomerate particles and the second part involves studies on unipolar diffusion charging of agglomerates.

Understanding mechanics of real agglomerate particles consisting of multiple primary particles is important for aerosol sizing instrumentation using electrical mobility and nanoparticle manufacturing process where coagulation and sedimentation occur. A key quantity determining transport properties of agglomerates is the friction coefficient. However, quantitative studies for the friction coefficient of agglomerates are very limited. Transmission Electron Microscopy (TEM) image analysis results of silver agglomerates provides a basis for the comparison of experimental data with estimates based on free molecular models. A new quantitative method to determine the dynamic shape factor and the two exponents, η and D_{fm}, which characterize the power law dependence of friction coefficient on the number of primary spheres and the mass on the mobility diameter, was developed using Differential Mobility Analyzer (DMA)-Aerosol Particle Mass (APM) analyzer. Model predictions indicate that η is independent of agglomerate size while D_{fm} is sensitive to agglomerate size. Experimentally, it appears the opposite is true. Tandem DMA (TDMA) results also show that the mass-mobility diameter scaling exponent is not dependent on mobility size range. Estimates of non-ideal effects on the agglomerate dynamics were computed as perturbations to the

Chan-Dahneke agglomerate model. After the corrections, an agreement between experimental data and model predictions becomes significantly improved.

Unipolar diffusion charging becomes more attractive because it has higher charging efficiency than bipolar charging as well as important applications in aerosol sizing instrumentation using electrical mobility, powder coating, and the removal of toxic particles from air stream using Electrostatic Precipitator. It has been reported that the particle morphology affects both bipolar and unipolar charging processes. Nevertheless, knowledge about the charging of non-spherical particles such as asbestos fibers and fractal agglomerates is still lacking. From this study it was found that the effect of dielectric constant of materials on unipolar diffusion charging of nanoparticles is very small and the experimental results are in a good agreement with Fuchs (1963)' theory. The effect of agglomerate morphology on unipolar charging characteristic was examined both experimentally and analytically in terms of the mean charge per particle. Both geometric surface area and electrical capacitance are known as two important parameters to determine the mean charge of non-spherical particles. A new model to predict the electrical capacitance of loose agglomerate particles as a function of mobility diameter was developed incorporating electrical mobility and electrostatics theories. This study shows that the electrical capacitance contributes to increase the mean charge per particle of agglomerates more than the geometric surface area, especially in the transition regime. The estimates of geometric surface area and electrical capacitance were used to predict the mean charge from Chang (1981)'s model and the predicted results are reasonably in good agreement with experimental data.

Table of Contents

List of Tables

List of Figures

Nomenclature

a	radius of particle
a_s	radius of the minor axis of the prolate spheroids
A_a	projected area of the agglomerate
A_f	a constant
A_1 , A_2, A_3	slip correction factor constants
A_p	mean projected area of primary particles
c_{bcu}^{a}	dimensionless friction coefficient for a basic chain unit if the chain is aligned in the direction of the chain motion
c_{bcu}^{r}	dimensionless friction coefficient for a basic chain unit if the chain is randomly oriented
C_c	Cunningham slip correction factor
CF	calibration factor of NSAM in $\mu m^2/(cm^3 * pA)$
C_p	electrical capacitance in C^2/N-m
c^*	dimensionless drag force
d_{cy}	diameter of cylinder
D_f	fractal dimension
D_{fL}	fractal-like dimension based on the maximum projected length (L)
D_{fm}	mass-mobility diameter scaling exponent
D_i	ion diffusion coefficient
DS	particle surface area deposited in human lung
d_{co}	diameter of coalesced particle
d_m	mobility diameter
d_{mi}	initial mobility diameter
d_{mp}	mobility diameter for the polydisperse particles
d_{m2}	mobility diameter of the agglomerate measured by the second DMA
d_p	primary particle diameter
$\overline{d_p}$	mean primary particle diameter

d_p (N)	size dependent primary size
d_{pa}	projected area equivalent diameter
d_{pc}	constant primary sphere size
D_v	diffusion coefficient of a mixture of silver vapor and nitrogen
d_{vep}	volume equivalent diameter for the polydisperse particles
e	elementary charge of unit ($e = 1.6 \times 10^{-19}$ coulomb)
f	friction coefficient
f_{Meakin}	friction coefficient based on Meakin's expression
f_{21}	ratio of the number concentration of doubly charged to singly charged particles for agglomerates with mobility diameter d_{m2} exiting a bipolar charger
f_0	friction coefficient for a constant primary sphere size
f_r	fraction of molecules diffusely reflecting from the particle surface
F_d	drag force
F_f	filling factor
F_i	ion particle interaction force
F_1	fraction of singly charged particles exiting for DMA size d_{m1}
$G(m)$	mass at the peak in the size distribution exiting the DMA
I_e	electrical current
k	the Boltzmann's constant
k_l	Lagrangian multiplier
k_a	an empirical constant
K_E	conversion factor between cgs unit and SI unit ($=1/(4\pi\varepsilon_o)$)
k_g	prefactor
k_m	prefactor
k_{m1}	prefactor
Kn	Knudsen number
Kn_{ion}	Knudsen number of ions
Kn_p	Knudsen number based on primary diameter
Kn_R	Knudsen number based on radius of gyration

L	maximum projected length of an agglomerate
$\bar{L}$	column length of DMA
L_{cy}	length of cylinder
m	particle mass, fg
M	molecular mass of silver
m_g	mass of a gas molecule
N	number of primary particles on an agglomerate
n_{box}	number of non-overlapping equal boxes
N_c	normalized capacitance
N_i	ion concentration
N_{in}	particle number concentration at the inlet of NSAM
N_m	ratio of the mass of the agglomerate to the mass of a primary sphere
N_u	number concentration of uncharged particles downstream of the charger
$N_o(V_1)$	APM output number concentration at voltage V_1
N_1	number concentration including singly and doubly charged particles
N_2	number concentration including only doubly charged particles
N_T	total number concentration of particles
N_p	mean charge per particle in elementary charge unit
n_g	number density of gas molecules
NS	normalized sensitivity of NSAM
N_{UCPC}	particle number concentration measured by UCPC
N_0	number of primary particles for d_{pc}
N_v	number of primary particles for d_p (N)
P	a normal distribution function with mean $\bar{d}_p$ and standard deviation σ
P_d	partial pressure of vapor at the particle surface
P_∞	partial pressure of vapor well away from the particle surface
Q_i	electrical charge on i_{th} primary particle
Q_{in}	total flow rate (2.5 lpm) entering into the inlet of NSAM,
Q_{sh}	sheath flow rate of DMA
Q_{tot}	total charge on an agglomerate

Q_{UCPC}	flow rate (1.5 lpm) entering into the inlet of UCPC
r	distance from the center of a particle
r_1 , r_2	radii of the inner and outer electrodes of APM
$\overline{r_1}$, $\overline{r_2}$	inner and outer radii of annular space of DMA
r_c	average of radii of the inner and outer electrodes of APM
R	gas constant
Re	Reynolds number
R_g	radius of gyration of the agglomerate
R_m	mobility radius
R_{ve}	radius of volume equivalent sphere
S	size dependent sensitivity of NSAM
S_{ag}	geometric surface area of an agglomerate
s_c	mass to charge ratio of particle at r_c
S_p	geometric surface area of particle
S_{pa}	projected area of an agglomerate
$S_{pa,\,r}$	reduced projected cross section averaged over three orthogonal orientations
S_{sph}	geometric surface area of a sphere
t	residence time in the ion environment
T_d	particle temperature
T_∞	ambient temperature
u	uncertainty
v	particle sedimentation velocity
$\bar{v}$	ion mean thermal velocity
V	voltage applied to APM electrode
$\overline{V}$	electrical voltage applied to DMA
V_p	electric potential
v_g	average speed of the gas molecules
W	maximum projected width of an agglomerate
Z	electrical mobility

Greek symbols

α	power exponent representing the dependence of primary sphere size on N in the agglomerate
β	aspect ratio of agglomerate (= L/W)
β_c	combination coefficient of ions and particles
β_{c0}	combination coefficient between ions and uncharged particles
β_s	aspect ratio of spheroids
δ	power exponent characterizing the friction coefficient of agglomerates and mobility diameter
δ_{box}	box size
Δ_D	change in mass-mobility diameter scaling exponent ($= D_{fm}(after) - D_{fm}(before)$)
Δ_η	change in η ($=\eta(after) - \eta(before)$)
δP_∞	total momentum transfer
ε	dielectric constant
ε_0	permittivity of vacuum
η	power exponent characterizing the friction coefficient of agglomerates and number of primary particles
η_i	intrinsic charged fraction of particles
$\eta_l\,(d_m)$	particle lung deposition efficiency in TB or A
$\eta_{charger}\,(d_m)$	charger chamber penetration efficiency of particles in NSAM.
$\eta_{tot}(d_m)$	total particle penetration efficiency in NSAM
$\eta_{flowpath}(d_m)$	flow path penetration efficiency
η_{TB} and η_A	deposition efficiencies in TB and A regions
γ	slope in box counting method (=$1-D_f$)
κ	dynamic shape factor
κ_E	experimental dynamic shape factor
κ_R	mobility radius dynamic shape factor

$\kappa_v/\ \kappa_0$	ratio of the dynamic shape factor of the size dependent to constant primary sphere size
λ	mean free path of gas, nm
λ_i	mean free path of the ions, nm
μ	viscosity of gas
$\phi(r)$	interaction potential at a distance r from the center of a particle
ϕ_F	Fuchs correction factor
φ_p	the nondimensional potential
Φ_i	pairwise interaction electrostatic energy of i_{th} primary sphere
Φ_s	self energies of all the spheres in the agglomerate
ρ	density of silver
ρ_b	bulk density of material
θ	angle between the polar axis of cylinder and flow direction
ω	rotation frequency
σ	standard deviation
σ_p	projected area of an agglomerate

Abbreviations

A	alveolar
aggl.	agglomerate
APM	aerosol particle mass analyzer
bcu	basic chain unit
CV	coefficient of variation equal to the standard deviation divided by the average
deg	degree
DMA	differential mobility analyzer
DOS	dioctyl sebacate
func	function
EAD	electrical aerosol detector
ESP	electrostatic precipitator
I. D.	inner diameter
J	Joule
lpm	liter per minute
NP	nanoparticle
NSAM	nanoparticle surface area monitor
PSL	polystyrene latex
sph.	sphere
SEM	scanning electron microscopy
3-D	three dimensional
TB	trancheobronchial
TDMA	tandem DMA
TEM	transmission electron microscopy
2-D	two dimensional
UCPC	ultra condensation particle counter
ve	volume equivalent sphere for an agglomerate

Chapter 1 Introduction

Nanoparticle agglomerates are pervasive in atmospheric sciences, air pollution, and material manufacturing. Combustion processes are used to manufacture a variety of materials in agglomerate form including fumed silica (Okuyama, 1986) and titanium dioxide (Pratsinis, 1998). Measurement of agglomerate particles is an important area of current aerosol research (Friedlander and Pui 2004).

This thesis consists of two parts. The first part is on the relationship between agglomerate structure and transport properties of agglomerates. In the second part, the effect of particle morphology on unipolar diffusion charging is investigated. The first and second parts are related to each other because the mechanics and charging properties of aerosol particles are correlated with the mobility equivalent diameter (Rogak and Flagan, 1992).

1-1. Mechanics of agglomerates

Physical properties of aerosol particles such as particle mobility and mass are essential to describe aerosol transport behaviors in the ambient air, aerosol manufacturing process, and aerosol sizing instrumentation using electrical mobility. Aerosol transport mechanics includes the processes of particle diffusion, sedimentation, electrical mobility, thermophoresis, and coagulation. A key quantity in computing all of these properties is the friction coefficient (f). It is defined as the drag force (F_d) exerted by the fluid on the particle as it moves at a constant velocity (v) through the

fluid divided by the velocity.

For spherical particles with a low Reynolds number ($Re < 1$), the friction coefficient is accurately known by the Stokes's law. Many aerosol instruments for small particles, including the Differential Mobility Analyzer (DMA) and diffusion battery, depend upon this expression for the measurement of particle size. Particles without a spherical shape have pronounced effects on particle sizing methods. An agglomerate has a larger drag force compared to a spherical particle with the same volume (Kousaka et al. 1996; Park et al. 2004a; Song et al. 2005; Zelenyuk and Imre 2007).

Previous studies (Park et al., 2004a; Park et al., 2004b, Lall et al., 2008) have not investigated the relationship between the friction coefficient of an agglomerate and the number of primary particles on an agglomerate. Park et al. (2004a, 2004b) used diesel emission particles as their test material for the study of the relationship between mass and mobility diameter. Diesel emission particles have a volatile component and they have no intrinsic density. Thus, it is not possible to estimate the number of primary particles from the measured mass of the diesel emission particles even though a primary particle size is determined by Transmission Electron Microscopy (TEM). In this thesis, silver agglomerate is used as a test material. This provides estimates of the number of primary particles from the measured mass or volume with a primary particle size determined by TEM.

It is of interest to make use of analytical models to predict structural and dynamic properties of nanoparticle agglomerates such as dynamic shape factor κ, friction coefficient f, number of primary particles N, and mass-mobility diameter scaling exponent D_{fm}. Chan and Dahneke (1981), Meakin et al. (1989), and Mackowski (2006)

have obtained the friction coefficient of agglomerate particle consisting of many primary spheres by doing numerical simulations. However, there are several characteristics of real agglomerates that are not incorporated in existing models for agglomerate dynamics. They include necking between primary particles, polydispersity of primary particles, and the particle alignment in the electric field of DMA. Those analytical models assume that agglomerates are in the free molecular regime. However, agglomerate particles are more likely to be in the transition regime, i.e., the mobility diameter d_m > 100 nm.

The first objective of this study is to characterize structural properties of nanoparticle agglomerates and relate the results to a mobility analysis. In order to characterize the silver agglomerates, an intensive TEM analysis is conducted.
The second objective of this study is to obtain quantitative data on the friction coefficient of nanoparticle agglomerates as a function of the agglomerate size with primary spheres in the free molecular regime. The friction coefficient of agglomerates is measured by DMA and the mass and volume of the agglomerates are measured using DMA-Aerosol Particle Mass analyzer (APM) and tandem DMA (TDMA), respectively. The number of primary particles is estimated from the measured mass (or volume) with the information about the primary particle size. The third objective of this study is to compare the measured results with free molecular based model predictions. The fourth objective of this study is to characterize the non-ideal effects experimentally and to estimate three non-ideal effects as perturbations to a free molecular based model, Chan and Dahneke model.

1-2. Charging of agglomerates

Diffusion charging has become one of the most commonly used methods for charging aerosol particles. The phenomenon is of significant interest in aerosol measurement science when electrical mobility analysis is used. The process can be characterized as unipolar or bipolar depending on the polarity of ions in the gas. Unipolar diffusion charging has become more attractive than bipolar diffusion charging because the former has a higher charging efficiency than the latter (Chen and Pui, 1999). Also, unipolar diffusion charging of aerosol particles has many applications in the removal of toxic aerosol particles from aerosol flow stream, powder coating, and aerosol sizing instrumentation using electrical mobility.

The diffusion charging process is determined by the Knudsen number of ions, Kn_{ion}, defined as the ratio of the mean free path of ions λ_i to the particle radius:

$$Kn_{ion} = \frac{\lambda_i}{a}. \tag{1-1}$$

In the continuum regime ($Kn_{ion} \rightarrow 0$), the diffusion charging is well described by the diffusion-mobility theory, which is based on the solution of the continuous diffusion equation for ions in the electric field of a charged particle (Fuchs, 1963). For the transition regime ($0.1 < Kn_{ion} < 10$) and free molecule regime ($Kn_{ion} \rightarrow \infty$), the situation is much more complex. A great number of independent theories have been reported.

Most diffusion charging theories (White 1951; Gunn 1954; Fuchs, 1963; Liu et al. 1967; Gentry 1972; Pui 1976; Liu and Pui 1977; Pui et al. 1988) assuming spherical particles has been widely and successfully used to describe the process. However, several previous studies (Rogak and Flagan, 1992; Laframboise and Chang, 1977;

Chang, 1981) showed that both unipolar and bipolar diffusion charging processes can be affected by particle morphology in both theoretical and experimental ways. Using 3-D Monte-Carlo model Biskos et al. (2004) showed that rectangular shaped and elongated chain-aggregate particles show different charging behavior compared to theoretical predictions based on Fuchs (1963), Laframboise and Chang (1977), and Chang (1981). The abovementioned difference between measured charge quantity and predictions requires a more sophisticated analysis.

The first objective of this study is to examine the material effect on unipolar diffusion charging of particles. In order to assess this issue, tested nanoparticles (10 – 200 nm) are selected to cover a wide range of dielectric constant but have almost the same spherical or compact morphology. The unipolar charger used in this study has been installed in several commercial aerosol instruments. The charger has negligible particle loss, which enables the measured charging properties in this study to be compared with existing diffusion charging theory. The second objective of this study is to investigate the effect of particle morphology on unipolar diffusion charging in both experimental and analytical ways. Laframboise and Chang (1977) and Chang (1981) indicated that the geometric surface area and electrical capacitance are two important morphology-related parameters which determine charging properties of non-spherical particles. For the experiments, two different types of particles, i.e., compact spheres and branched chain agglomerates are used. Also, the geometric surface area is estimated from a mobility analysis. A new analytical model based on Lall and Friedlander (2006) and Brown and Hemingway (1995) is developed to estimate the electrical capacitance of branched chain agglomerates.

1-3. Thesis outline

As mentioned above, the thesis consists of two parts. The first part, regarding the study of mechanics of agglomerates, consists of Chapters 2, 3, 4, 5, and 6. The second part, which concerns the study of the effect of agglomerate morphology on the unipolar diffusion charging of agglomerates, is discussed in Chapters 7 and 8. Figure 1-1 shows a schematic diagram for structure of this thesis.

Chapter 2 presents a Transmission Electron Microscopy (TEM) analysis of the structural properties of silver nanoparticle agglomerates generated using a condensation and evaporation method in an electric tube furnace followed by a coagulation process. The projected area, fractal dimension (or mass-mobility diameter scaling exponent), and number of primary particles obtained from TEM images are compared with a free molecular model, i.e., Lall and Friedlander (2006). The results in Chapter 2 also show that silver agglomerates used in this study are cluster-cluster agglomerate, which enables DMA-Aerosol Particle Mass analyzer (APM) data to be compared with another free molecular model, Meakin et al. (1989). This analysis is presented in Chapters 3, 4, and 5.

Dynamic shape factor of agglomerate particle is defined as the friction coefficient of an agglomerate divided by that of a volume equivalent sphere. Chapter 3 presents a quantitative method to measure the dynamic shape factor using DMA-APM method. This method provides characterization of nearly monodisperse agglomerates and can be used to analyze thousands of particles over a ten minute period. A

quantitative uncertainty analysis is also presented. Chapter 3 also presents the exponent η which characterizes the power law dependence of friction coefficient f on the number (N) of primary spheres. The power law relationship is expressed as $f = A_f N^{\eta}$ where A_f is a constant. The experimentally determined dynamic shape factor and the exponent η are compared with those obtained based on free molecular analysis.

Chapter 4 presents mass-mobility diameter scaling exponent (D_{fm}) which characterizes the relationship between mass (m) and the mobility diameter (d_m) of agglomerate particles using DMA-APM method. The power law relationship is expressed as $m = k\left(\frac{d_m}{d_p}\right)^{D_{fm}}$, where k is a prefactor and d_p is primary particle diameter. A quantitative uncertainty analysis is also performed. The experimentally determined mass-mobility diameter scaling exponent is compared with that obtained based on free molecular analysis.

In Chapter 5, estimates are made for the following effects: particle alignment in the electric field, necking between particles, polydispersity of the primary particles, and variable primary sphere size. These effects are not included in the models used in Chapters 2-4. The estimates were computed as perturbations to the Chan-Dahneke agglomerate model.

It is of interest to compare DAM-APM results for agglomerates with another independent method. In Chapter 6, TDMA methods are used to obtain volume and mass-mobility diameter scaling exponent of agglomerates and compare with DMA-APM data. Also, the particle alignment is investigated using TDMA method and the

result is compared with a cross model presented in Chapter 5. Possibilities of partial evaporation and thermal recharging of particles are discussed.

In Chapter 7, the effect of dielectric constant of materials on unipolar diffusion charging of nanoparticles is experimentally investigated. The examined nanoparticles (10 – 200 nm) cover a wide range of dielectric constants but have almost the same spherical or compact morphology. Measurement results for both intrinsic charged fraction and mean charge per particle are compared with the estimates based on Fuchs (1963)' theory.

In Chapter 8, the effect of agglomerate morphology on unipolar diffusion charging of nanoparticles is presented. The mean charge per particle for both silver agglomerates and sintered spheres is evaluated and compared with diffusion charging theories. From a diffusion charging theory (Chang, 1981), one can find that the geometric surface area and electrical capacitance of an agglomerate are two important key parameters which are related to particle morphology. In this chapter, the estimates of the geometric surface area and electrical capacitance of an agglomerate are made with a newly developed model based on the combination of Lall and Friedlander (2006)'s and Brown and Hemingway (1995)'s models.

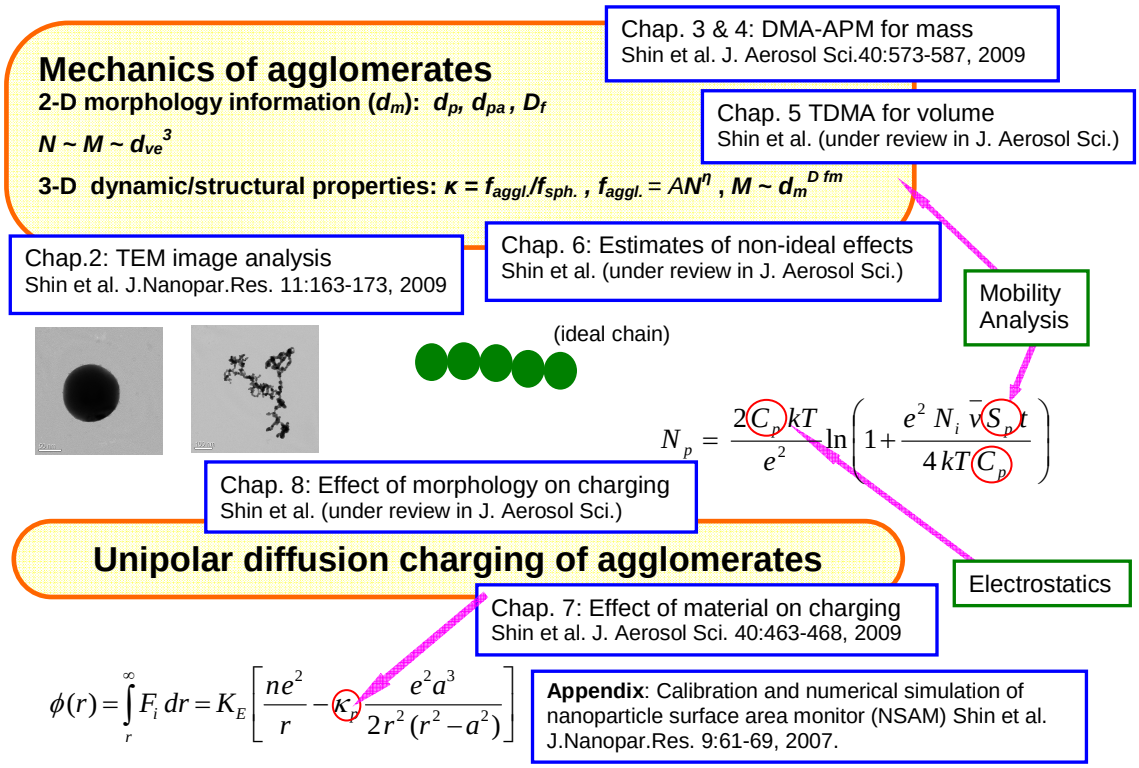

Figure 1-1. Structure of thesis

Chapter 2 Structural Properties of Agglomerates Based on TEM Analysis: Relationship to Mobility Analysis

2-1. Introduction

Agglomerate particles often have a fractal structure which can be represented with Eq. (2-1) given by Mandelbrot (1982):

$$N = k_g \cdot \left(2R_g / d_p\right)^{D_f}, \tag{2-1}$$

where N is the number of primary particles in an agglomerate, R_g is the radius of gyration of the agglomerate, d_p is the primary particle diameter, and D_f is fractal dimension. As one extreme case, one can consider loose agglomerates with a transparent structure and no necking between primary particles.

In order to describe the properties of agglomerates more in detail, one can consider several parameters. First of all, one can consider an intrinsic parameter, the density (ρ_b) of the bulk material. Secondly, one can consider chainlike agglomerate parameters such as number of primary particles (N) and primary particle diameter (d_p) in a fractal agglomerate. Thirdly, one can consider morphology parameters such as the fractal dimension and dynamic shape factor. Finally, one can take account of equivalent diameters. An equivalent diameter is defined as the diameter of a sphere having the

same behavior in a physical process of an agglomerate or having the same property like mass or surface area as an agglomerate.

Transmission Electron Microscopy (TEM) has been used to image agglomerates and derive the fractal dimension, projected area, primary particle size, and aspect ratio. (Cai et al., 1993; Koylu et al., 1995; Neimark et al. 1996; Park et al. 2004a; Rogak et al. 1993; Samson et al., 1987; Wentzel et al., 2003). Rogak et al. (1993) showed that the projected area equivalent diameters of TiO_2 and Si agglomerates are nearly equal to mobility diameters for particles with mobility diameters up to 400 nm. Park et al. (2004a) also showed that it applies to diesel agglomerates consisting of primary particles with the mean diameter of 31.9 nm in the mobility diameter range of 50 to 220 nm. Oh et al. (2004) showed that the projected area equivalent diameter does not change depending on particle shape if particles have the same mobility diameter. Using numerical simulations, Brasil et al. (1999) showed that the projected area and length can be overestimated in the 2-D projection depending on the resting position of the agglomerate and how many contact points the agglomerate has established with the substrate. Additionally deriving the fractal dimension of 3-D particles from 2-D images is limited by the inability to distinguish 3-D agglomerates with $2 < D_f < 3$ (Katrinak et al., 1993; Tence et al., 1986).

In this chapter, structural properties of silver agglomerates are investigated using TEM. Silver agglomerates generated by evaporation and condensation followed by coagulation process are preclassified by a Differential Mobility Analyzer (DMA) and sampled agglomerates are imaged by TEM.

This chapter is focused on obtaining structural properties including the projected area equivalent diameter, 2-D fractal dimension, and number of primary particles of silver agglomerates. For the case of a loose and transparent agglomerate, the projected area equivalent diameter (d_{pa}) can be expressed as:

$$d_{pa} = \sqrt{N} d_p \quad \text{from } S_{pa} = \pi d_{pa}^2 / 4 = N \pi d_p^2 / 4, \tag{2-2}$$

where S_{pa} is the projected area of an agglomerate. Those properties obtained from the projected image of an agglomerate can be also used to estimate the surface area, volume, and dynamic shape factor of agglomerates. The projected area equivalent diameter (d_{pa}), fractal dimension (D_f), and number of primary particles (N) of silver agglomerates obtained from TEM images is compared with those obtained from mobility analysis using Lall and Friedlander (2006). The Lall and Friedlander (2006)'s model is discussed more in detail in the section Results and Discussion.

2-2. Experimental

Silver primary particles were generated by evaporation and condensation method developed by Scheibel and Porstendorfer (1983) with silver powder (99.999%, Johnson Mattney Electronics) within an electric tube furnace. A schematic diagram for experimental set-up is shown in Figure 2-1. Silver agglomerates were produced by having primary particles pass through an agglomeration chamber to increase the residence time needed for coagulation. Nitrogen was used as carrier gas. The reactor conditions for the particle generation are summarized in Table 2-1. The particle

generation system was very stable during the experiments. Particle concentration at the peak varied within 20 % and the peak location was changed by a few nanometers. The standard deviation of size distribution varied within 15 %. Silver agglomerates were classified by DMA (Model 3081, TSI, Inc.) with sheath flow rate of 15 lpm and aerosol flow rate of 1.5 lpm and then sampled with a Nanometer Aerosol Sampler (Model 3089, TSI, Inc.) which uses electrostatic force for the collection of charged particles leaving the DMA.

2-3. Results and discussion

2-3-1. Basic properties of projected silver agglomerates

Properties of projected monodisperse silver agglomerates are measured, and reported here. TEM measurements of agglomerates include the primary particle size (d_p), maximum projected length (L), maximum projected width (W), and derived aspect ratio (L/W) as shown in Figure 2-2 (a). These measurements were done with the aid of two pieces of image analysis software, Digital Micrograph 3, Gatan Inc. and ImageJ with the plug-in FracLac_2003K.

The particle in the Figure 2-2 on the left does not match the several assumptions made by Lall and Friedlander (2006) which may cause a deviation from experimental result: (1) It is not a chainlike agglomerate (2) It is not a loose (“neckless”) agglomerate. Neck formation can occur in silver agglomerates (Weber and Friedlander, 1997; Lall et al., 2006). In order to measure primary particle size, a circle was drawn on

each primary particle with a distinct boundary as shown in Figure 2-2 (a). (3) Primary particles are polydisperse as can be seen in Figure 2-2 (b). The measured average primary sphere diameter of silver agglomerates is 13.8 nm with a standard deviation of 2.5 nm as shown in Figure 2-2 (b). It is well fitted with a Gaussian distribution function. Previous studies showed that the primary particle size of silver agglomerates in diameter is 15 nm in Schmidt-Ott (1988), 18.5 nm in Lall et al. (2006).

2-3-2. The effect of a tilting angle of TEM specimen holder on TEM analysis

In this section, the effect of a tilting angle of TEM holder on TEM analysis result is investigated. Figure 2-3 shows TEM images of only one agglomerate with d_m = 120 nm viewed at different tilting angles of the TEM specimen holder. The TEM images (b) and (d) look strikingly different from each other. The projected area equivalent diameter, maximum length, aspect ratio, and fractal dimension are summarized in Table 2-2 as a function of the tilting angle.

The projected area equivalent diameter was obtained using the ImageJ software. The original TEM image was binarised by selecting brightness thresholds. From the binarised TEM images, the projected area was measured. The projected area equivalent diameter is smaller than the mobility diameter. Due to the different tilting angles of the TEM specimen holder, there is a difference of 10.3 nm in projected area equivalent diameter between image (b) and image (d). Maximum projected length and aspect ratio of image (b) and image (d) are significantly different from each other while there is almost no difference in fractal dimension measured using a box counting algorithm in

ImageJ software for the two images (b) and (d). The method to determine the fractal dimension is discussed later more in detail. In this study, those biased effects due to the tilting angle were minimized by analyzing many TEM image samples randomly and taking the average value.

2-3-3. Projected area equivalent diameter vs. mobility diameter

Figure 2-4 shows the projected area equivalent diameter distribution of silver agglomerates with d_m = 120 nm together with representative TEM images corresponding to different projected areas. The mobility diameter of doubly charged particles corresponding to d_m = 120 nm is 180 nm. The projected equivalent diameter was determined from the bin of the maximum count observed in the distribution. The projected area equivalent diameter is 110 nm for singly charged particles and 160 nm for doubly charged particles, respectively.

The projected area equivalent diameters corresponding to mobility sizes are summarized in Table 2-3. The projected area equivalent diameter is slightly smaller than the mobility diameter for both singly charged and doubly charged as shown in Table 2-3. Using Lall and Friedlander (2006), one can estimate the projected area equivalent diameter with the information about the primary particle diameter (d_p). Lall and Friedlander (2006) related the number of primary particles, N, to mobility size d_m using Stokes-Einstein equation and Chan and Dahneke's model (1981) as follows:

$$F_d = c^* N \mu \frac{d_p}{2} v / Kn = \frac{3\pi \mu v d_m}{C(d_m)}, \quad (2\text{-}3)$$

where F_d is the drag force exerted on an agglomerate, c^* is the dimensionless drag force, μ is the viscosity of gas, v is the sedimentation velocity in an electric field, Kn is the Knudsen number, and $C_c\ (d_m)$ is the Cunningham slip correction factor. From Eq. (2-3), the number of primary particles is given as:

$$N = \frac{d_m}{C_c(d_m)} \frac{c^* d_p^2}{12\pi\lambda}, \quad (2\text{-}4)$$

where λ is the mean free path of gas.

Figure 2-5 compares the projected area equivalent diameter obtained from TEM images for d_m = 80 nm, 120 nm, and 150 nm with that predicted from Lall and Friedlander (2006) for the same mobility sizes with mean primary particle diameter, d_p = 13.8 nm from TEM measurement. A linear fitting of the experimental data shows that the measured projected area equivalent diameter, d_{pa}, is equal to 0.92 ± 0.03 d_m, rather than $d_{pa} = d_m$. The best fit of predicted projected area diameter from Lall and Friedlander (2006) is a function of $d_m^{0.86}$ rather than d_m.

The average values and standard deviation of the maximum length (L_{avg}), width (W_{avg}), and aspect ratio $(L/W)_{avg}$ of silver agglomerates are summarized in Table 2-4 as a function of mobility diameter. In Table 2-4, doubly charged particles and fragments are excluded. The relation between the maximum projected length and projected area equivalent diameter for silver agglomerates is shown in Figure 2-6 for only singly charged particles. The maximum length can be scaled to and the projected area

equivalent diameter and the mobility diameter with the same power (1.19) as shown below:

$$L \sim d_{pa}^{1.19} \sim d_{m}^{1.19}. \quad (2\text{-}5)$$

Park et al. (2004a) obtained the relation $L \sim d_{pa}^{1.26} \sim d_{m}^{1.26}$ for diesel agglomerates. Equation (2-5) will be used in the next section for the calculation of a fractal dimension based on maximum projected length (D_{fL}).

2-3-4. Fragmentation of agglomerates

Park et al. (2004a) used a Low Pressure Impactor (LPI) (Hering et al., 1978) consisting of 8 stages with a minimum cut size of 50 nm for sampling diesel particles. They found that fragmentation of agglomerate may occur upon impact. In this study, an electrostatic sampling method was used. The Nanometer Aerosol Sampler (Model 3089, TSI, Inc.) is based on Dixkens and Fissan (1999)'s design. The LPI makes use of inertial impaction of particles while the electrostatic sampling method makes use of electric field for the collection of particles. Even though a different sampling method was used in this study, there is also a small peak around 60 nm for agglomerates with d_m = 120 nm as shown in Figure 2-4 and around 80 nm for agglomerates with d_m = 150 nm similar to Park et al. (2004a)'s observation. These results indicate that the fragmentation of silver agglomerate may occur when the electrostatic sampling method is used. The possibility of fragmentation of agglomerate when the electrostatic sampling method is used was also observed by Weber et al. (1996) and Weber and Friedlander (1997). The

kinetic energy of agglomerate particle was estimated before the impact on the TEM grid for both sampling methods using electrostatic or inertial force. For the electrostatic sampling method used in this study the voltage applied on a copper TEM grid is -9 kV. Following Weber and Friedlander (1997), it was assumed that the agglomerate potential energy of 1.44×10^{-15} J (1.6×10^{9} Cb · 9 kV) is converted to kinetic energy without friction losses in the gas before impact on the grid. One can collect agglomerate particles with d_m =150 nm on the stage 6 of a LPI as described in Hering et al. (1978). The jet velocity and operating pressure of the stage 6 is 150 m/s and 106 mmHg, respectively. It was assumed that particle can follow the jet flow and neglected friction losses in the gas. Then, the kinetic energy of silver agglomerate with d_m = 150 nm is estimated to be approximately an order of 10^{-14} J. In the above cases, it appears that the kinetic energy of particle inside a low pressure impactor is larger compared to electrostatic sampling method. The average energy available to break one bond in silver agglomerate is an order of 10^{-18} J from Weber and Friedlander (1997) and Froeschke et al. (2003). This may indicate that one needs to apply a relatively low electric voltage in order to sample agglomerate particles without fragmentation.

2-3-5. Fractal(-like) dimension

In this section, the fractal dimension of agglomerate are obtained using three different techniques: (1) deriving D_f from projected TEM images using a box counting method, (2) deriving D_f from the number of primary particles and the maximum length of agglomerates, (3) deriving D_f theoretically from Lall and Friedlander (2006).

First, the 2-D fractal dimension D_f was derived as the slope on a least square linear fit of the plot of log n vs. log box size, where n_{box} is the number of non-overlapping equal boxes that would fill the projected surface area of the agglomerate. The equation for the slope ($\gamma = 1-D_f$) is shown in Hinds (1999) as follows:

$$n_{box} = k\,\delta_{box}{}^{\gamma} = k\,\delta_{box}{}^{1-D_f}, \qquad (2\text{-}6)$$

where k is a constant and δ_{box} is a box size. This method was previously used by Ku and Maynard (2006) and Gwaze et al. (2006). Gwaze et al. (2006) carried out a detailed analysis on the effect of the image resolution defined as the pixels per primary particle diameter. They found that the fractal dimension was changed by 9-18 % depending on the resolution with the range of 4-50 and poorly resolved intricate TEM images may result in an overestimation of projected surface area. In this study, a biased result due to resolution was minimized by using a very high resolution about 30-118 pixels per primary particle diameter. It is shown that the 2-D fractal dimensions of silver agglomerate are 1.84 ± 0.03 for d_m = 80 nm, 1.75 ± 0.06 for d_m = 120 nm, and 1.74 ± 0.03 for d_m = 150 nm. This result is comparable to Ku and Maynard (2006)'s result. Ku and Maynard reported that the 2-D fractal dimension of silver agglomerate has a range from 1.58 to 1.94 for differently sintered silver agglomerate particles. From Ku and Maynard (2006) and Weber and Friedlander (1997) one can expect that a higher degree of necking will increase the fractal dimension.

Secondly, the 2-D fractal dimension D_f was obtained from the number of primary particles and the radius of gyration (R_g) described by Eq. (2-1). Several studies suggested the following relationship between the projected area and number of primary

particles (Samson et al. 1987; Meakin et al. 1989; Megaridis and Dobbins 1990; Koylu et al. 1995; Brasil et al. 1999):

$$N = k_a \cdot \left(\frac{A_a}{A_p} \right)^{\alpha}, \tag{2-7}$$

where A_a is the projected area of the agglomerate, A_p is the mean projected area of primary particles, k_a is an empirical constant, and α is an empirical projected area exponent. In this study, in order to determine N, α = 1.09 and k_a = 1.15 (Koylu et al., 1995) were used for Eq. (2-7). The radius of gyration can also be extracted from projected properties. Several studies suggested that the maximum projected length (L) can be related to R_g as follows: $L/2R_g$ = constant (Koylu et al., 1995; Oh and Sorensen, 1997; Brasil et al., 1999). Using the relation, $L/2R_g$ =constant, Park et al. (2004a) approximated Eq. (2-1) as follows:

$$N = k_L \cdot \left(L / d_p \right)^{D_{fL}}, \tag{2-8}$$

where k_L is a prefactor and D_{fL} is a fractal dimension based on the maximum projected length (L). The relationship between the number of primary particles, N, and the maximum projected length, L, normalized with respect to primary particle diameter, d_p is shown in Figure 2-7. The fractal dimension (D_{fL}) based on the maximum projected length is 1.47. The square of the correlation coefficient between N and L/d_p is 0.81.

Thirdly, a mass-mobility diameter scaling exponent (D_{fm}) was derived based on the mobility diameter using Lall and Friedlander (2006). It was assumed that mass is proportional to N and primary particles have the same particle size similar to Park et al. (2004a). Park et al. (2004a) measured mass of diesel particles using Aerosol Particle

Mass analyzer (APM) and defined the relationship between mass and mobility diameter as follows:

$$m = k_m \left(\frac{d_m}{d_p} \right)^{D_{fm}}, \tag{2-9}$$

where k_m is a prefactor. Using the relation that mass is proportional to N, Eq. (9) can be expressed as:

$$N = k_{m1} \left(\frac{d_m}{d_p} \right)^{D_{fm}}, \tag{2-10}$$

where k_{m1} is a prefactor. The number of primary particles, N, is given by Eq. (2-4) from Lall and Friedlander (2006). By combining Eq. (2-10) with Eq. (2-3), D_{fm} of 1.71 and k_{m1} of 1.69 were obtained for the size range of d_m equal to 80 to 150 nm. Lall and Friedlander (2006) give us a fixed fractal dimension independent of primary particle size even though it slightly depends on the mobility size range. Since the model by Lall and Friedlander (2006) assumes a loose and transparent structure (D_f less than 2), the computations of D_f based on their model is not likely to give a D_f larger than 2. Schmidt-Ott (1988) obtained a mass-mobility diameter scaling exponent of 2.18 for silver agglomerates in the size range below d_m = 100 nm. In order to derive the 3-D fractal dimension, Schmidt-Ott (1988) used a size of close-packed clusters instead of using the radius of gyration. A recent study (Kim et al., 2009; Shin et al., 2009a) shows that mass-mobility diameter scaling exponent of silver agglomerate measured by DMA-Aerosol Particle Mass analyzer (APM) method is 2.08 in the particle size range of 100 to 300 nm. Park et al. (2004a) computed the ratio between D_{fm} and D_{fL} for diesel agglomerates and obtained D_{fm} / D_{fL} =1.26. With the recent results (Kim et al., 2009;

Shin et al., 2009a) for the D_{fm} of silver agglomerates, D_{fm} / D_{fL} of 1.19 was obtained. The value is close to the result by Park et al. (2004a).

2-3-6. Number of primary particles in an agglomerate

In this section, the number of primary particles as a function of mobility diameter is obtained from three different methods: (1) using Eq. (2-7) with coefficients from Koylu et al. (1995) with measured projected area equivalent diameter (2) using Eq. (2-2) with a relation between projected area equivalent diameter and mobility diameter, i.e., $d_{pa} = 0.92 \pm 0.03\ d_m$ (3) using Lall and Friedlander (2006), i.e., Eq. (2-4). Figure 2-8 shows a comparison of different methods to obtain the number of primary particles as a function of d_m/d_p. The symbols indicate data points for d_m = 80 nm, 120 nm, 150 nm. The values from the first method are larger than those from the second and third method. It may be due to a difference in the basic assumption of individual methods. The first and third methods make use of the assumption that the agglomerate has a loose and transparent structure while Koylu et al. (1995)'s equation reflects some shielding effects which is more appropriate for real agglomerates.

2-3-7. Comparison with results in literature

In this section, structural properties of agglomerates obtained from this study are compared with previous data (Schmidt-Ott, 1988; Weber and Friedlander, 1997; Ku and

Maynard, 2006; Lall et al., 2006) for the structural properties of silver agglomerate. Primary particle sizes of silver agglomerate from those studies are below 20 nm even though reactor conditions are different. The fractal dimension obtained with a box counting method is larger by 15 % than that obtained by Ku and Maynard (2006) using the same method. Those 2-D fractal dimensions are smaller than 3-D fractal dimension measured by Schmidt-Ott (1988) and Weber and Friedlander (1997). A mass-mobility diameter scaling exponent (D_{fm}) of 1.71 was derived from the mobility analysis (Lall and Friedlander, 2006). This value is closer to the measured 2-D fractal dimension because the model assumes a loose and transparent agglomerate, i.e., 2-D agglomerate. For the number of primary particles in an agglomerate, it would be difficult to make a direct comparison because primary particle sizes of each study are different. The number of primary particles estimated using Eq. (2-2) with $d_{pa} = 0.92 \pm 0.03\ d_m$ for d_m = 80 nm, N = 29 is smaller than N =34 calculated using Lall and Friedlander (2006) for d_m = 80 nm. Schmidt-Ott (1988) and Weber and Friedlander (1997) give us a little larger number of primary particles compared to the method using Eq. (2-2) with $d_{pa} = 0.92 \pm 0.03\ d_m$ because the former methods take account of three dimensional effects, i.e., shielding between primary particles.

2-4. Conclusions

The objective of this study is to analyze the structural properties of silver agglomerates based on TEM measurement and relate the results to mobility analysis.

Agglomerates with mobility diameters of 80 nm, 120 nm, and 150 nm are sampled using electrostatic method and then imaged by TEM.

According to the tilting angle of TEM specimen holder, the extent of variation of structural properties based on TEM measurement is 10 % for the projected area equivalent diameter and about a factor of 2 for the projected maximum length and aspect ratio of agglomerate. However, 2-D fractal dimension using a box counting algorithm is insensitive to the tilting angle of TEM specimen holder. In order to minimize those artifacts, a lot of particle samples need to be randomly chosen and then analyzed.

It was observed that silver agglomerates with d_m = 120 nm and 150 nm are fragmentized when they are sampled using electrostatic method similar to previous studies by Weber et al. (1996) and Weber and Friedlander (1997). The kinetic energy of particle inside a low pressure impactor is one order of magnitude higher compared to electrostatic sampling method. This may indicate that one needs to apply a relatively low electric voltage in order to sample agglomerate particles without fragmentation.

Measured projected area equivalent diameter, d_{pa}, is slightly smaller than mobility diameter, d_m. The relationship between the two quantities is $d_{pa} = 0.92 \pm 0.03\ d_m$ for silver agglomerates in the size range of d_m = 80 nm to 150 nm. Fractal dimensions of silver agglomerates were obtained using three different methods: (1) Two-dimensional fractal dimensions (D_f) = 1.74 to 1.84 from projected TEM images using a box counting algorithm, (2) fractal dimension (D_{fL}) = 1.47 based on maximum projected length using an empirical equation proposed by Koylu et al. (1995), (3) mass-mobility diameter scaling exponent (D_{fm}) = 1.71 theoretically derived from the mobility analysis proposed

by Lall and Friedlander (2006). 2-D fractal dimensions measured by using a box counting algorithm are closer to the mass-mobility diameter scaling exponent (D_{fm}) of 1.71 derived from the mobility analysis (Lall and Friedlander, 2006) rather than three-dimensional fractal dimension of 2.18 measured by Schmidt-Ott (1988). The reason may be that Lall and Friedlander (2006) has an assumption that agglomerate particle is loose and transparent. Therefore, the model can be comparable to two-dimensional TEM analysis.

Three different methods were used to obtain the number of primary particles in agglomerate. The number of primary particles obtained from the projected surface area using an empirical equation from Koylu et al. (1995) is larger than those obtained from the projected area measurement directly or from the mobility analysis. It is because the former includes shielding effect while the others assumed completely transparent agglomerates. Number of primary particles calculated using Lall and Friedlander (2006) or using the relationship between d_m and d_{pa} with an assumption that agglomerate is loose and transparent may be an underestimate for real agglomerates.

Type	Dimensions	Residence time, s	Temperature, °C
Electric tube furnace	Length: 89 cm I.D. :1.43 cm	2.85	1100
Agglomeration chamber	Volume: 2.7 L I.D.: 15 cm	60	25

Table 2-1. Condition of particle generation system

Image	Tilting angle (deg)	d_{pa} (nm)	L (nm)	L/W	D_f
a	0	99.3	176.9	1.59	1.80
b	+22.54	93.3	142.3	1.19	1.80
c	-19.42	103.8	211.5	2.12	1.81
d	-38.71	103.1	246.2	2.56	1.75

Table 2-2. Projected area equivalent diameter, maximum projected length, aspect ratio, and fractal dimension vs. tilting angle of TEM specimen holder for an agglomerate with d_m = 120 nm

d_{m1} (nm)	d_{pa1} (nm)	d_{m2} (nm)	d_{pa2} (nm)
80	75	119	105
120	110	180	160
150	145	230	215

Table 2-3. Mobility diameter and projected area equivalent diameter

d_m (nm)	Number of analyzed agglomerates	L_{avg} (nm)	W_{avg} (nm)	$(L/W)_{avg}$
80	122	140.12±25.92	83.44±18.91	1.77±0.56
120	120	228.42±48.16	138.88±28.51	1.71±0.51
150	60	321.60±65.77	186.39±37.12	1.79±0.51

Table 2-4. The maximum projected length, maximum projected width, and aspect ratio of silver agglomerates for d_m = 80 nm, 120 nm, 150 nm

	d_p (nm)	D_f	N
Schmidt-Ott (1988)	15	2.18[a]	27[c]
Weber and Friedlander (1997)	13	2.03[a]	41[d]
Ku and Maynard (2006)	20	1.58 ±0.02[b]	NA
Lall and Friedlander (2006)		1.71	
Lall et al. (2006)	18.5 ± 3.5		19[c]
this study	13.8 ± 2.5	1.84 ± 0.03[b]	34[e] , 29[f]

[a] Three dimensional fractal dimension

[b] Two dimension fractal dimension obtained using a box counting algorithm in ImageJ software

[c] for d_m = 80 nm

[d] for d_m = 74 nm

[e] Calculated using Lall Friedlander (2006) for d_m = 80 nm

[f] Calculated using Eq. (2) with d_{pa}=0.92 ± 0.03 d_m for d_m = 80 nm

Table 2-5. Comparison with results in literature for the structural properties of silver agglomerates

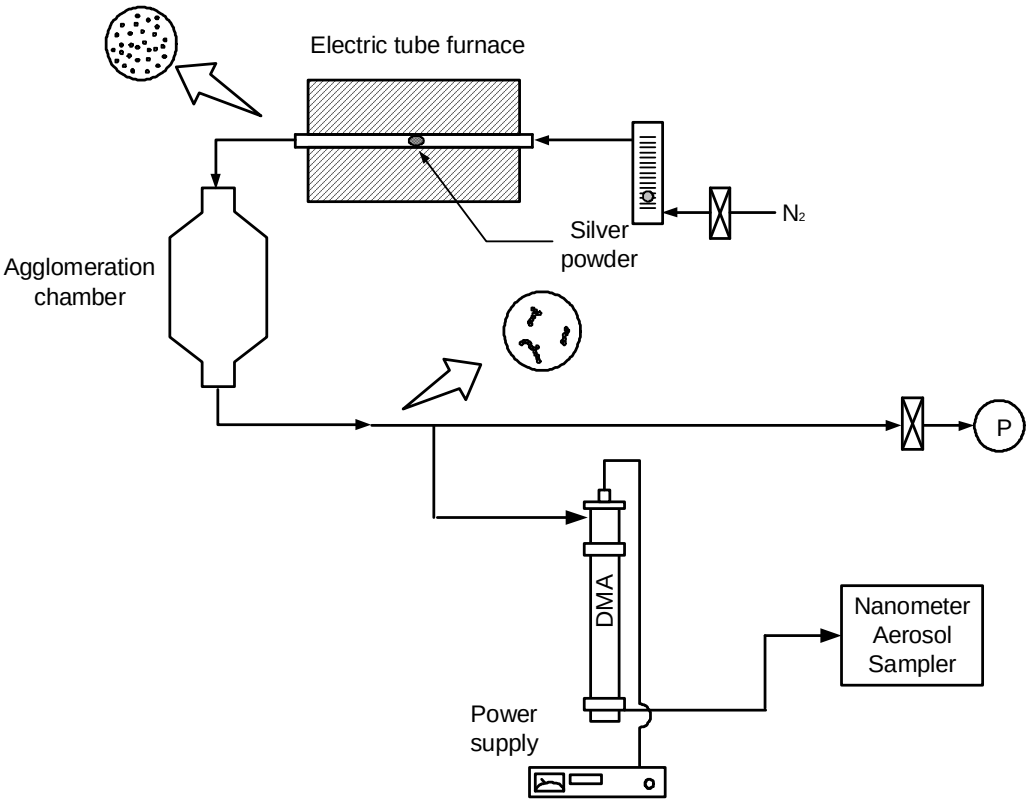

Figure 2-1. Schematic diagram for the experimental set-up

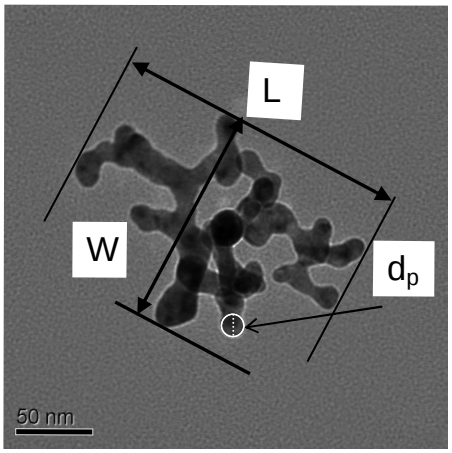

(a)

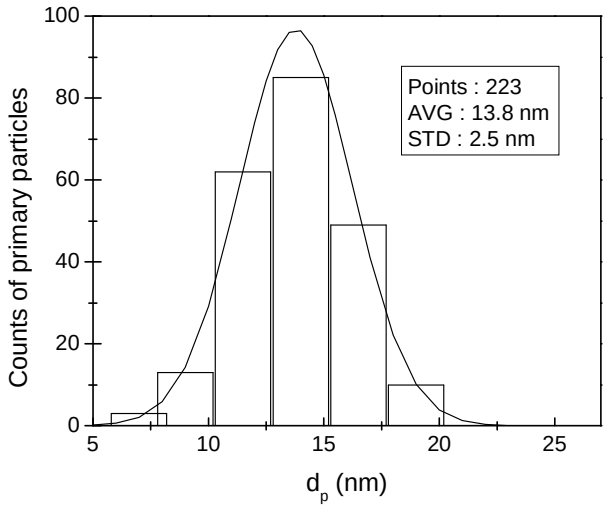

(b)

Figure 2-2. (a) Parameters measured from TEM image (b) primary particle size distribution at the furnace temperature of 1100 °C

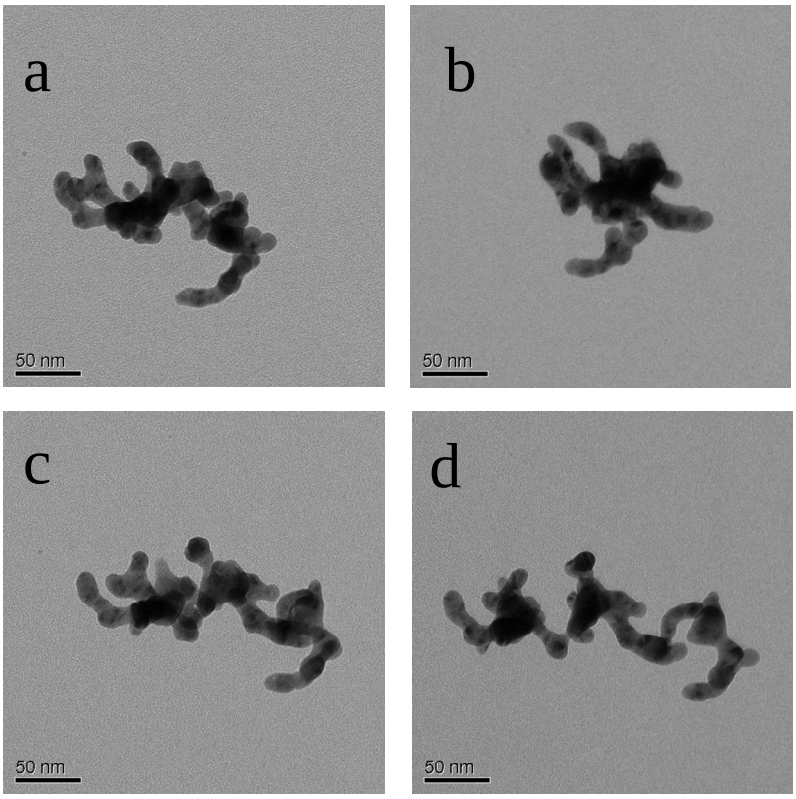

Figure 2-3. TEM images of the same agglomerate with d_m = 120 nm viewed at different tilting angles of the TEM specimen holder

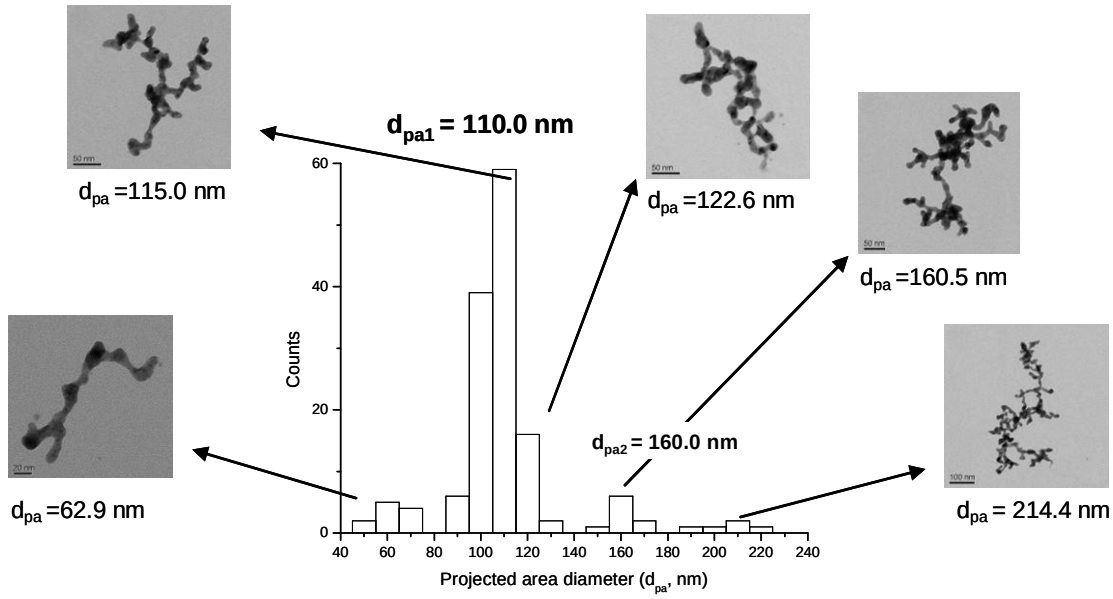

Figure 2-4. Projected equivalent area diameter distribution for d_m = 120 nm (The total number of analyzed agglomerates is 148)

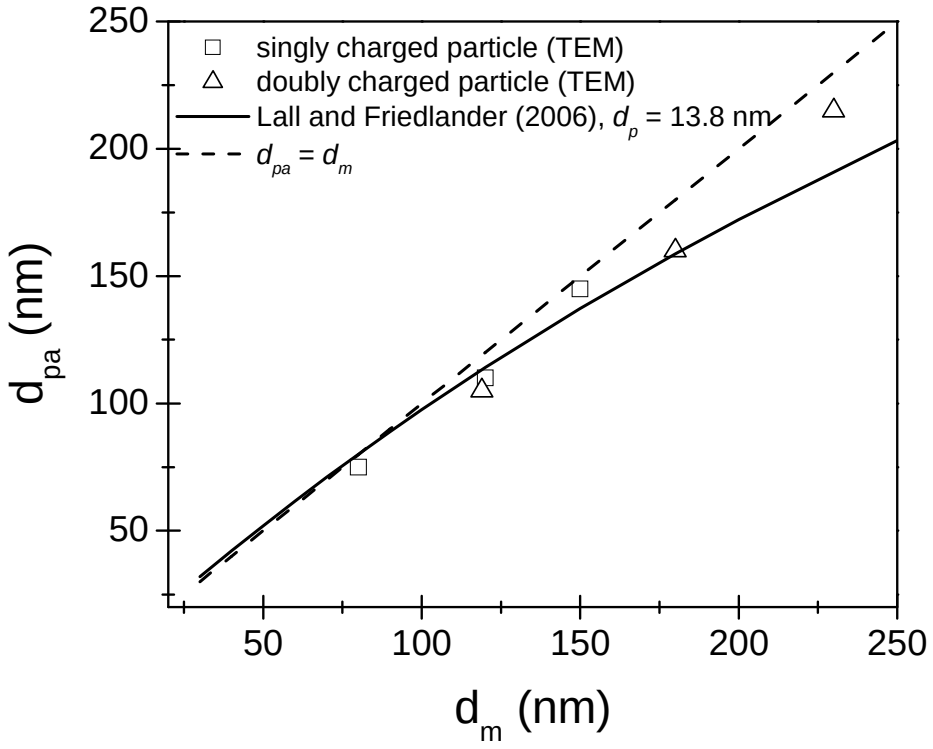

Figure 2-5. Projected area equivalent diameter vs. mobility diameter: comparison of TEM analysis results with theoretical prediction result using Lall and Friedlander (2006)

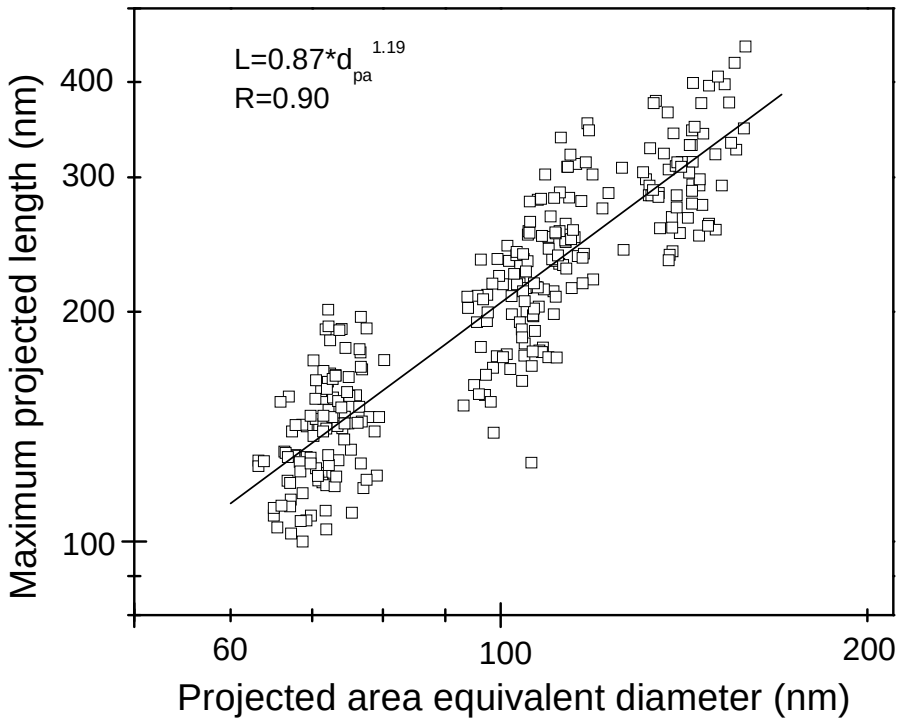

Figure 2-6. The maximum projected length vs. projected area equivalent diameter

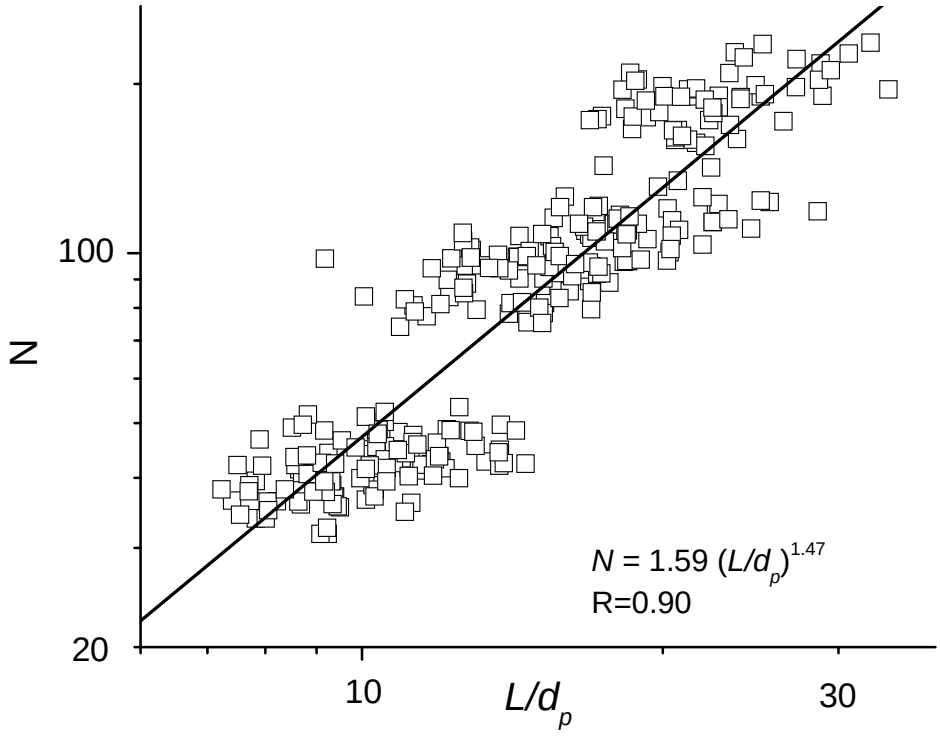

Figure 2-7. Number of primary particles vs. L/d_p from TEM measurement: the three different clusters of experimental data points are for d_m = 80 nm, 120 nm, and 150 nm, respectively

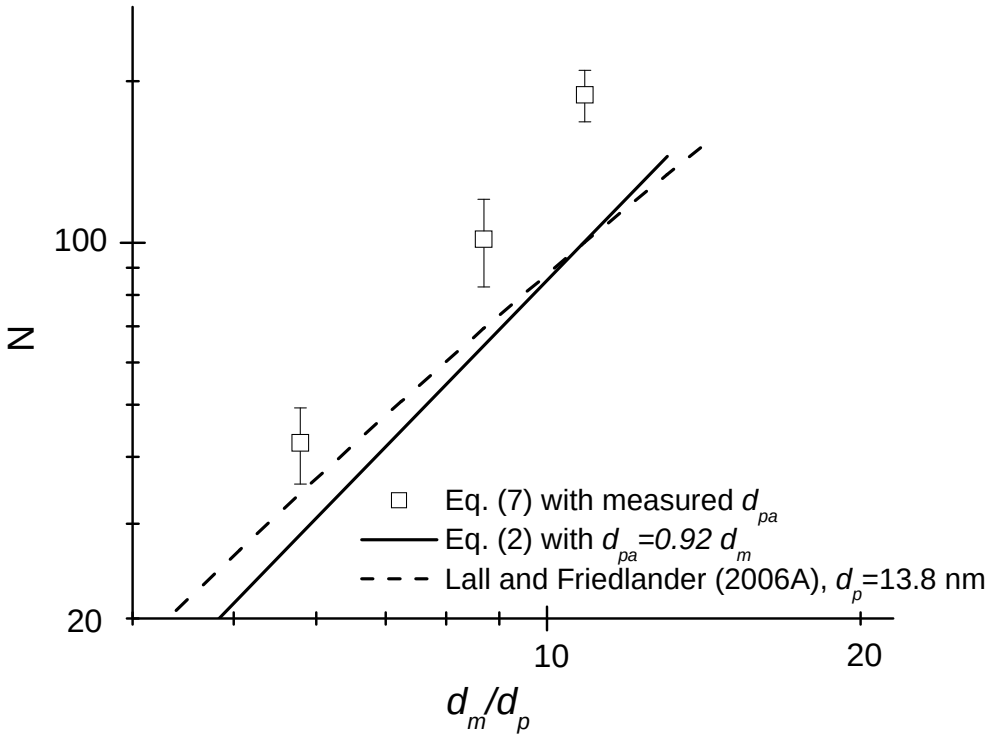

Figure 2-8. Number of primary particles vs. d_m/d_p

Chapter 3 Study of Dynamic Shape Factor and Friction of Coefficients of Agglomerates Using DMA-APM

3-1. Introduction

The friction coefficient f is a key quantity for describing the motion of an aerosol particle including its diffusion, electrical mobility, sedimentation, thermophoresis, and coagulation rate. It is defined as the force exerted by the fluid on the particle as it moves at a constant velocity through the fluid divided by the velocity. For a spherical particle, the friction coefficient is given by:

$$f_{sph.} = \frac{3\pi\mu d_{sph.}}{C\left(d_{sph.}\right)} \quad , \tag{3-1}$$

where $d_{sph.}$ is the sphere diameter, μ is the viscosity of the gas, and $C_c(d_{sph.})$ is the Cunningham slip correction factor, which corrects for non-continuum gas behavior on the motion of small particles. In the limit of small Knudsen number (continuum limit), the expression for $f_{sph.}$ reduces to the Stokes expression. In the limit of large Knudsen number (free molecular limit), $f_{sph..}$ is proportional to d_{sph}^2.

In this chapter, it is of interest to investigate the friction coefficient of nanoparticle agglomerates (NP agglomerates), which are cluster or chains of nanoparticle spherules. Such particles are produced by high temperature processes

leading to a solid particulate. Combustion is a primary source including diesel particulate and soot from building fires. Combustion is also used to make a variety of materials in agglomerate form including fumed silica, titanium dioxide, and carbon black. A variety of metallic agglomerates including silver, iron, and copper are produced by the vaporization of the metal and subsequent cooling in a non-oxidative environment.

The objective of this study is two fold. The first is to obtain quantitative data on the friction coefficient of NP agglomerates as a function of the agglomerate size for agglomerates with fractal dimension less than 2 and primary sphere size in the free molecular regime. The second is to compare the measured results with model calculations for agglomerates based on free molecular behavior for the primary spheres. One topic of interest is whether there is a difference between experiment and model predictions with increasing agglomerate size. A model does not currently exist that can account for the effect of the flow interaction between the primary particles on the friction coefficient. Existing models assume that the flow is free-molecular at the length scale of the entire agglomerate. They do not consider the case where the length scale of the agglomerate is comparable or several times larger than the mean free path of the gas. Quantitative data is needed to test the various predictions for the friction coefficient of large agglomerates.

Chan and Dahneke (1981) used a Monte Carlo approach to compute the friction coefficient of a straight chain of spherical particles in the free molecular limit based on the Knudsen number of the primary particle diameter $Kn_p = 2\,\lambda/d_p$ where λ is the mean free path of the gas, and d_p the diameter of the primary sphere. For randomly oriented

straight chain agglomerates, the following expression is obtained for the friction coefficient:

$$f = \left(c^*_{bcu}\left(N-1\right) + c^*_{sph.}\right)\mu\, d_p^2 / 4\lambda \qquad , \qquad (3\text{-}2)$$

where N is the number of spheres in the chain, μ the gas viscosity, d_p the diameter of the primary sphere, $c^*_{sph.}$ is the dimensionless friction coefficient for a sphere, and λ is the mean free path of the gas. The quantity c^*_{bcu} is the orientation averaged dimensionless friction coefficient for a basic chain unit, two hemispheres touching at their poles. Assuming 7 % of the collisions to have specular reflections and 93 % diffuse reflections, Chan and Dahneke (1981) obtained values of 9.17 for c^*_{bcu} and 11.44 for $c^*_{sph.}$. For N > 12, Eq. (3-2) can be approximated to within 2 % accuracy by the following:

$$f = c^*_{bcu}\, N\, \mu\, d_p^2 / 4\lambda\,. \qquad (3\text{-}3)$$

The linear dependence of the friction coefficient on the number of primary spheres for larger chains is a key feature of Eq. (3-3). Other researchers have assumed that this proportionality is also valid for agglomerates with fractal dimension less than 2. For example, Mountain et al. (1986) made this assumption in modeling the kinetics of agglomeration and Lall and Friedlander (2006) in developing a methodology for determining the size distribution of agglomerates based on electrical mobility measurements.

Meakin et al. (1989) used computer simulations of collision between point masses and fractal agglomerates to compute the friction coefficient of the agglomerate in the free molecular limit. The agglomerates were generated using ballistic cluster-

cluster aggregation and ranged in size from a few primary spheres up to about 8 000 spheres. The dependence of friction coefficient, $f(N)$, on the number of primary spheres can be expressed as:

$$f(N) \cong 4 S_{pa}(N) \delta P_{\infty} n m v / 3, \tag{3-4}$$

where S_{pa} is the projected area of the agglomerate, δP_{∞} is the total momentum transfer, n_g is the number density of gas molecules, m_g is the mass of a gas molecule, and v_g is the average speed of the gas molecules. Meakin et al. found that the momentum transfer is insensitive to *N* so that the only significant *N* dependence is in the projected area. In computing the orientation averaged friction coefficient, Meakin et al. assumed that the average of the product $(S_{pa}\ \delta P_{\infty})$ was equal to the product of the averages $(S_{pa})(\delta P_{\infty})$; that is, that there was no correlation between the projected area and the momentum transferred. Nakamura and Hidaka (1998) have verified this finding for the conditions used in this study where the particle velocity is small compared to gas velocity.

Mackowski (2006) used a Monte Carlo method for computing the friction coefficient of fractal agglomerates. He generated agglomerates using an algorithm that satisfied the fractal power law relationship between *N* and the radius of gyration for each agglomerate generated. The Monte Carlo method is similar to that used by Chan and Dahneke except Mackowski's treatment was restricted to the aerosol velocity much less than the gas velocity. Mackowski (2006) found that the friction coefficient was proportional to $N^{0.94}$ for fractal dimensions in the range 1.7 to 2.0 and for *N* in the range 3 to 3000.

The friction coefficient is often expressed in a reduced form termed the dynamic shape factor κ. This quantity is equal to the ratio of the friction coefficient of the agglomerate, $f_{aggl.}$, to the friction coefficient of a sphere with the same condensed phase volume as the agglomerate.

$$\kappa = \frac{f_{aggl.}}{f_{ve}} = \frac{f_{aggl.} C_c(d_{ve})}{3\pi\mu d_{ve}} \quad , \tag{3-5}$$

where the subscript *ve* refers to the volume equivalent sphere. With the recent development of the aerosol mass analyzer, it is now possible to accurately measure κ for agglomerates. This study is restricted to agglomerates with the primary sphere size in the free molecular range.

While there have been a number of studies of the dynamic shape factor of regular 3-D structures such as prolate ellipsoids, rods, and of multiplets with 5 or fewer spheres (Kousaka et al., 1996; Song et al., 2005; Zelenyuk and Imre, 2007), there have been few studies for larger agglomerates produced by high temperature processes. One of these was a study by Park et al. (2004a) to measure the dynamic shape factor of diesel exhaust particles. They used a differential mobility analyzer (DMA) and electron microscopy to measure the dynamic shape factor. The electrical mobility of an agglomerate $Z_{aggl.}$ can be expressed in terms of its friction coefficient by performing a force balance between the electrical force and the drag force:

$$Z_{aggl.} = \frac{v}{E} = \frac{e}{f_{aggl.}}, \tag{3-6}$$

where E is the electric field and v the drift velocity. The mobility of the agglomerate is equal to the mobility of a sphere with diameter d_m.

$$Z_{aggl.} = Z_{sph.}(d_m) = \frac{eC_c(d_m)}{3\pi\mu d_m}, \tag{3-7}$$

where the second expression is obtained by substituting for the friction coefficient for a sphere from Eq. (3-1). The value of d_m is computed from Eq. (3-7) where the mobility is the experimentally obtained value with the DMA. Also from Eqs. (3-6) and (3-7), one obtains the following expression for the friction coefficient of an agglomerate:

$$f_{aggl.} = \frac{3\pi\mu d_m}{C(d_m)}. \tag{3-8}$$

Finally, substituting Eq. (3-8) into Eq. (3-5), one obtains an expression for the dynamic shape factor as function of only the mobility diameter and the volume equivalent sphere diameter (Kasper, 1982; Kelly and McMurry, 1992):

$$\kappa = \frac{d_m C_c(d_{ve})}{d_{ve} C_c(d_m)}. \tag{3-9}$$

Note that the Cunningham slip correction factors are for spherical particles with diameters d_{ve} and d_m and not the slip correction for the agglomerate.

The volume equivalent diameter was determined by electron microscopy. This was a labor intensive process. With extensive analysis and correction for particle overlap, Park et al. (2004a) were able to obtain dynamic shape factor measurements of diesel exhaust particulates with an uncertainty of 10 % to 15 % over a mobility size range from 50 nm to 220 nm.

The dynamic shape factor of silver agglomerates was chosen to be measured using a combination of a DMA and an Aerosol Particle Mass Analyzer (APM) (Ehara et al., 1996). The use of an aerosol composed of one material allows us to determine the

volume of the particles from their mass and the density of silver. This was not possible with diesel particulate which contains both carbonaceous material and some amount of lubricating oil. There are two major advantages of using an APM for determining the volume equivalent diameter: The APM is an online instrument allowing the measurement of the volume of several mobility selected particles within an hour compared to nominally a week of TEM analysis to do the same. Secondly the uncertainty in the volume determined by the APM is on the order of a factor of 2 to 3 less than that obtained by TEM.

A dynamic shape factor κ_R based on mobility radius was obtained in the pioneering study (Schmidt-Ott, 1988) for silver agglomerates. Schmidt-Ott used two DMAs: the first to select an agglomerate size and to measure the friction coefficient and the second to measure the diameter of the fully sintered agglomerate. The second measurement allows one to determine the volume equivalent diameter. The mobility radius dynamic shape factor was defined in Eq. (7) of Schmidt-Ott as:

$$\kappa_R = \frac{R_m}{R_{ve}}. \tag{3-10}$$

(Note that Schmidt Ott used the symbol R_0 for mobility radius while the symbol R_m used in this study.) This quantity can be related to κ as explained in the discussion section. Experiments in this study include agglomerates over the mobility diameter range from 50 nm to 300 nm compared to a range of about 25 nm to 90 nm in the Schmidt-Ott study. One motivation for this study was to obtain accurate measurements of the dynamic shape factor for agglomerates with up to several hundred primary particles and to compare with theoretical predictions.

The fundamental dynamic quantity predicted by the various theories (Chan-Dahneke, Meakin et al., and Mackowski) is the friction coefficient. The DMA is used in this study to select nearly monodisperse agglomerates in terms of the friction coefficient. The APM measurement of agglomerate mass of the monodisperse agglomerates allows one to infer the number of primary particles in the agglomerate from TEM information on the primary sphere size and from the known density of silver. Thus, with these two instruments the friction coefficient can be accurately determined as a function of the number of primary spheres for narrowly distributed agglomerates and then compare with the various theoretical models. As mentioned, the major interest in this study to determine at what value of N the theoretical predictions for the friction coefficient begin to deviate from the experimental data.

There have been a number of agglomerate studies on the relationship between the mobility radius and the radius of gyration and between the mobility radius and the number of primary particles in an agglomerate. These include the studies for in-flame carbonaceous aerosols in the free molecular regime (Cai and Sorensen, 1994), for TiO_2 agglomerates with Kn in the range 0.02 to 1.3 as well as an insightful review of other experimental studies covering a wide range in Kn (Wang and Sorensen, 1994), and for TiO_2 and Si agglomerates with Kn in the range 0.14 to 2.2 (Rogak et al., 1993). In this case the Knudsen number is defined based on the radius of gyration ($Kn_R = \lambda / R_g$). The results for the relation between d_m and N will be compared with these previous studies along with those of Schmidt-Ott (1988) in the Discussion section.

3-2. Experimental

Silver nanoparticles, generated by the evaporation/condensation of silver powder (99.999%, Johnson Mattney Electronics) within an electric tube furnace, collide and stick together in an agglomeration chamber leading to NP agglomerates made up of a few primary particles up to several hundred. Nitrogen is used as the carrier gas. Two sets of data were collected using slightly different conditions. Two different tube furnaces were used at slightly different temperatures and two different volume agglomeration chambers were used (See Table 3-1.). The average primary sphere size was 16.2 nm with a standard deviation of 3.4 nm for the first experimental dataset obtained in March 2007 and 19.5 nm with a standard deviation of 6.1 nm for the second experimental dataset obtained in January 2008. More than 200 primary particles was measured for both datasets. For the primary particle size 19.5 ± 6.1 nm, 254 primary particles were measured. For the case, the uncertainty in the mean size is 0.38 nm. In the rest of this paper, the first experiments are refered to as Set 1 and the second as Set 2. Transmission Electron Microscope (TEM) images for d_m =100 nm and 200 nm are shown in Figure 3-1. For the Set 1, a second tube furnace was located between the agglomeration chamber and the DMA. In one experiment the tube furnace was turned off and in the second it was set at 100 ^{o}C. The measurements in Set 1 were part of an agglomerate filtration study (Kim et al., 2009). The general methodology used for generating agglomerates is similar to that used by others (Schmidt-Ott, 1988; Lall et al., 2006; Ku and Maynard, 2006).

Using TEM Shin et al. (2009b) characterized silver agglomerate particles generated in the same way as in this study. Agglomerates with mobility diameters of 80, 120, and 150 nm were sampled using the electrostatic method and then imaged by TEM. Fractal dimensions of silver agglomerates were obtained using a box counting algorithm in Image J software. The fractal dimensions are 1.84±0.03, 1.75±0.06, and 1.74±0.03 for d_m = 80, 120, and 150 nm, respectively from projected TEM images. The values are close to 1.78, i.e., the fractal dimension for self-similar aggregates produced by diffusion limited cluster aggregation (DLCA) in aerosols (Jullien and Botet, 1987). Also, in Meakin (1989)'s study, the fractal dimensions of agglomerates are in the range 1.80 to 1.95. Considering that the fractal dimensions obtained from projections are 10-15 % lower than the fractal dimensions of the three dimensional agglomerates (Samson et al., 1987), the measured 2-D fractal dimension is close to the fractal dimension used in Meakin et al.'s study. Thus the size dependence of the friction coefficient obtained by the simulations of Meakin et al. is relevant to this experimental study. However, the silver agglomerates show prominent necking while the Meakin aggregates are composed of spheres with point contacts. The estimate of the effect of necking on the friction coefficient of agglomerates is discussed in Chapter 5.

A schematic diagram of the system for generating the silver NP agglomerates together with DMA-APM system is shown in Figure 3-2. The NP agglomerates are classified by mobility diameter using a DMA operating with an aerosol to sheath flow ratio of 0.1. Only charged particles with a narrow range of mobility with a half-width at half-height of about 5 % pass through the DMA. The DMA was calibrated with NIST

traceable reference particles and the estimated 1 sigma uncertainty in the mobility diameter is 4 %.

The charged particles then enter the APM, which consists of two cylindrical electrodes rotating together at the same controlled speed (~3,000 rpm). A voltage is applied to the inner electrode with the outer electrode grounded. Particles flow into the small gap between two electrodes and experience centrifugal and electrostatic forces. The APM transmits particles of a known mass (independent of particle shape or composition), determined by the balance of the centrifugal and electrostatic forces (Park et al., 2004a). The concentration of the transmitted particles is measured by a condensation particle counter (CPC). The relationship between the centroid mass m of the particles with q unit charges and the rotation frequency ω, voltage V, and radii of the inner and outer electrodes r_1 and r_2 is given (Ehara et al., 1996):

$$m = \frac{qV}{r_c^2 \omega^2 \ln(r_2 / r_1)}, \tag{3-11}$$

where r_c is the average of r_1 and r_2. The centroid mass is the mass of a particle for which the net force acting on the particle is zero at r_c.

3-2-1. Calibration uncertainty of APM

There are a number of factors that contribute to the uncertainty in the mass measurement. These include measurement repeatability, the calibration uncertainty, and the uncertainty in obtaining the size distribution from inverting the convolution integral. The number concentration is plotted as a function of mass passing through the

APM (Figure 3-3). Repeat measurements of the peak mass were obtained using Gaussian fits and the CVs (coefficient of variation equal to the standard deviation divided by the average) were typically less than 0.01 (Table 3-2).

To assess the calibration uncertainty of the APM, the peak in the mass distribution of 200 nm NIST traceable polystyrene latex (PSL) spheres was measured. A difference of 3.9 % between the measured peak and the mass computed from the certified diameter and the density of PSL spheres was obtained. Ehara et al. (1996) made a similar comparison for 309 nm diameter PSL spheres and obtained a difference of 6.5 %. McMurry et al. (2002) showed that using an APM together with PSL calibration spheres, the density of spherical droplets from Fomblin Y-25 and dioctyl sebacate (DOS) of sizes 107 nm and 309 nm in diameter could be measured within ~ 5 %. This 5 % uncertainty in the density corresponds to the systematic component in the APM uncertainty. The actual uncertainty could be larger. Based on the above results, the calibration uncertainty for the APM used in this study was approximated as 5.5 % for the mass range of 0.3 fg to 15 fg.

The peak in APM plot of number versus mass differs slightly from the peak in the number distribution as a function of mass of the agglomerates exiting the DMA. It is the mass at the peak in the size distribution exiting the DMA, G(m), which is needed so that both the mobility diameter and the mass are determined for the same size distribution. The APM output number concentration at voltage V_1, $N_o(V_1)$, is a convolution of the size distribution exiting the DMA and the APM transfer function, $T(m,V_1)$:

$$N_o(V_1) = \int_0^\infty G(m)T(m,V_1)dm \ . \qquad (3\text{-}12)$$

The size distribution is obtained based on measurements of the output APM number concentration versus voltage using a gradient search optimization to minimize the Chi-squared (χ^2) function (Emery, 2007). This approach also allows the calculation of the uncertainty in the mass based on the fitting procedure and is found to be on average 3.4 % of the measured mass (see Table 3-2). It is found that the error in estimating the peak in the mass distribution from a Gaussian fit of $N_o(m(V_1))$ is on average 0.8 % for the range of sizes considered.

The combined relative uncertainty for the mass, $u_c(m)$, is obtained as the square root of the sum of squares (RSS) of the CV for the calibration procedure, repeatability, and inversion. The values of $u_c(m)$ range from 0.061 to 0.090 with a mean value of 0.068. The largest uncertainty is for the smallest mass, 2.9×10^{-16} g, which corresponds to a 50 nm mobility diameter.

Using the DMA-APM, the masses of the agglomerates were determined as a function of the mobility diameter over a range from about 50 nm up to 300 nm. The volume equivalent diameter is computed from the following equation:

$$m = \frac{\rho\pi d_{ve}^3}{6} \quad , \qquad (3\text{-}13)$$

where ρ is the density of silver (1.05×10^4 kg/m^3). The dynamic shape factor κ is computed using Eq. (3-9). The equation (Kim et al., 2005) used for $C_c(d_{ve})$ is given by

$$C_c(d_{ve}) = 1 + Kn_{ve}\left[A_1 + A_2 \exp(-A_3 / Kn_{ve})\right] \ , \qquad (3\text{-}14)$$

where $Kn_{ve} = 2\lambda / d_{ve}$, A_1=1.165, A_2=0.483, and A_3=0.997.

3-3. Results and discussion

3-3-1. Dynamic shape factor of silver agglomerates

The results are shown in terms of the dynamic shape factor versus the mobility diameter (Figure 3-4). It is seen that κ increases to a value of 3 - 4 for a mobility diameter of 300 nm. The results for silver agglomerates obtained by Schmidt-Ott (1988) are included in Figure 3-4. The results given in Figure 7 of his paper are expressed in terms of κ_E, the experimental dynamic shape factor, which is related to the mobility radius dynamic shape factor κ_R (defined by Eq.(3-10) above) by the expression:

$$\kappa_R = F_f^{-1/3} . \kappa_E = 1.126 \cdot \kappa_E , \qquad (3\text{-}15)$$

where F_f (=0.7) is the filling factor for a close-packed agglomerate.

From Figure 7 of the paper (Schmidt-Ott) and Eq. (3-15), both R_m and R_{ve} were estimated and then κ was computed by using Eq. (3-9) together with the slip correction formula in Eq. (3-14).

3-3-2. Uncertainty in dynamic shape factor

The uncertainty in the measurement of the dynamic shape factor, $u(\kappa)$, can be computed from the uncertainty in d_m and m using the law of propagation of uncertainty:

$$u^2(\kappa) = \left(\frac{\partial \kappa}{\partial d_m} u(d_m) \right)^2 + \left(\frac{\partial \kappa}{\partial m} u(m) \right)^2 . \quad (3\text{-}16a)$$

Using Eq. (3-9), one obtains the following expression for the relative uncertainty in κ:

$$u_r^2(\kappa) = \frac{u^2(\kappa)}{\kappa^2} = u_r^2(d_m) \left[1 - \frac{d_m C'(d_m)}{C(d_m)} \right]^2 + \frac{1}{9} u_r^2(m) \left[1 - \frac{d_{ve} C'(d_{ve})}{C(d_{ve})} \right]^2 . \quad (3\text{-}16b)$$

In Eq. (3-16b), the primes indicate the differentiation of slip correction factor with respect to d_m or d_{ve}. The relative uncertainty for d_m is 0.04 and for m is estimated as the mean uncertainty equal to 0.068. The value of $u_r(\kappa)$ ranges from 0.07 to 0.08 for both the Set 1 data and for the Set 2 data. The repeatability of the 2008 data as defined by the relative standard deviation of the mean for each value of d_m ranged from 0.01 to 0.03. Adding this component of uncertainty in quadrature to $u_r(\kappa)$ increases $u_r(\kappa)$ by at most 0.005.

3-3-3. Comparison of measured dynamic shape factor with model predictions

In this section, measurement results obtained from this study are compared with other measurements and model predictions. It is of interest to compare the two model predictions with the experimental data. The dependence of κ on d_m for the Chan-Dahneke model is obtained by equating the friction coefficient in Eq. (3-2) or (3-3) to the friction coefficient of a sphere with diameter d_m:

$$\frac{\left[c_{bcu}^*(N-1) + c_{sph}^* \right] \mu d_p^2}{4\lambda} = \frac{3\pi \mu d_m}{C_c(d_m)} \quad , \quad \text{N<12}$$

$$\frac{c^*_{avg} N \mu d_p^2}{4\lambda} = \frac{3\pi \mu d_m}{C_c(d_m)} \qquad , \qquad N \geq 12 \, . \tag{3-17}$$

For a given value of N and a fixed value of the primary diameter d_p, the mobility diameter d_m can be computed from Eq. (3-17). From N and d_p the volume equivalent diameter d_{ve} can also be determined. Then from the values of d_m and d_{ve} the value of κ is computed by using Eq. (3-9). In the free molecular limit and the limit where d_m much larger than the mean free path, explicit expressions are obtained for κ for the case $N \geq 12$:

$$\kappa = \left(k_1 d_m / d_p\right)^{2/3} \quad , \text{ free molecular} \tag{3-18a}$$

$$\kappa = \left(k_1 d_m / d_p\right)^{1/3} \quad , \quad d_m >> \lambda \tag{3-18b}$$

where $k_1 = \left(\frac{c^*(A_1 + A_2)}{6\pi} \right)$.

The Meakin results for the computer simulations of ballistic collisions with agglomerates are expressed by Eq. (3-4). For the case of diffuse reflection, the reduced projected cross section averaged over three orthogonal orientations is given by

$$S_{pa,r}(N) = 0.264N + 0.519N^{0.825} \quad , \text{ for } \quad N \leq 100$$

$$S_{pa,r}(N) = 0.240N + 0.517N^{0.847} \, , \text{ for } \quad 100 < N \leq 2500 \, . \tag{3-19}$$

The reduced projected area is based on a diameter of unity for the primary sphere so the actual projected area is given by:

$$S_{pa}(N) = d_p^2 S_{pa,r}(N) \, . \tag{3-20}$$

The slight variation in δP for the case of diffuse reflection is estimated from Figure 3-6 (b) of Meakin. The molecular properties are based on nitrogen gas at 296.15 K and 1.0133×10^5 Pa.

The experimental results for the dynamic shape factor for silver agglomerates are plotted vs. d_m (Figure 3-4). The value of d_p used in the theoretical calculations, Eq. (3-17) and Eq. (3-20), is 15 nm for comparison with the Schmidt-Ott's data and 16.2 nm for Set 1. All of the model predictions approach κ =1 at a size of about 15 nm, since the dynamic shape of the primary sphere with a diameter of 15 or 16.2 nm is by definition 1. The Meakin predictions exceed the results of Set 1 by about 10 % for the smaller values of d_m and by up to 30 % for the 300 nm agglomerates. The Chan- Dahneke predictions exceed the results of Set 1 by about twice as much as the Meakin predictions. The Mackowski predictions, which are not shown, would lie between the other two model predictions. The likely reason for the better agreement with the Meakin prediction is that this model takes into account the shielding of one part of fractal agglomerate by another part while such screening is not present for the straight chain model of Chan-Dahneke. The orientation average projected area for the Meakin model is proportional to N^x where $x \approx 0.90$ while the projected area of an orientation averaged chain of spheres is proportional to N. The decrease in the dynamic shape factor for the larger primary spheres for the Set 2 compared to the Set 1 is qualitatively consistent with the theoretical calculations.

The Chan-Dahneke predictions appear to agree well with the Schmidt-Ott's data, which are obtained for smaller agglomerates than this study. His measurements of κ exceed the measured values with DMA-APM by more than three times the

measurement uncertainty in this study. Possible causes of this discrepancy include errors in the measurement of the primary sphere size and in the filling factor of 0.7 in Eq. (3-15). In order to account for the discrepancy between Schmidt-Ott's measurements of κ and the measurements of κ based on primary sphere size effect in Eq. (3-18a), either the primary sphere measured by Schmidt-Ott would have to increase by 1.7 or the primary sphere size used in this study decrease by a factor of 1.7. Such a large TEM measurement error seems unlikely. For the filling factor F_f, one finds that the κ decreases by 20-25 % as the filling factor increases from 0.7 to 1.0. Thus, using the F_f of 1.0 will reduce the discrepancy between measurements from this study and Schmidt-Ott's measurements by about a factor of three.

3-3-4. Comparison of measured friction coefficient with model predictions

It is of interest to compare the experiments and model predictions in terms of the friction coefficient as a function of the number of primary sphere. This provides the most direct test of the models for the friction coefficient.

Equations (3-2), (3-4), and (3-20) give the predicted N dependence for the two model calculations. The experimental friction coefficient is computed from the mobility diameter and the number of primary spheres determined from the primary sphere diameter and either the mass of the agglomerate (current method) or the diameter of the fully sintered agglomerates (Schmidt-Ott, 1988). For a single sphere with the size of 16.2 nm, the friction coefficients are 1.99 E-13 kg/s for Chan-Dahneke based on free molecular friction coefficient for sphere with 93 % diffuse reflection, 2.17 E-13 kg/s for

Meakin extrapolated to a single sphere, and 1.91 E-13 kg/s from Cunningham-Stokes's relation in the free molecular limit (Eq. (3-1)).

Figure 3-5 compares the measured and predicted friction coefficients. The exponent characterizing the power law dependence of the friction coefficient on N is defined as η.

$$f = A_f N^{\eta} \ . \tag{3-21}$$

From Set 1, the exponent η characterizing the power law dependence of friction coefficient on N is 0.751 ± 0.020(T=25 ^{o}C) and 0.760 ± 0.020 (T=100 ^{o}C) for N between 40 and 600, which is equivalent to d_m in the range of 100 nm to 300 nm. Similar results were obtained in 2008 with a mean value of the six repeat measurements (See Table 3-3) equal to 0.751. The best estimate of η is the mean of the eight measurements, 0.752 with a standard deviation of the mean equal to 0.011. The uncertainty estimates for η are discussed below. The values of η from the theoretical studies are 0.999 by Chan-Dahneke and 0.908 by Meakin for the same range in N. The mean value of η obtained by Mackowski is 0.94 with a variation of about ± 0.03 and the prefactor varied by about a factor of 2. This value is slightly larger than the value obtained by Meakin. The difference may result from the different structure of the agglomerates. The Meakin's agglomerates are formed by a random combining of smaller agglomerates while Mackowski's algorithm for generating agglomerates constrains the orientation of contact of two agglomerates so that the resulting radius of gyration fits the fractal equation.

3-3-5. Dependence of friction coefficient on number of primary particles

To obtain a higher resolution comparison of the theory and experiment, the ratio of the measured friction coefficient to the Meakin expression, f/f_{Meakin}, is plotted in Figure 3-6. The expression for Meakin is obtained from a power law fit of the simulations for N in the range of 2 to 40.

$$f_{Meakin} = 2.159 \times 10^{-13} \left(\frac{d_p}{d_{p,0}} \right)^2 N^{0.888} \; kg/s \,, \tag{3-22}$$

where $d_{p,0}$ = 16.2 nm. The data of Schmidt-Ott for smaller silver agglomerates is also included in Figure 3-6. The constant off-set of about 0.3 between results from this study and Schmidt-Ott's results may be from an error in the measurement of the primary sphere size. The filling factor F_f has no effect on the friction coefficient ratio. From Eq. (3-22) one can see that f_{Meakin} increases with $d_p{}^2$. Thus, a 13 % change in d_p results in a 30 % change in the friction coefficient ratio. So in this case, TEM measurement errors could account for much of the discrepancy.

As a point of reference, the reduced data in Figure 3-6 for Schmidt-Ott correspond to the friction coefficient varying as $N^{0.859}$ relative to the Meakin exponent of 0.888. Also, fitting a power law to the first three points (50 nm, 80 nm, and 100 nm) of 100 ^{o}C data in Set 1 resulted in a slightly larger η with a value of 0.87. The uncertainty in η in the case is large because of the small number of points and because the smallest mass is near the minimum mass that can be measured by this APM. Cai and Sorensen (1994) obtained η equal 0.86 (x = 0.43) for soot agglomerates in a flame using a combination of dynamic and static light scattering. In this experiment, both the

primary particle diameter and the mobility diameter are in the free molecular limit, while Schmidt-Ott's measurements and measurements in this study are partly in the transition region. The agreement may be a bit fortuitous considering the experimental issues and measurement range, but it still suggests at least rough agreement with the Meakin prediction.

The variation in the Set 2 is also likely from different primary sphere sizes as a result of slightly different temperature/vaporization rates in the furnace and cooling rates at the exit of the tube furnace. A 2.5 % change in the primary sphere size would result in a change in the friction coefficient ratio equal to the observed standard deviation of the ratio, which is about 5.1 % of the mean value. The slight systematic difference in the friction coefficient ratio between the Set 1 and Set 2 is likely a result of using a different DMA and a different calibration procedure.

The key finding of this study is that in the transition region with N between 40 and 600 (d_m between 100 and 300 nm) the friction coefficient decreases by about 32 % relative to the free molecular prediction based on the Meakin model (Figure 3-6). The decrease is slightly smaller relative to the power law behavior based on either the Schmidt-Ott data (η = 0.86) or data from this study for the smallest three agglomerates (η = 0.87). The exponent characterizing the N dependence of the friction coefficient ratio is 0.141, which is equivalent to an exponent of 0.751 for the friction coefficient itself compared to the Meakin value of 0.888. This decrease is a result of a flow interaction between the primary particles. A theory for the flow interaction between particles for two length scales, one small compared to the mean free path and the other large compared to the mean free path, does not exist.

An analytic approximation to the behavior of f/f_{Meakin} based on the experimental data plus the small N limit has been obtained as follows:

$$f / f_{Meakin} = 1.0 \times \exp(-N/182) \quad N < 40$$

$$f / f_{Meakin} = 1.392 N^{-0.141} \quad , \; 600 > N \geq 40 \; . \tag{3-23}$$

In Figure 3-6, the red short dash line and short dash dot line indicate uncertainty ± 0.02 in the power exponent, -0.141 in Eq. (3-23). The slope of the friction coefficient ratio may decrease below the expression in Eq. (3-23) with increasing number of spheres beyond 600. Wang and Sorensen (1994) found that the ratio of the mobility radius to the radius of gyration was 0.7 for TiO_2 agglomerates with a primary sphere size of about 35 nm and the average radius of gyration ranging from 500 nm to 2000 nm. The range in the Knudsen number based on the radius of gyration for the ambient pressure measurements was 0.03 – 0.13. The corresponding range in the mobility radius d_m is 700 nm – 2800 nm. The exponent η was estimated based on the dependence of f on mobility radius and on the fractal relation between the radius of gyration and the number of primary particles in the agglomerate:

$$f \propto \frac{R_m}{C_c(R_m)} \propto R_m^{\delta} \propto R_g^{\delta} \propto \left(N^{1/D_f}\right)^{\delta} \propto N^{\delta/D_f} \; . \tag{3-24}$$

From a power law fit of f vs. R_m over the range in the mobility radius, one finds δ = 1.091. Using this value in Eq. (3-24) and a fractal dimension of 1.75, one obtains η = 0.623. In Figure 3-6, the friction coefficient ratio for d_m equal to 700 nm and 2800 nm are plotted. The calculation assumes a fractal prefactor of 1.3. In this case the power law has decreased to a value of -0.275, compared to a value of -0.141 for the expression in Eq. (3-23). This result is suggestive but not directly comparable because of different

primary sphere size of about 35 nm compared to 16 to 19.5 nm used in this study. The dependence of the friction coefficient on the primary sphere diameter is known for free molecular flow, but it is not known for this unsolved flow interaction problem where there is one length scale smaller than the mean free path and one larger. Thus data are needed for the friction coefficient as function of primary sphere size and number.

The key focus in this study is the N dependence of the friction coefficient. This information may be relevant to Wang and Sorensen (1994)'s concern about the ratio R_m/R_g undershooting the continuum limit, which is assumed to be R_m/R_g equal a constant of order unity, in the case of agglomerates made up of small primary particles. It may be that the changing N dependence of the friction coefficient with increasing agglomerate size prevents the undershooting or leads to a large agglomerate limit different than R_m proportional to R_g.

A deviation plot of the measured versus the fitted friction coefficient for each set of data is shown in Figure 3-7. It is seen that the 100 ^{o}C data has a parabolic shape indicating systematic deviations from a power law fit. There is also a slight systematic trend for the January 12 data of Set 2. For the relatively small number of data points, 4 to 6, and small range, a power law fit provides a good fit except for the 100 ^{o}C data. However, there is the caveat that over a wide range in N as one goes from the free molecular to the transition region, one expects a systematic decrease in the slope as suggested in Figure 3-6.

3-4. Conclusions

A quantitative method for measuring κ and the exponent η were developed with an uncertainty of 6 % to 7 % for κ and about 3 % for the exponent for agglomerates with mobility diameter in the range 50 nm to 300 nm. The major contributor to the uncertainty is from the calibration of the APM. The measured value of η in the size range less than 100 nm agrees within a few percent with the predictions of Meakin and with other measurements in this size range. For larger agglomerates with d_m from 100 nm to 300 nm, the measured η decreases by 15 % while the predicted value increases by about 1 %. An empirical equation is given for the N dependence of the ratio of the measured friction coefficient to the Meakin free molecular expression. The observed decrease in η with increasing agglomerate size suggests a flow interaction between the primary particles not included in the existing models which are based on free molecular dynamics.

Components	Length, cm	I.D., cm	Residence time, s[a]	Temperature, °C
Generator	89[b, c] (Heated region)	1.43[b, c]	5.7[b, c]	1150[b] 1169[c]
Agglomeration chamber	2.7 L[b] 6.7 L[c]	15[b] 20[c]	120[b] 300[c]	25 [b, c], 100[d]

[a] Residence time computed based on a flow of 1.5 L/min at 25 °C and the reactor at 25°C in the particle generation furnace.

[b] Condition for experiments done in March 2007

[c] Condition for experiments done in January 2008

[d] Same conditions as March 2007 except 2nd furnace heated to 100 ^{o}C.

Table 3-1. Experimental conditions for generation of agglomerate particles

Temp.	Dm (nm)	Mass (fg)	Fitting CV	Mass (fg) Gaussian	Repeatability CV	$u_c(m)$
R.T.	50	-				
	100	1.07	0.028	1.08	0.009	0.065
	150	2.56	0.047	2.59	0.001	0.075
	200	4.87	0.018	4.89	0.005	0.061
	250	7.36	0.031	7.36	0.003	0.066
	300	10.40	0.028	10.55	0.003	0.064
100 °C	50	0.29	0.069	0.29	0.003	0.090
	80	0.77	0.039	0.77	0.002	0.070
	100	1.22	0.025	1.22	0.001	0.063
	150	2.82	0.028	2.82	0.004	0.065
	200	5.09	0.028	5.30	0.021	0.067
	300	11.67	0.028	11.77	0.011	0.065

Table 3-2. Difference in two different fitting methods in terms of mass

Date	η
03/15/07[a]	$f = 3.32E\text{-}13\ N^{0.751}$
03/29/07[b]	$f = 2.95E\text{-}13\ N^{0.760}$
50 nm -100 nm	$f = 1.86E\text{-}13\ N^{0.872}$
$\eta = 0.755 \pm 0.006\ (0.004)$ [c]	
01/04/08[d]	$f = 4.68E\text{-}13N^{0.738}$
01/04/08[e]	$f = 4.38E\text{-}13\ N^{0.739}$
01/05/08[f]	$f = 3.99E\text{-}13\ N^{0.757}$
01/07/08[g]	$f = 3.50E\text{-}13\ N^{0.771}$
01/11/08[h]	$f = 4.18E\text{-}13N^{0.753}$
01/12/08[i]	$f = 4.27E\text{-}13\ N^{0.745}$
$\eta = 0.751 \pm 0.0124\ (0.005)$ [c]	
$\eta_{tot} = 0.752 \pm 0.0109\ (0.004)$ [c]	

[a] d_m = 100 nm (N=46), 150 nm (N=110), 200 nm (N=208), 250 nm (N=315), 300 nm (N=445)
[b] d_m = 100 nm (N=33), 150 nm (N=52), 200 nm (N=121), 250 nm (N=218), 300 nm (N=499)
[c] first number is mean value, second is standard deviation, third is standard deviation of the mean
[d] d_m = 100 nm (N=30), 150 nm (N=81), 200 nm (N=130), 300 nm (N=320)
[e] d_m = 100 nm (N=33), 150 nm (N=85), 200 nm (N=159), 250 nm (N=229)
[f] d_m = 100 nm (N=36), 150 nm (N=78), 200 nm (N=166), 250 nm (N=232)
[g] d_m = 100 nm (N=39), 150 nm (N=93), 200 nm (N=161), 250 nm (N=259)
[h] d_m = 80 nm (N=19), 100 nm (N=34), 150 nm (N=81), 200 nm (N=149), 250 nm (N=232), 300 nm (N=317)
[i] d_m = 80 nm (N=20), 150 nm (N=80), 250 nm (N=234), 300 nm (N=334)

Table 3-3. Power law dependence for friction coefficient vs. *N* over limited ranges

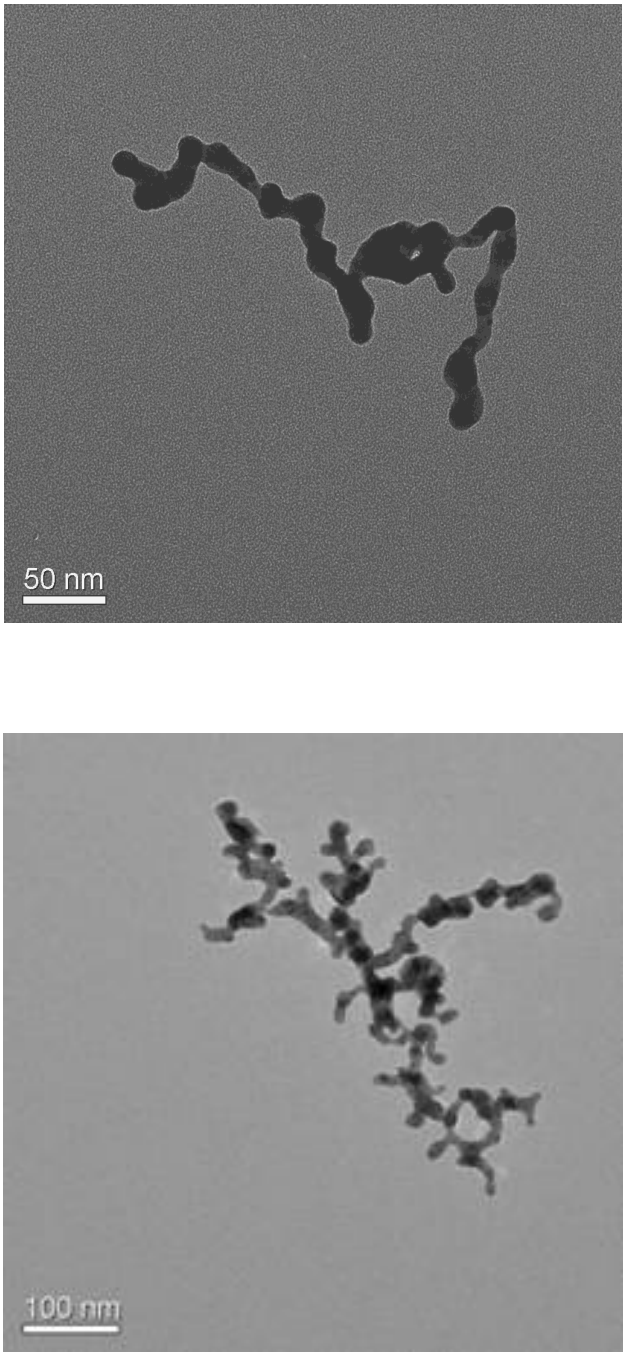

Figure 3-1. TEM images of Ag Agglomerates: d_m = 100 nm (top) and d_m = 200 nm (bottom)

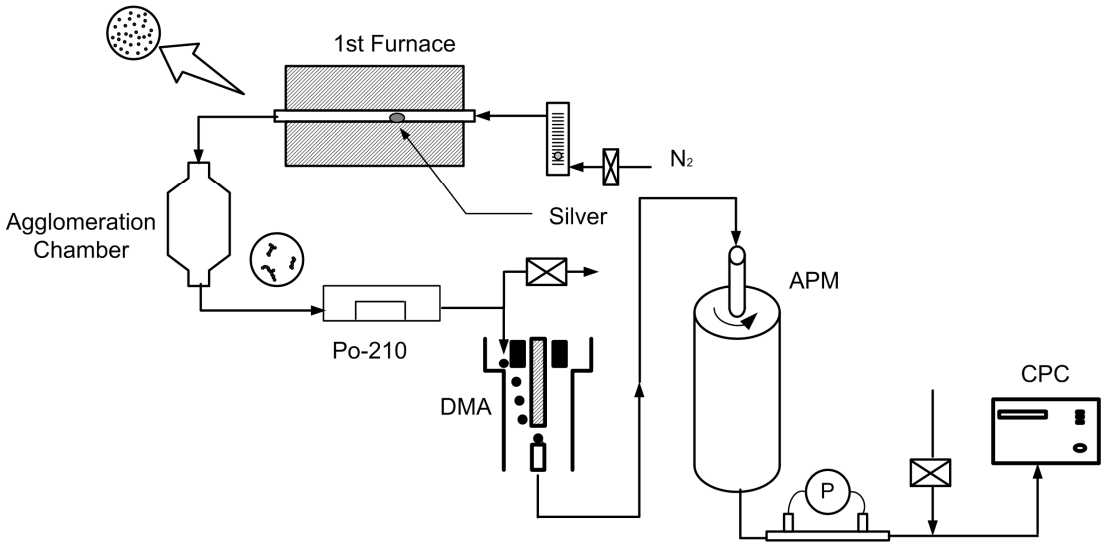

Figure 3-2. Schematic diagram for the measurement of dynamic shape factor using DMA and APM. For the Set 1 experiments a second tube furnace was inserted between the agglomeration chamber and the DMA

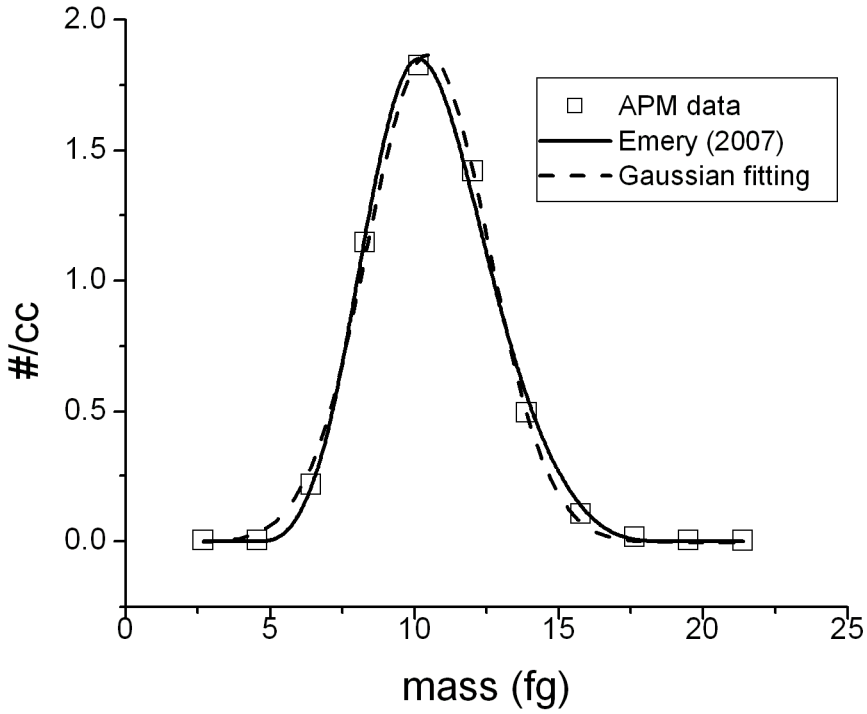

Figure 3-3. The number concentration as a function of mass passing through the APM for d_m = 300 nm at room temperature

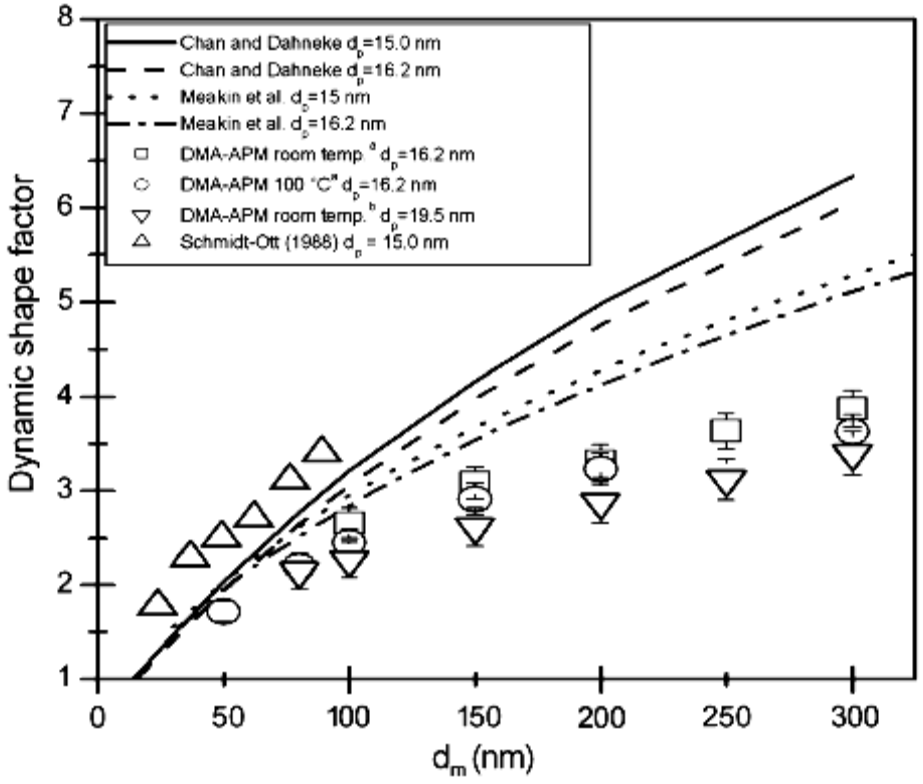

Figure 3-4. Comparison of measured dynamic shape factor ([a] Set 1, [b] Set 2) as a function of d_m of silver agglomerates with prediction of Chan-Dahneke and Meakin (values of d_p for model comparison: 15 nm for Schmidt-Ott (1988) and 16.2 nm for Set 1)

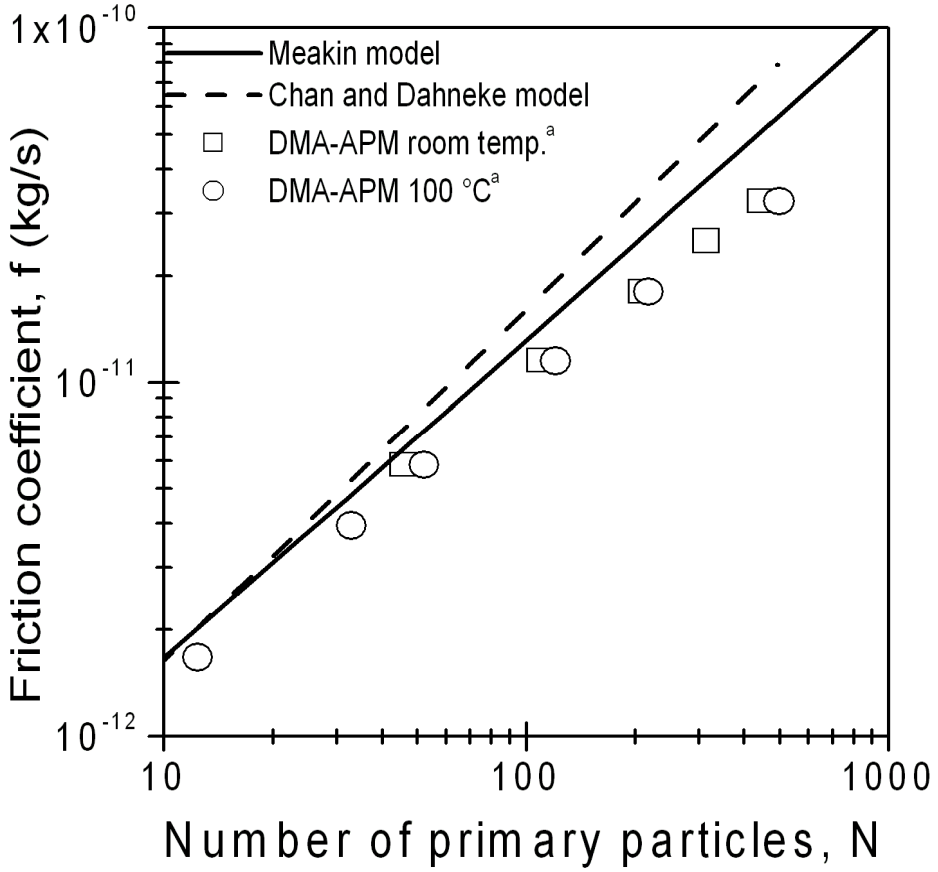

Figure 3-5. Dependence of friction coefficient on the number of primary sphere: [a] Set 1

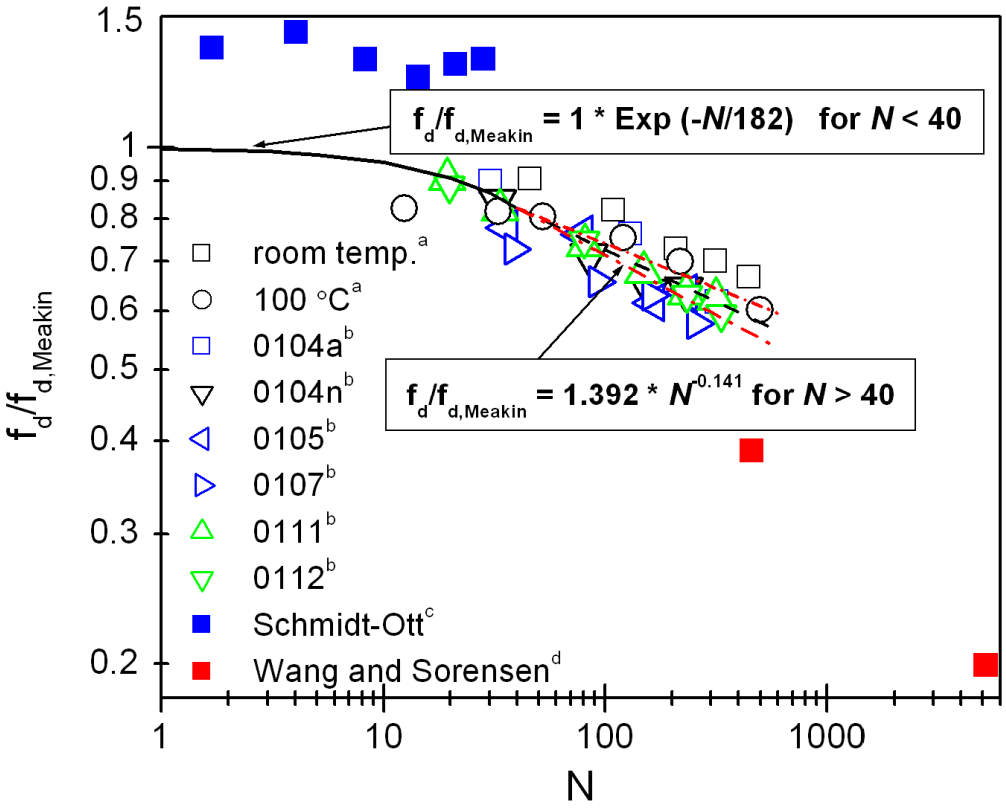

Figure 3-6. The ratio of the measured friction coefficient to the Meakin expression: red short dash line and short dash dot line indicate uncertainty ± 0.02 in the power exponent, -0.141 in Eq. (3-23). [a] Set 1, [b] Set 2, [c] Schmidt-Ott (1988), [d] Wang and Sorensen (1994)

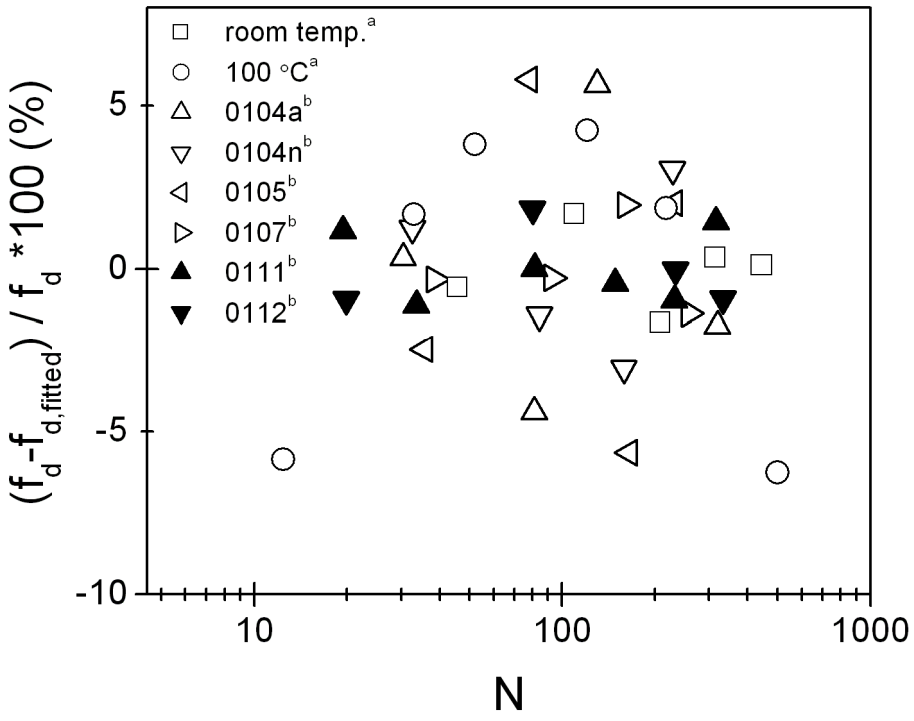

Figure 3-7. Deviation plot of the measured versus the fitted friction coefficient for each set of data: [a] Set 1, [b] Set 2

Chapter 4 Mass and Mass-Mobility Diameter Scaling Exponent of Agglomerate Particles in the Transition Regime

4-1. Dependence of mass on mobility diameter

One other comparison of interest is the fractal-like plot of the agglomerate mass as a function of the mobility diameter. In Figure 4-1, m is plotted vs. d_m for d_p = 16.2 nm for the two theories. From Eqs. (3-3), (3-8), and (3-13) the following expression is obtained between the mass and d_m for the model of Chan-Dahneke (1981):

$$m = \rho \frac{d_m}{C_c(d_m)} \frac{2\pi^2 \lambda}{c^*} d_p \ . \qquad (4\text{-}1)$$

A value of mean free path of nitrogen of 66.3 nm at 23 ^{o}C and 101.3 kPa from the study by Hirschfelder et al. (1954**)** was used in the analysis in Eq. (4-1) as well as other equations containing the slip correction.

The mass measured by Schmidt-Ott (1988) is1.58 times greater than the measured mass for d_m = 50 nm, 80 nm. Possible causes include errors in the measurement of the primary sphere size and in the filling factor of 0.7 in Eq. (3-15). If there is a 50 % error in the measurement of primary sphere size in Schmidt-Ott's study or in this study, the discrepancy would be removed. However, such a large error in the TEM measurement is unlikely. One finds that the mass measured by Schmidt-Ott would be increased by about 40 % if the filling factor is increased from 0.7 to 1.0. Thus,

for F_f equal to 1.0, the two mass measurements will agree within the uncertainty range of mass measurement in this study. The mass-mobility diameter scaling exponent D_{fm} characterizing the power law dependence of the mass on the mobility diameter is defined as

$$m = k_m \, d_m^{D_{fm}} \quad . \tag{4-2}$$

The quantity is obtained for the measurements and the models. The model calculations are carried out for a primary sphere diameter of 16.2 nm. The best fit values of D_{fm} are 2.080 at room temperature and 2.055 at 100 °C for d_m in the range of 100 nm to 300 nm. This value of 2.08 is 17 % larger than the value of 1.72 predicted by the Meakin model and 25 % larger than the prediction based on the Chan- Dahneke model based on the range for the mobility diameter. The best power law fit for the data obtained in Set 1 and Set 2 are presented in Table 4-1. The average of all the measurements, 2.103, is taken as the best estimate of D_{fm}. The results of Set 2 are expected to give a more accurate average value because of the larger number of repeats and because a systematic effect was observed for the data set collected at 100 ^{o}C in Set 1.

4-2. Measurement uncertainty in D_{fm}

The difference between the average of all tests and the average for the Set 2, 0.011, is small compared to the measurement uncertainty in determining D_{fm} which is shown below to be about 0.065. In Figure 4-1, the short dash line and short dot line indicate the uncertainty, ± 0.065 in the best estimate of D_{fm}, 2.103 in room temperature data of Set 1. The uncertainty in the best estimate of D_{fm} can change mass of d_m = 300

nm by ± 7.4 %. Also, horizontal and vertical error bars marked on square symbols represent calibration uncertainties in DMA, 4 % and in APM, 6.8 %.

The measurement uncertainty in D_{fm} arises from fitting the data to a power law expression, from the propagation of the uncertainties from the measured mass and mobility diameter, and from the repeatability uncertainty. The relative uncertainty, $\sigma_A(D_{fm})$, obtained from a linear least square analysis of the variables $\ln(m)$ and $\ln(d_m)$ ranges from 0.011 to 0.019 and the larger value was used as the estimate of the uncertainty.

The estimated uncertainty in d_m given above was 4 % of the value. A constant percentage change will not affect the slope for a log-log plot. However, a more careful analysis indicates that the likely error in measuring d_m depends slightly on particle size. A likely source of the error in the d_m measurement is an error in the flow measurement. A constant error in the flow measurement will result in a constant error in the mobility, but not quite a constant change in d_m and random. For example, a flow decrease of 4.4 % in the DMA will result in 4.4 % decrease in the electrical mobility and a 3.0 % increase in d_m for d_m equal 200 nm, but this same change in flow will result in a 2.7 % increase in d_m for d_m equal 100 nm. Using Eqs. (3-6) and (3-7), one can estimate the change in the measured values of d_m resulting from a 4.4 % decrease in the mobility. The best fit value for D_{fm} decreases fractionally by 0.005 based on the modified mobility diameters. This value is used as the relative uncertainty component, $u_{B1}(D_{fm})$.

The last term in the uncertainty analysis is the mass. Above the combined relative mass uncertainty was estimated as 0.068. An uncertainty in the mass proportional to the mass does not affect the slope. As in the DMA, there are possible

systematic effects such as the rotation speed or geometrical dimensions of the instrument that could affect the results. However, the calibration results presented above indicate large changes in the calibration constant as a function of size. The cause of these changes is not known. An estimate of the impact of this variability is obtained by assuming that the difference between the true mass and the measured mass increases linearly with mass starting at zero difference at the smallest size and increasing to a 5.5 % difference at the largest size of 300 nm. The value of 5.5 % is the approximate calibration measurement uncertainty used in this study. The fractional change in the fractal exponent, $u_{B2}(D_{fm})$, is found to be 0.024.

The relative repeatability uncertainty, $u_R(D_{fm})$, is estimated as the standard deviation of all the repeat measurements for D_{fm} divided by the average value. From Table 5-1 one finds the value to be 0.005.The total relative uncertainty in D_{fm} is obtained by taking RSS of $\sigma_A(D_{fm})$, $u_{B1}(D_{fm})$, $u_{B2}(D_{fm})$, and $u_R(D_{fm})$ with the result $u_{tot}(D_{fm}) = 0.031$, which corresponds to $D_{fm} = 2.103 \pm 0.065$.

The same general approach is used for estimating the uncertainty in η as for D_{fm}; however, in this case, a constant error in the flow does not affect the exponent, because the friction coefficient is inversely proportional to the flow. The individual components are found to be $\sigma_A(\eta)=0.005$, $u_{B1}(\eta)=0$, $u_{B2}(\eta)=0.025$, and $u_R(\eta)=0.005$. The value of $u_{tot}(\eta)$ computed from the RSS of the components is 0.026, which corresponds to $\eta = 0.752 \pm 0.020$.

The measured values of D_{fm} for the 100 ^{o}C data of Set 1 are 2.055 for the size range of 100 nm to 300 nm and 2.074 based on the sizes of 50 nm, 80 nm, and 100 nm. This small change of about 1 % is much less than the 15 % change predicted from the

Meakin model, 1.722 for the larger size range and 2.028 for the smaller range. In Chapter 3, it is shown that the Meakin model predicted a small change in η of about 1 % for these ranges of mobility size. The large change in D_{fm} results from the slip correction term in the relation between the friction coefficient and the mobility diameter as given in Eq. (3-8). Over a small range in d_m, one can approximate the relationship as a power law dependence with exponent δ:

$$f = c_1 d_m^{\delta} \quad . \tag{4-3}$$

The value δ varies by about 15 % from 1.55 to 1.81 for the larger range of d_m (100 nm – 300 nm) to the smaller (50 nm to 100 nm). From Eqs. (3-23), (4-2), and (4-3), one finds that $D_{fm} = \delta/\eta$. In the case of the Meakin model, D_{fm} increases by about 15 % because δ increases about 15 % while η is approximately constant. The experimental situation is different. The exponent δ increases by the same amount as in the model, but the exponent η is increasing by a similar amount so that the ratio, which is equal to D_{fm}, is relatively constant.

Wang and Sorensen (1994) previously reported a similar finding about the constancy of D_{fm} based on three data sets. They found a value of about 0.45 for the exponent x characterizing the power-law dependence of the mobility radius on the number of primary particles. The exponent x equals $1/D_{fm}$ so that the corresponding value of D_{fm} is 2.22. The data sets included inflame agglomerate soot (Cai and Sorensen, 1994), which is in the free molecular region, silver agglomerate (Schmidt-Ott), which extends from free molecular to the transition region, and TiO_2 and Si agglomerates (Rogak et al., 1993), which extends from the transition region to a minimum Knudsen number based on the radius of gyration of 0.13. The total variation

in the exponent D_{fm} was about 6 % across the flow regime from free molecular to near continuum. Wang and Sorensen focus on the dependence of the ratio of the mobility radius to the radius of gyration, R_m/R_g, on the Knudsen number for the agglomerate. A key idea in their explanation of a universal dependence of the ratio on the Knudsen number is the requirement that in all cases the N=1 limit for the ratio is 1.29. So there are two independent explanations for the same effect. More work is needed to assess whether these approaches are equivalent or, if not, which is correct.

4-3. Multiple charging artifact

Doubly charged particles with different mass to charge ratios than the singly charged particles will exit the DMA along with the singly charged particles. The effect of these particles on the mass measured by the APM is estimated. Some fraction of the nanometer-sized agglomerates exiting from the DMA will have two charges. While these doubly charged particles have the same mobility as the singly charged particles, their mass divided by charge will be different than for the singly charged particles will be different. The presence of two overlapping size distributions for the singly and doubly charged agglomerates will result in a difference between the overall peak in the measured distribution and the peak in the distribution of the singly charged agglomerates. It is the peak in the distribution of the singly charged agglomerates that is the quantity of interest. To assess this effect, the masses m_1 and m_2 of the singly and doubly charged agglomerates are first computed.

From Eq. (4-2), one can express m_2/m_1 as a function of the ratio of the mobility diameters of the doubly and singly charged agglomerates, d_{m2} and d_{m1}:

$$\frac{m_2}{m_1} = \left(\frac{d_{m2}}{d_{m1}} \right)^{D_{fm}} . \tag{4-4}$$

By equating the mobility of singly and doubly charged agglomerates using Eq. (3-7), one obtains the following implicit equation for d_{m2} as a function of d_{m1}:

$$\frac{C_c(d_{m2})}{d_{m2}} = \frac{C_c(d_{m1})}{2d_{m1}} . \tag{4-5}$$

For example, for d_{m1} equal 300 nm, one finds d_{m2} equals 510 nm. So by using Eqs. (4-4) and (4-5), one can compute the ratio of m_2/m_1 as a function of d_{m1}. The values of m_2/m_1 are given in Table 4-2 for the range of d_{m1} studied.

The second part of the analysis is to estimate the ratio of the number of doubly charged particles to singly charged particles for DMA size d_{m1}. From measurements of the number concentrations N_1 and N_2 of particles exiting the DMA for the voltage setting corresponding to d_{m1} and d_{m2}, the fraction F_1 of singly charged particles exiting for DMA size d_{m1} is given by:

$$F_1 = \frac{N_1 - f_{21} N_2}{N_1} \quad , \tag{4-6}$$

where f_{21} is the ratio of the number concentration of doubly charged to singly charged particles for agglomerates with mobility diameter d_{m2} exiting a bipolar charger. This first order estimate is obtained using the relationship between the number concentration exiting the DMA and the mobility distribution assuming that the mobility distribution is much broader than the transfer function. Also, N_1 includes singly and doubly charged

particles and N_2 only doubly charged particles. Table 4-2 includes the values of f_{21} for d_{m2}, which are estimated using Wiedensohler (1988)'s approximation for spheres, and the values of F_1 for all of the particle sizes studied.

The APM mass distributions for the singly and doubly charged species are approximated as normal distributions, both with the same value of the coefficient of variation (standard deviation of the mass distribution divided by the peak mass). The values of coefficient of variation are obtained by a best fit of the mass distributions to Gaussians. The peaks for the two Gaussians are given by F_1, for m_1 and 1- F_1 for m_2. The sum of these two normal distributions is fitted with a normal distribution and the modified peak mass along with the reduced standard deviation are given in Table 4-2. The slight decrease in the peak mass leads to an approximately constant increase of about 1 % in κ and a change of only about 0.2 % in η and D_{fm}.

4-4. Conclusions

A quantitative method for measuring the exponent D_{fm} was developed with an uncertainty of about 3 % for the exponent for agglomerates with mobility diameter in the range 50 nm to 300 nm. The major contributor to the uncertainty is from the calibration of the APM. The measured value of D_{fm} decreases by about 1 % as the size range increases while the predicted value of D_{fm} decreases by about 15 %. The near constancy of D_{fm}, which has also been discussed by Wang and Sorensen, is shown to result from both the exponent η and δ decreasing with increasing N. Further work is needed to determine the connection between the explanation for the constancy of D_{fm}

from this study and the earlier explanation by Wang and Sorensen of the universal behavior of R_m/R_g.

Date	D_{fm}
03/15/07[a]	$m = 7.559E\text{-}05 d_m^{2.080}$
03/29/07[b]	$m = 9.477E\text{-}05 d_m^{2.055}$
50 nm -100 nm	$m = 8.705E\text{-}05 d_m^{2.074}$
$D_{fm} = 2.068 \pm 0.018\ (0.013)$[g]	
01/04/08[c]	$m = 7.775E\text{-}05 d_m^{2.110}$
01/04/08[d1]	$m = 6.911E\text{-}05 d_m^{2.150}$
01/05/08[d2]	$m = 9.35E\text{-}05\ d_m^{2.095}$
01/07/08[d3]	$m = 1.17E\text{-}04\ d_m^{2.068}$
01/11/08[e]	$m = 7.73E\text{-}05 d_m^{2.120}$
01/12/08[f]	$m = 7.02E\text{-}05\ d_m^{2.139}$
$D_{fm} = 2.114 \pm 0.030\ (0.012)$ [g]	
$D_{fm,\,tot} = 2.103 \pm 0.032\ (0.011)$ [g]	

[a] d_m = 100 nm (N=46), 150 nm (N=110), 200 nm (N=208), 250 nm (N=315), 300 nm (N=445)
[b] d_m = 100 nm (N=33), 150 nm (N=52), 200 nm (N=121), 250 nm (N=218), 300 nm (N=499)
[c] d_m = 100 nm (N=30), 150 nm (N=81), 200 nm (N=130), 300 nm (N=320)
[d1] d_m = 100 nm (N=33), 150 nm (N=85), 200 nm (N=159), 250 nm (N=229)
[d2] d_m = 100 nm (N=36), 150 nm (N=78), 200 nm (N=166), 250 nm (N=232)
[d3] d_m = 100 nm (N=39), 150 nm (N=93), 200 nm (N=161), 250 nm (N=259)
[e] d_m = 80 nm (N=19), 100 nm (N=34), 150 nm (N=81), 200 nm (N=149), 250 nm (N=232), 300 nm (N=317)
[f] d_m = 80 nm (N=20), 150 nm (N=80), 250 nm (N=234), 300 nm (N=334)
[g] first number is mean value, second is standard deviation, third is standard deviation of the mean

Table 4-1. Power law dependence for mass vs. d_m over limited ranges

d_{m1}(nm)	d_{m2}	m_2/m_1	f_{21}	F_{1avg}	cv*	$m_{modified}/m_{original}$
50	73	2.18	0.913	0.087	0.221	0.992
80	119	2.29	0.191	0.838	0.184	0.978
100	151	2.35	0.259	0.821	0.125	0.978
150	235	2.54	0.408	0.867	0.123	0.986
200	324	2.71	0.517	0.893	0.133	0.990
250	415	2.86	0.591	0.907	0.162	0.989
300	510	3.00	0.639	0.860	0.198	0.980

*cv** - coefficient of variation. at room temp.

Table 4-2. Modified mass through multiple charge correction on DMA-APM data at room temp.

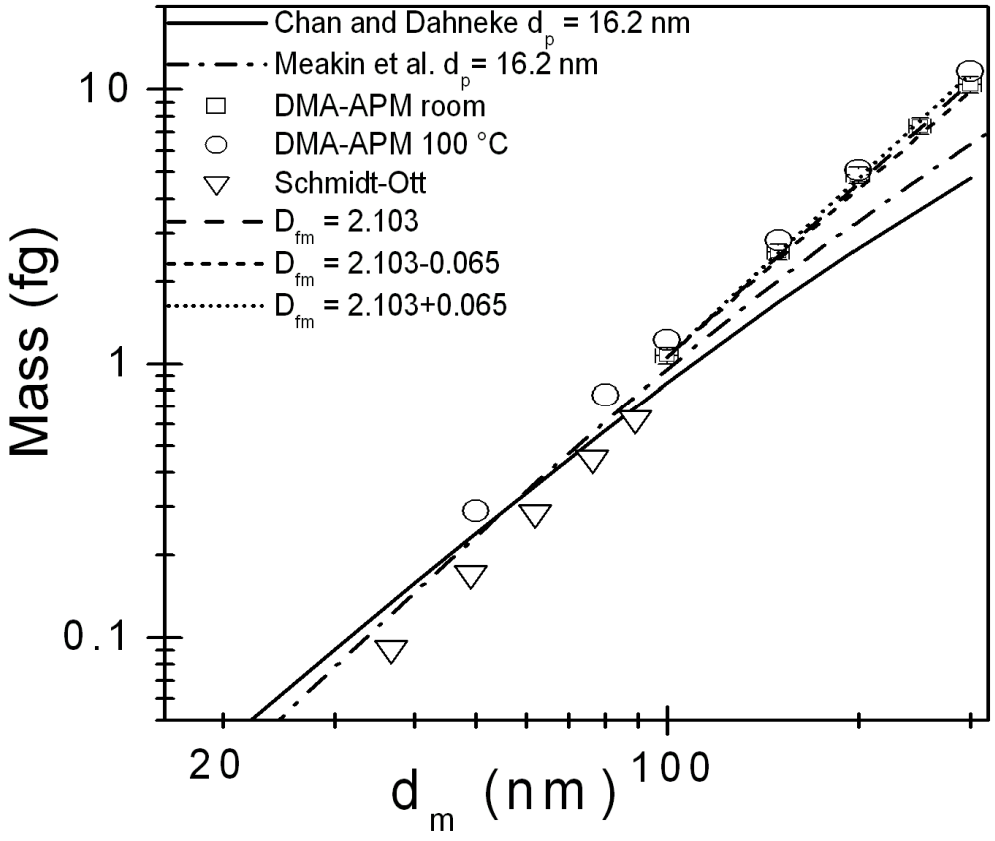

Figure 4-1. Comparison of measured mass as a function of d_m of silver agglomerates with prediction of Chan-Dahneke and Meakin: short dash line and short dot line indicate the uncertainty, ± 0.065 in the mass-mobility diameter scaling exponent, 2.103 and horizontal and vertical error bars marked on square symbols represent calibration uncertainties in DMA, 4 % and in APM, 6.8 %.

Chapter 5 Estimates of Non-ideal Effects on the Friction Coefficient of Agglomerates

5-1. Introduction

It is of interest to make use of analytical models to predict structural and dynamic properties of nanoparticle agglomerates such as dynamic shape factor κ, friction coefficient f, number of primary particles N, and mass-mobility diameter scaling exponent D_{fm}. Chan and Dahneke (1981), Meakin et al. (1989), and Mackowski (2006) have obtained the friction coefficient of agglomerate particle consisting of many primary spheres by doing numerical simulations.

Shin et al. (2009a) experimentally showed that the deviation between the predicted and measured value of dynamic shape factor for silver agglomerates increases with particle size to a value of about 30 %. Also, the dependence of the exponent η, which characterizes the friction coefficient on the number of primary spheres, on particle size is greater than for mass-mobility diameter scaling exponent D_{fm}. On the other hand, model predictions (Chan and Dahneke, 1981; Meakin et al., 1989) indicate that η is independent of agglomerate size while D_{fm} is sensitive to agglomerate size.

The agglomerate particle shown in Figure 5-1 does not match the assumptions for the numerical simulation referenced above. (1) The agglomerates may not be randomly aligned. Studies have shown that agglomerates can be partially aligned in

electric fields (Kousaka et al., 1996; Zelenyuk and Imre, 2007). (2) It is not a loose (‘‘neckless’’) agglomerate. Neck formation can occur in silver agglomerates (Weber and Friedlander, 1997; Lall et al., 2006). (3) Primary particles are not monodisperse. (4) The primary particle size may vary with the size of the agglomerate. In this study, perturbations of the Chan and Dahneke's model are made to estimate these non-ideal effects on the predicted values of dynamic shape factor κ and on the two exponents, η and D_{fm}, for the power law dependence of friction coefficient on the number of primary spheres and of the mass on the mobility diameter.

5-2. Predictions of non-ideal effects on the friction coefficient of agglomerates

The simplest of the three models, the Chan-Dahneke model for a straight chain agglomerate was used as a basic model in this study. Chan and Dahneke (1981) used a Monte Carlo approach to compute the friction coefficient of a straight chain of spherical particles in the free molecular limit based on the Knudsen number of the primary particle diameter ($Kn_p = \lambda / d_p$). The following expression is obtained for the friction coefficient:

$$f = \left(c_{bcu}\left(N-1\right) + c_{sph}\right)\mu\, d_p^2 / 4\lambda \quad , \qquad (5\text{-}1)$$

where c_{bcu} is the dimensionless friction coefficient for a basic chain unit, two hemispheres touching at their poles, N the number of spheres in the chain, μ the gas viscosity, d_p the diameter of the primary sphere, c_{sph} the dimensionless friction

coefficient for a sphere, and λ the mean free path of the gas. Assuming 7 % of the collisions to have specular reflections and 93 % diffuse reflections, Chan and Dahneke (1981) obtained values of 9.17 for c_{bcu}^{r} if the chain is randomly oriented, 6.62 for c_{bcu}^{a} if the chain is aligned in the direction of the chain motion, and 11.44 for c_{sph}.

The quantities of interest are the dynamic shape factor κ, the exponent η characterizing the power law dependence of the friction coefficient on N, and the exponent D_{fm}. This dynamic shape factor is equal to the ratio of the friction coefficient of the agglomerate, f, to the friction coefficient of a sphere with the same condensed phase volume as the agglomerate:

$$\kappa = \frac{f}{f_{ve}} = \frac{f\, C_c(d_{ve})}{3\pi\mu d_{ve}} \quad , \tag{5-2}$$

where the subscript *ve* refers to the volume equivalent sphere and C the Cunningham slip correction. The volume equivalent sphere is computed from N and d_p as:

$$d_{ve} = N^{1/3} d_p \, . \tag{5-3}$$

The following equations define the exponents η and $D_{fm:}$

$$f = A_f N^{\eta} \, , \tag{5-4}$$

$$m = k_m \, d_m^{D_{fm}} \, , \tag{5-5}$$

where A is a prefactor, m mass of agglomerate, and k_m a prefactor.

The quantity d_m is the diameter of a sphere with the same mobility as that of the agglomerate:

$$Z_{aggl.} = \frac{e}{f} = \frac{eC_c(d_m)}{3\pi\mu d_m} \, . \tag{5-6}$$

The mass of the agglomerate is computed using the density of silver ρ and N :

$$m = \frac{\pi}{6} d_p^3 \rho N \,. \tag{5-7}$$

5-2-1. Alignment Effect

The mobility diameter of a nonspherical particle is a function of the particle shape and orientation. The electric field in the DMA can cause nonspherical particles to partially align. The torques arising from the free charge on the agglomerate as well as from the induced polarization causes the alignment. For larger agglomerates where the orientation energy is large compared to kT, the particle alignment leads to a reduction in the friction coefficient. This reduction will in turn result in a reduction of the dynamic shape factor relative to the value for a random orientation, which is assumed for the baseline calculation in this study.

Here an order of magnitude estimate of this change was made for an agglomerate with d_m equal to 300 nm. One assumption is that the agglomerate has a cross structure with the long chain 1.6 times longer than the cross chain. Kim et al. (2009) show that silver agglomerates have the ratio of the maximum projected length divided by the maximum projected width equal to about 1.6. In the current analysis, a primary sphere size is assumed to be 16.2 nm. The Chan and Dahneke's expression for the friction coefficient was used for both the vertical and horizontal chain. The two chains have one sphere in common. Half of this sphere is assumed to be associated

with the longer chain and half with the shorter resulting in the following modification to Chan and Dahneke expression for each chain:

$$f = \left(c_{bcu}\left(N_k - 1 - 1/2\right) + c_{sph}\right)\mu\, d_p^2 / 4\lambda \quad , \tag{5-8}$$

where k = 1, 2 corresponds to the long and short chain.

For a randomly oriented cross with 201 spheres, 126 in the long direction and 76 in the short direction with one sphere shared, the friction coefficient corresponds to a mobility size of 300 nm. For an aligned cross with 220 spheres, 136 in the long direction and 85 in the short direction with one sphere shared, is aligned in the direction of the longest arm of the cross, the friction coefficient corresponds to a mobility size of 300 nm. The value of κ is computed from Eqs. (5-2) and (5-3) for both the randomly oriented cross and the aligned cross. It is found that the dynamic shape factor is about 5 % smaller for the oriented configuration, 5.78, compared to the random configuration, 6.06. Current method of estimating the alignment effect is similar to that used by Rogak et al. (1993).

As the agglomerate size decreases, the tendency to orient decreases. It is assumed that for a mobility size of 50 nm, which corresponds to 10 spheres, the orientation is random. Figure 5-2 shows the effect of alignment on the dynamic shape factor.

Also how this change in orientation would affect the power law expression for the friction coefficient versus N and for the exponent D_{fm} was estimated. The exponents were computed based on two points: one for N = 10 for the cross in a random orientation and the second for N = 201, for which both a random orientation and an aligned orientation are computed. The exponent η decreases by 4.3 % from a value of

1.00 for the aligned orientation versus a random orientation. The exponent D_{fm} increases by 3.9 % from 1.675 to 1.740 as shown in Table 5-1.

5-2-2. Necking of particles

As indicated in Figure 5-1, the primary spheres making up the agglomerates are not distinct spheres touching at one point. There is a neck between the spheres. In some areas the agglomerate appears more like a rope than a chain of spheres. An extreme version of necking would be the formation of a cylinder. It is of interest to compare the dynamic shape factor and exponent D_{fm} for a chain and a cylinder. In this comparison the sphere diameter and cylinder unit length is taken to be 16.2 nm, and the cylinder diameter is chosen to give the same mass per length as the sphere. The friction coefficient for a cylinder with flat ends in the free molecular limit is given by:

$$f(cylinder) = \frac{\pi \mu d_{cy}^2}{2\lambda} \left\{ \left(\frac{L_{cy}}{d_{cy}} + \frac{1}{2} \right) f_r + \left(2 - \frac{6-\pi}{4} f_r \right) \left(\frac{L_{cy}}{d_{cy}} \sin^2 \theta + \cos^2 \theta \right) \right\}, \qquad (5\text{-}9)$$

where d_{cy} is the diameter of cylinder, L_{cy} the length of cylinder, f_r the fraction of molecules diffusely reflecting from the particle surface, and θ the angle between the polar axis of cylinder and flow direction. The relation between the primary sphere diameter, d_p, and the cylinder diameter, d_{cy}, is given by:

$$d_{cy} = (2/3)^{1/2} (d_p). \qquad (5\text{-}10)$$

The friction coefficient of a randomly oriented cylinder can be obtained from the friction coefficients computed about the three principle axes for the orientation dependent friction coefficient. These axes correspond to the cylinder oriented in the

direction of the field and the two axes orthogonal to the aligned direction. The resulting expression for the friction coefficient of a randomly oriented cylinder f_{random} (*cylinder*) is given by:

$$f_{random}(cylinder) = \frac{3}{\left[1/\ f(\theta = 0) + 2/\ f(\theta = \pi/2)\right]}\ . \qquad (5\text{-}11)$$

The two orthogonal axes have identical expression for the friction coefficient.

From Eqs. (5-9) and (5-11), one can compute f_{random} as a function of the length of the cylinder. The ratio of the dynamic shape factor for the cylinder to the dynamic shape factor for a chain of spheres with the same mass is shown in Figure 5-2. The cylinder has the same length and volume as the chain of spheres. The ratio is initially larger than 1.0 and then decreases asymptotically for large N or large mobility diameter to a value of about 0.86. The cylinder and the chain of spheres have nearly identical values of the friction coefficient for the orthogonal orientation; however, the friction coefficient in the aligned direction is about 30 % smaller for the cylinder compared to the chain.

It is seen in Eqs. (5-1) and (5-9) that the friction coefficient for both the chain of spheres and the cylinder become proportional to the number of spheres for large N so that it is not surprising that η is changed by less than 1 % for a chain versus a cylinder as indicated in Table 5-1. The mass-mobility diameter scaling exponent D_{fm} also is only slightly different for the cylinder compared to the chain.

5-2-3. Variability in primary sphere size

In comparing with experiment, the Chan and Dahneke expression for the friction coefficient, Eq. (5-1), was expressed in terms of N_m, which is the ratio of the mass of the agglomerate to the mass of a primary sphere. This estimation of N is correct if the primary spheres are monodisperse. In reality the estimated standard deviation of the primary spheres is about 20 % of the mean size. Below, the effect of the polydispersity was estimated on κ and D_{fm}.

For a distribution of primary sphere sizes, d_p^2 in Eq. (5-1) is replaced with the projected area diameter of the two touching spheres, $\left(d_{p1}^2 + d_{p2}^2\right)/2$. It is assumed that the value of c_{sp} and c_{bcu} are unchanged. The expression for f (*poly*) for a polydisperse distributions of primary spheres is computed as:

$$f\ (poly) = \mu \int_{d_{p1}} \Lambda \int_{d_{pN}} \left[c_{sp} d_{p1}^2 + c_{bcu}\left(d_{p1}^2 + d_{p2}^2\right) + \Lambda\ + c_{bcu}\left(d_{pN-1}^2 + d_{pN}^2\right) + c_{sp} d_{pN}^2\right]$$

$$P\left(d_{p1}\right)\Lambda\ P\left(d_{pN}\right) d_{p1} \Lambda\ d_{pN} / (8\lambda) \qquad , \tag{5-12}$$

where P is a normal distribution with mean $\bar{d}_p$, standard deviation σ, and N is the total number of primary spheres in the chain. Performing the integration by making use of the properties of a normal distribution, one obtains:

$$\begin{aligned} f\left(poly\right) &= \mu\left(\bar{d}_p\right)^2\left(1 + \sigma^2/\left(\bar{d}_p\right)^2\right)\left(c_{sp} + (N-1)c_{bcu}\right)/(4\lambda) \\ &\approx \mu N\left(\bar{d}_p\right)^2\left(1 + \sigma^2/\left(\bar{d}_p\right)^2\right)c_{bcu}/(4\lambda) \end{aligned} \quad . \tag{5-13}$$

The expression on the RHS, valid to an accuracy of about 2 % for $N > 12$, is used in the estimate.

The mobility diameter d_{mp} corresponding to the friction coefficient given in Eq. (5-13) is expressed implicitly by:

$$f(poly) = \frac{\mu N(\bar{d}_p)^2 c_{bcu}}{4\lambda}\left(1+\frac{\sigma^2}{(\bar{d}_p)^2}\right) = f(mono)\left(1+\frac{\sigma^2}{(\bar{d})^2}\right) = \frac{3\pi\mu d_{mp}}{C_c(d_{mp})}. \quad (5\text{-}14)$$

The value of d_{mp} is slightly different from $d_{m,}$ the mobility of the monodisperse chain of spheres, because of the term containing σ^2.

To compute κ for the polydisperse aerosol, the volume equivalent diameter for the polydisperse particles, d_{vep} is also needed. Using the properties of the normal distribution, the d_{vep} is obtained as:

$$d_{vep} = N^{1/3}\bar{d}_p\left(1+3\frac{\sigma^2}{(\bar{d}_p)^2}\right)^{1/3} = d_{ve}\left(1+3\frac{\sigma^2}{(\bar{d}_p)^2}\right)^{1/3}, \quad (5\text{-}15)$$

where d_{ve} is the volume equivalent diameter of the chain with N primary particles all with diameter $\bar{d}_p$. The expression for the friction coefficient of the volume equivalent diameter is then given by:

$$f(d_{vep}) = \frac{3\pi\mu d_{vep}}{C(d_{vep})}. \quad (5\text{-}16)$$

From Eqs. (5-14) and (5-16), one can compute the dynamic shape factor as a function of N, and also using the right hand side of Eq. (5-14), one can express the dynamic shape factor as a function of the mobility diameter. The ratio of the dynamic shape factor of the polydisperse distribution versus the monodisperse distribution is plotted in Fig. 2. It is seen that the ratio is mostly in the range 0.97 to 0.98.

As seen from Eq. (5-14), the friction coefficient for the polydisperse case is proportional to N so the exponent remains unchanged with a value of 1.0. The mass of the polydisperse chain can be expressed in terms of N using Eq. (5-15) and ultimately be computed as a function of implicitly expressed in terms of d_{mp} using Eq. (5-14). The

change in the exponent D_{fm} from the value for the monodisperse case is found to be 0.003.

The above estimate may break down for distributions with a large coefficient of variation ($\sigma / \bar{d}_p$). In the Chan and Dahneke analysis for monodisperse spheres, a gas molecule reflecting from one sphere can only collide with a neighboring sphere. As the polydispersity increases, the friction coefficient could be affected by reflected molecules from a large sphere hitting next nearest neighbors.

5-2-4. Dependence of Primary Sphere Size on Agglomerate Size

This analysis assumes that the primary sphere size is constant independent of the agglomerate size. This would be the case if the growth and shape of the primary spheres were fixed before the spheres began to form agglomerates. In reality, there may be some growth of primaries as well as sintering of primaries during the agglomeration. Here the case where the primary sphere size is assumed to have a power-law dependence on the number of primary spheres in the agglomerate was considered as:

$$d_p(N) = d_{p0} N^{\alpha} \ . \tag{5-17}$$

Substituting Eq. (5-17) into the large N approximation for Eq. (5-1) yields:

$$f = \frac{C_{bcu}\mu}{4\lambda} d_{p0}^2 N^{1+2\alpha} . \tag{5-18}$$

This is to be compared with the following expression for a constant primary sphere size, d_{pc}:

$$f_0 = \frac{C_{bcu}\mu}{4\lambda} d_{pc}^2 N . \tag{5-19}$$

From this analysis it is seen that the power law exponent η increases by an amount 2α for the size dependent d_p (N) relative to the constant d_{pc}.

There is a lack of experimental data on the size dependence of d_p. The measurement uncertainty of the primary sphere size is on the order of 10 % for a 16.2 nm sphere. Assuming there is a 10 % increase in the primary size as the number of primary spheres in an agglomerate increases from 36 to 152, from Eq. (5-17) α equal to 0.066 was obtained. This range in primary sphere sizes corresponds to the range in mobility diameter from 100 nm to 300 nm, which is the range studied by Shin *et al.* (2009a). In this case the exponent η increases by 0.132.

In assessing the effect of size dependence on the dynamic shape factor, it is convenient to compute f and f_0 for the same value of the mass. In this case, the ratio of the dynamic shape of the size dependent to constant primary sphere size, κ_v/κ_0, is equal to the ratio of the friction coefficients of the agglomerates. Equating the mass of the agglomerate with the size dependent primary sphere size to the one with the constant sphere size leads to the following relationship for the number of primary spheres:

$$N_0 = \frac{d_{p0}^3}{d_{pc}^3} N_v^{1+3\alpha}, \tag{5-20}$$

where N_0 is for constant primary size d_{pc} and N_v for size dependent primary size d_p (N) From Eqs. (5-18), (5-19), and (5-20), one obtains:

$$\frac{\kappa_v}{\kappa_0} = \frac{d_{pc}}{d_{p0}} N_v^{-\alpha}. \tag{5-21}$$

The value of d_{pc} is taken to be 16.2 nm and this value is set equal to $d_p(N)$ for N = 36. This is an arbitrary but convenient choice since it leads to $\kappa_v/\kappa_0 = 1$ for N = 36, which corresponds to a mobility diameter of 100 nm. In the study by Shin *et al.* (2008), the minimum mobility diameter was typically 100 nm. As N_v increases to 152, the ratio decreases by 10 %. This ratio can be computed as a function of the mobility diameter of the agglomerate for a constant primary sphere size using Eqs. (5-19) and (5-6). The results are shown in Figure 5-2.

For each value of N_v, one can compute the mass of the agglomerate by making use of Eq. (5-17). This together with the calculation of the mobility diameter enables one to compute the mass-mobility diameter scaling exponent D_{fm}. One finds for the size dependent primary sphere size, the fractal dimension is 0.109 larger than the baseline case.

There is another important experimental issue. The number of primary spheres in an agglomerate is the quantity N_0 rather than N_v. From Eqs. (5-18) and (5-20), one obtains the following expression for the dependence of f on N_0:

$$f = \frac{c_{bcu}\mu}{4\lambda} d_{p0}^2 \left(\frac{d_{pc}}{d_{p0}} \right)^{3\left(1-\frac{\alpha}{1+3\alpha}\right)} N_0^{\frac{1+2\alpha}{1+3\alpha}}. \qquad (5\text{-}22)$$

To assess the significance of this effect, the change in the exponent η observed by Shin *et al.* (2009a) is considered as the agglomerate size increased. The magnitude of the decrease was about 0.15. This change was attributed to a change in flow interaction with increasing agglomerate size. It is seen that the effect of a size dependent primary sphere size is in the same direction as the flow effect. Based on estimated α of 0.066, the decrease in η arising from the variable primary sphere size is 0.055, which is

significant relative to a decrease of 0.15. There is a large uncertainty in the estimated value of α and quantitative data are needed on the size dependence of the primary sphere size.

5-3. Discussion/summary

In summary, four non-ideal effects are estimated as perturbations to the Chan and Dahneke model. The change in the exponents D_{fm} and η arising from polydispersity and from necking are negligible with changes less than 1 %. Alignment in the electric field results in about a 4 % change in both exponents in the direction of the experimental results relative to the model prediction. The estimate is an upper bound estimate, since the perturbed case for the 300 nm mobility diameter is fully aligned. Partial alignment is more likely the case unless the agglomerate is more than a micrometer long.

The case of the variable primary sphere size is more dramatic but also more uncertain than the other perturbations. Assuming a 10 % increase in the primary sphere size as the mobility diameter of the chain increases from 100 nm to 300 nm, one estimates about a 10 % increase in both D_{fm} and η. In the case of η the direction of the deviation is the opposite of the experimental observation. These estimates are based on the number of primary spheres in the chain.

Experimentally the number of primary spheres is determined from the mass of the agglomerate assuming a constant primary sphere diameter. This leads to an over estimate by 13.2 % for η if there were a variable primary sphere size. This is a

significant effect relative to the observed 15 % decrease in η observed experimentally (Shin et al., 2009a) as the agglomerate size increases from the free molecular regime into the transition regime. This change in behavior is attributed to a flow interaction between the primary spheres.

While the magnitude of this effect and its relevance to understanding the flow effect are significant, the direct experimental evidence for a systematic variation of the primary sphere size with the size of the agglomerate for silver agglomerates does not exist. The estimated effect is based on the uncertainty in the measurement of the primary particle size and the uncertainty in the estimate is on the order of ± 100 % of the value.

While polydispersity has a negligible effect on the exponents, it has the dominant effect on the dynamic shape factor. It results in about a 14 % decrease in the dynamic shape factor for agglomerates with a mobility diameter approaching 300 nm. It is of interest to apply these corrections to the dynamic shape factor for the prediction of the model of Meakin *et al.*, since this model includes a more realistic fractal structure of the agglomerate and closer agreement with experimental results. It is seen in Figure 5-3 that the modified Meakin *et al.* results are in much better agreement with the measured results than the original predictions. The effect of the variable primary sphere size is not included because of the large uncertainty in this effect.

Effects	*Average* $\left\langle \frac{\kappa(after)}{\kappa(before)} \right\rangle$	D_{fm} (*before*)	Δ_D [a]	η	Δ_η [a]
alignment	0.977[b]	1.675 [b]	0.065 [b]	1.0	-0.043 [b]
polydispersity	0.975	1.554	0.003	1.0	0.000
necking	0.866	1.554	0.006	1.0	-0.0091
size dependent primary size	0.948	1.554	0.109	1.0	0.132

[a] $\Delta_D = D_{fm}(after) - D_{fm}(before)$ and $\Delta_\eta = \eta(after) - \eta(before)$

[b] For the size range d_m = 50 nm to 300 nm.

Table 5-1. Change in dynamic shape factor and the exponents D_{fm} and η for the mobility diameter of the baseline agglomerates in the range of 100 nm to 300 nm

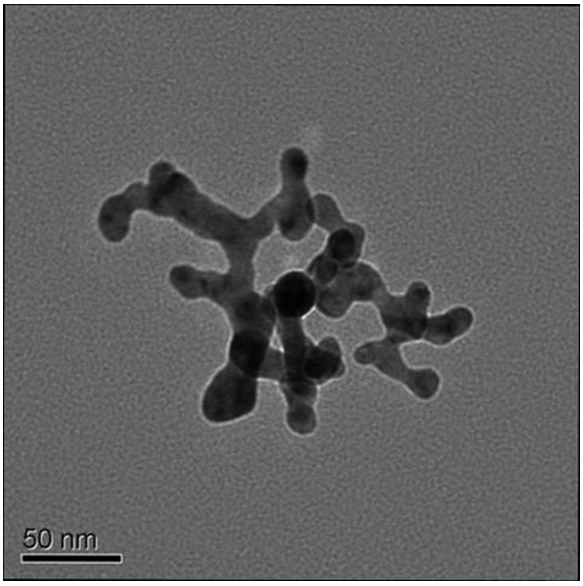

Figure 5-1. Representative TEM image of silver agglomerate particle

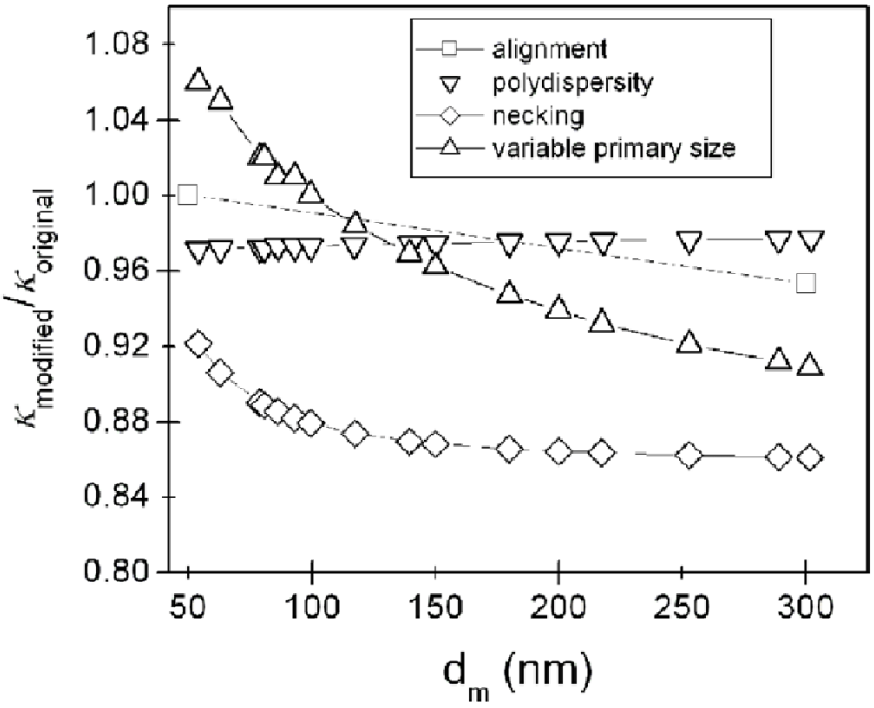

Figure 5-2. The ratio of predicted dynamic shape factor before and after modification considering non-ideality

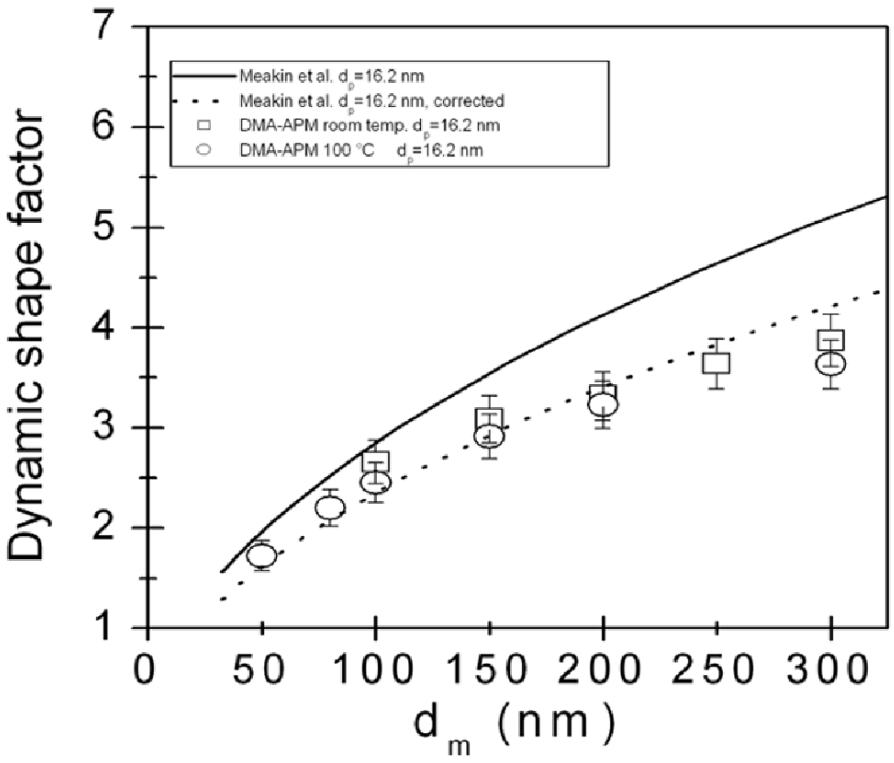

Figure 5-3. Dynamic shape factor as a function of d_m before and after adjustment of Meakin et al. considering non-ideality

Chapter 6 Determination of Volume, Mass-Mobility Diameter Scaling Exponent, and Particle Alignment of Nanoparticle Agglomerates Using Tandem Differential Mobility Analyzers

6-1. Introduction

Atmospheric and intentionally produced aerosol particles are often nonspherical. Soot particles are agglomerates that are almost always found in the ambient aerosol (Katrinak et al., 1993). Flame and furnace-generated particles such as TiO_2 and Ag particles with industrial applications also have agglomerate morphologies (Pratsinis, 1998; Ku and Maynard, 2006). The physical and chemical characterization of nonspherical and fractal agglomerate particles is an important area of current aerosol research (Friedlander and Pui, 2004).

There is a need for measuring the mass of agglomerate particles because particle mass is essential to describe aerosol behavior in ambient air and when aerosol particles enter into the human respiratory passage. Nonspherical particles have a larger friction coefficient compared to spherical particle with the same volume (Kousaka et al., 1996; Park et al., 2004a; Song et al., 2005; Zelenyuk and Imre, 2007). For nonspherical particles, effective density, i.e., mass/volume based on mobility diameter, is typically significantly lower than the inherent material density because the geometric volume of

nonspherical particle is smaller than that of spherical particle for the same mobility diameter (Kelly and McMurry, 1992; Hering and Stolzenberg, 1995; McMurry et al., 2002). The inherent material density (mass/volume) is also a fundamental property of aerosol particles that can be used to place bounds on composition of those particles. Independent measurements of mass and volume can be performed with gas pycnometry (Hanel, 1977). This approach requires several days to acquire a sufficient sample and typically provides no information on size dependent properties. Also, conventional offline filter based gravimetric methods such as those used in emission standard testing (Burtscher, 2005; Kittelson, 1998) require long sampling time. As online instruments, the Differential Mobility Analyzer (DMA) and the Aerosol Particle Mass analyzer (APM) have been used in tandem to measure the mass, effective density, or intrinsic density of agglomerate particles (Kelly and McMurry, 1992; Hering and Stolzenberg, 1995; McMurry et al., 2002; Park et al., 2004a; Park et al., 2004b; Lall et al., 2008; Kim et al., 2008; Shin et al., 2009a). Park et al. (2004a), Kim et al. (2008), and Shin et al. (2009a) provided structural properties of agglomerate in terms of mass mobility diameter scaling exponent and dynamic shape factor.

Physical properties of agglomerates can be estimated from mathematical models or be obtained from experiments. There are two difficulties in using free molecular based models for estimating the properties of agglomerates. Lall et al. (2008) tested the idealized aggregate (IA) theory (Lall and Friedlander, 2006) against volume measured by DMA-APM and showed a good agreement in the size range up to mobility diameter, d_m = 120 nm. However, Shin et al. (2009a) showed the breakdown of the free molecular models for the friction coefficient of agglomerates with more than 100 primary spheres

in the transition regime. The results indicate that estimates of physical properties of agglomerates such as dynamic shape factor, mass, and mass mobility diameter scaling exponent based on free molecular models can be inaccurate as agglomerate size becomes larger. Also, there are several characteristics of real agglomerates that are not incorporated in existing models for agglomerate dynamics (Shin et al., 2009b). These characteristics include particle alignment in the electric field, necking between particles, polydispersity of the primary particles, and variable primary sphere size.

In the previous studies (Ehara et al., 1996; McMurry et al., 2002; Shin et al., 2009a) showed that there is a calibration uncertainty of 5 to 7 % in the mass of NIST traceable particles measured with DMA-APM. Thus, it is of interest to use tandem Differential Mobility Analyzer (TDMA) method as another independent experimental method to study agglomerate dynamics and compare the results with those from DMA-APM method especially in terms of volume and mass mobility diameter scaling exponent of agglomerate particles. There is another advantage of using TDMA method. Because of limitation in maximum operating rotation speed of APM, it is very difficult to use DMA-APM for small nanoparticle agglomerates which weigh below 0.3 fg (Shin et al., 2009a). The smallest weight corresponds to silver agglomerates in the size range of d_m = 50 nm to 80 nm. However, TDMA method can be used for the small metal nanoparticle agglomerates. Thus it enables one to further investigate the dependence of the exponent η, which characterizes the dependence of the friction coefficient on the number of primary spheres. Shin et al. (2009a) found that the exponent η has a greater dependence on particle size than for mass mobility diameter scaling exponent D_{fm} from DMA-APM study.

Silver particles were chosen as tested particles in this study. One advantage of choosing agglomerates made composed of silver is that the agglomerates can be sintered at relatively lower temperature compared to other metal nanoparticles such as gold (Schmidt-Ott, 1988; Shimada et al., 1994; Weber and Friedlander, 1997). The sintering/coalescence processes have been investigated and explained by three stages in a number of previous studies (Weber and Friedlander, 1997; Friedlander and Wu, 1994; Ku and Maynard, 2006). The first stage is related to the re-arrangement and sintering of primary particles, leading to a sintered agglomerate of fewer and larger constituent particles (Weber and Friedlander, 1997; Schwade and Roth, 2003). The second stage is where the curvature between these particles defining necking disappears (Koch and Friedlander, 1990; Lehtinen et al., 1996) and the third stage is where the non-spherical particle coalesces into a sphere (Friedlander and Wu, 1994).

The sintering process has been used to characterize the dynamic and structural properties of agglomerate particles. Schmidt-Ott (1988) studied the change of mobility size of particles with initial mobility diameter, d_{mi} up to 100 nm during the sintering process using TDMA system. The sintering temperatures range over from room temperature to around 900 °C. In the study, the dynamic shape factor and fractal dimension of silver agglomerates, with a narrow range in mobility, were derived by measuring electrical mobility and aerosol photoemission (APE) during the sintering process. For the derivation, the volume equivalent diameter (d_{ve}) of an agglomerate particle was estimated from the measured mobility diameter (d_{cl}) of a close-packed agglomerate induced by the sintering process with a relationship:

$$d_{cl} = d_{ve} F_f^{-1/3}, \tag{6-1}$$

where F_f is a filling factor for a close-packed agglomerate (F_f = 0.7 used in the study). One disadvantage of Schmidt-Ott's approach is that the filling factor may vary according to the status of sintering or agglomerate size. Thus, the uncertainty for the filling factor can cause an inaccurate estimation of volume of agglomerate particle.

Ku and Maynard (2006) showed the agglomerate morphology changes from a loose structure to a compact structure as the sintering furnace temperature increases, using a Transmission Electron Microscope and a scanning mobility particle sizer (SMPS). In their experiments, polydisperse particles were sintered first and monodisperse particles classified after a sintering furnace. Thus, the mobility size change of monodisperse particles before and after the sintering process was not evaluated in the study.

In this study, mobility size change of monodisperse particles before and after the sintering process was also measured. The difference between this study and Schmidt-Ott's study is that the fully coalesced diameter of agglomerate particles was used in this study instead of the mobility diameter of close-packed agglomerates. The fully coalesced diameter of agglomerate particles is defined as the mobility diameter when the agglomerate particles become compact with a spherical shape. One expects the fully coalesced diameter to be very close to the volume equivalent diameter of the agglomerate particles. The fully coalesced diameter can be obtained by monitoring mobility size change with TDMA together with analyzing the TEM images.

In this study, the volume of agglomerate particles was determined using two independent methods: (1) TDMA with a sintering process (2) DMA-APM. The DMA-APM data are presented in the previous study (Shin et al., 2009a). Silver agglomerates

have a known bulk density of 10500 kg/m^3. Thus, one can determine the volume of silver agglomerates from the mass measured by DMA-APM. Silver agglomerate particles with a size range of 30 to 300 nm in mobility diameter are investigated in this study. However, for the d_m of 30 to 50 nm, mass data of silver agglomerates measured with DMA-APM is not available because of the limited operation range of APM.

Also, the mass mobility diameter scaling exponent of silver agglomerates determined by TDMA was compared with that obtained from DMA-APM data. The extent of particle alignment of large silver agglomerates was evaluated with TDMA. In addition, measurement results to determine whether particle evaporating or charging is occurring during the high temperature sintering were reported.

6-2. Theory

6-2-1. Theoretical basis of mobility measurement

The electrical mobility Z_p, of a singly charged particle can be determined by equating the electric field force and the Stokes drag force,

$$Z_p = \frac{eC_c}{3\pi\mu d}, \tag{6-2}$$

where e is the electron charge, C is the slip correction factor, μ is the viscosity of gas and d is particle diameter. Knutson and Whitby (1975) obtained the following

expressions for the mean electrical mobility of particles exiting a DMA and for the mobility bandwidth ΔZ_p:

$$Z_p^* = \frac{Q_{sh}}{2\pi \bar{V} \bar{L}} \ln\left(\frac{\bar{r}_2}{\bar{r}_1}\right), \tag{6-3a}$$

$$\Delta Z_p = \frac{Q_a}{Q_{sh}} Z_p^*, \tag{6-3b}$$

where Q_{sh}: sheath flow rate of DMA, Q_a: aerosol flow rate of DMA, $\bar{V}$: electrical voltage applied to DMA, $\bar{L}$: column length of DMA, $\bar{r}_2$: outer radius of annular space, and $\bar{r}_1$: inner radius of annular space.

6-2-2. IA theory (Lall and Friedlander, 2006)

Lall and Friedlander (2006) obtained a relationship between primary particle diameter (d_p) and mobility diameter using Chan and Dahneke (1981)'s expression for the friction coefficient of a chain agglomerate:

$$\frac{d_m}{C(d_m)} = \frac{c^* N \; d_p^2}{12\pi\lambda}, \tag{6-4}$$

where N is the number of primary spheres in the chain, d_p the diameter of the primary sphere, c^* is the dimensionless friction coefficient for a sphere, and λ is the mean free path of the gas. Lall et al. (2006) determined the size distribution, surface area distribution, and volume distribution of agglomerates based on electrical mobility measurements. In Eq. (6-4), if a primary particle size is known from TEM

measurements, N can be computed as a function of the mobility diameter d_m. Then, the volume, v, and volume equivalent diameter, d_{ve}, of agglomerate are given as:

$$v = N \frac{\pi d_p^3}{6}, \tag{6-5}$$

$$d_{ve} = N^{1/3} d_p. \tag{6-6}$$

6-3. Experimental

Silver nanoparticles are generated by the evaporation/condensation of silver powder (99.999%, Johnson Mattney Electronics) within the first electric tube furnace (Lindberg/Blue, Laboratory Tube Furnace STF55433C, max. temp 1500 °C). The primary particles collide and stick together in an agglomeration chamber leading to nanoparticle agglomerates made up of a few primary particles up to several hundred. In TDMA experiments, nanoparticle agglomerates were sintered in the second furnace (Lindberg/Blue, Laboratory Tube Furnace STF55433C, max. temp 1200 °C). Nitrogen was used as a carrier gas and the flowrate of carrier gas was 1.5 lpm. The reactor conditions are summarized in Table 6-1.

A thermocouple probe made of stainless steel (Model: KHXL-316G-RSC36, OMEGA, Inc) was used to measure temperature distribution inside the generation tube. The temperature uncertainty specified by the manufacturer is at most 2.8 °C for temperatures up to 1335 °C. The temperature distribution inside the generation tube is

shown in Figure 6-1. The measured gas temperature inside the generation tube was around 1169 °C at the center of the tube and was uniform over the central 40 cm region when the furnace temperature was set to 1150 °C. The temperature at the center of the sintering tube was also measured and it was found to be within a few percent of the set temperature.

A schematic diagram in Figure 6-2 shows the experimental set-ups to measure fully coalesced mobility diameter with TDMA system and to measure mass (or volume equivalent diameter) of silver nanoparticle agglomerates with DMA-APM system. When the TDMA system was used, the temperature of the second furnace was varied in the range of 200 °C to 900 °C. Transmission Electron Microscopy (TEM) was used to determine the primary particle size distribution as well as the change in particle morphology during the sintering process.

In the TDMA experiment, the coalesced diameters, d_{co}, of agglomerate particles in the size range of initial mobility diameter d_{mi} = 30 nm to 300 nm were obtained by monitoring mobility size change. For the dataset for d_{mi} = 30 nm to 100 nm silver agglomerate particles were generated without using an agglomeration chamber. Only charged particles with a narrow range of mobility passed through the two DMAs. The two DMAs were calibrated with NIST traceable reference particles (Mean size: 199 nm, Duke Scientific Corporation). The peak mobility size of the reference particles measured by the first DMA was 198.5 ± 1.04 nm. The uncertainty of the NIST traceable reference particles 1.7 % from manufacture specs. The peak mobility size of the same particles measured by the second DMA was outside the uncertainty range. The two parameters in Eq. (6-3a), i.e., $\overline{V}$ and Q_{sh} of the second DMA were checked and the error

in the mobility size measured by the second DMA was found to be mainly attributed to the inaccurate sheath flow rate of the second DMA. It is assumed that the values of the geometric constants of the two DMAs are identical within the manufacturing tolerances. Thus, the sheath flow rate of the second DMA was accordingly corrected to compensate for the difference between mobility sizes measured by the two DMAs. Then, particle mobility sizes originally obtained from the second DMA were corrected in the subsequent TDMA data analysis.

The estimated 1 sigma uncertainty in the mobility diameter was 1.7 %, which is equal to the square root of the sum of squares (RSS) of the uncertainty of the 199 nm spheres and repeatability uncertainty with a value of 0.2 %. In the TDMA experiments, monodisperse silver particles were classified by the first DMA and then enter the second furnace, which sintered the agglomerate particles. Then, a new mobility size, d_{m2}, caused by sintering process was monitored by manually scanning the size distribution around a roughly found peak size with a high size resolution of 2 to 4 nm at each temperature. From these measurements, the new mobility diameters of monodisperse agglomerate particles were determined as temperature was increased. Also, in order to assess the change in mobility size only due to sintering process, the possibility of coagulation of particles in the sintering tube was minimized by classifying the monodisperse particles before the second furnace. In most of TDMA experiments, a Po-210 neutralizer was not used in front of the second DMA. But, in one set of measurements, a Po-210 neutralizer was used to investigate the possibility of small particles being formed in the sintering furnace as the results of partial evaporation of

silver particles followed by nucleation and condensation. In order to investigate change in the morphology of particles, TEM analysis was used.

The present work also examines the extent of particle alignment with a TDMA system for d_m = 300 nm, which is the largest particle size in this study. Silver agglomerate particle with d_m = 300 nm was classified by the first DMA at Q_{sh} = 9.0 lpm. The mobility diameter distributions of singly charged silver agglomerate with d_m = 300 nm were obtained by manually scanning the second DMA at Q_{sh} of 9.0 lpm, 3.0 lpm, 1.5 lpm, and 1.0 lpm. By varying the sheath flow rate in the second DMA, the average electric field in the second DMA was changed. In the experiments, the Q_{sh} of 9.0 lpm corresponds to average electric field in DMA of 9 kV/cm and Q_{sh} of 1.0 lpm corresponds to 1 kV/cm.

Using DMA-APM, the masses of monodisperse agglomerates were determined as a function of the mobility diameter over a range from 80 to 300 nm (Shin et al., 2009a). Typical rotational speeds of APM used in this study were from 1400 rpm to 3250 rpm depending on mobility sizes from 80 to 300 nm. The volume equivalent diameter, d_{ve}, is calculated from particle mass measured by APM using Eq. (6-7)

$$d_{ve} = \left(\frac{6m}{\rho \pi} \right)^{1/3} \quad , \tag{6-7}$$

where ρ is the density of silver (1.05×10^4 kg/m^3).

6-4. Results and discussion

6-4-1. Mobility size change

Figure 6-3 shows mobility size distributions of sintered agglomerate particles with d_{mi} = 300 nm at various sintering temperatures. It is seen that the mobility diameter decreases by about a factor of two as the temperature is increased to 200°C and then approaches a value of about 140 nm at temperatures above 400 °C. The manually scanned size distributions were fitted by a Gaussian function to determine the peak mobility size.

In Figur 6-4(a), changes in the mobility size measured by the second DMA, d_{m2}, are plotted as a function of sintering temperature for d_{mi} = 30 nm, 80 nm, 150 nm, 250 nm, and 300 nm, respectively. Figure 6-4(b) shows that agglomerate particles with initial mobility sizes of 30 nm to 300 nm exhibit a sharp decrease in size by 20 % to 60 % of the initial sizes. In Figure 6-5, these mobility sizes (d_{m2}) were obtained without using a neutralizer in front of the second DMA. The larger agglomerates require higher thermal energy to become compact structures with a spherical form. As shown in Figure 6-5 (a), broad plateau regions (where the mobility size change is within few percent of initial mobility diameter) start from around 200 °C for d_{mi} = 30 nm, 300 °C for d_{mi} = 80 nm and 150 nm, and 400 °C for d_{mi} = 250 nm and 300 nm. Around those temperatures, primary particles of agglomerate re-arrange. This re-arrangement of weakly bonded primary particles is driven by the minimization of Gibbs free energy (Weber and Friedlander, 1997). Weber and Friedlander showed that at 300 °C the agglomerates with d_{mi} = 80 nm and 150 nm reached a close packed state and that there was no change in mobility diameter above 300 °C. For the cases of d_{mi} = 80 nm and 150 nm, the results are in a good agreement with Weber and Friedlander (1997)’s results. Ku and Maynard

(2006) found that particles (up to d_{mi} = 100 nm) classified by DMA located at downstream of the sintering furnace have spherical shapes at 600 °C.

Figure 6-4(b) shows normalized mobility size $d_{m2,\ normalized}$ vs. sintering temperature. The quantity $d_{m2,\ normalized}$ was obtained by normalizing the value of each d_{m2} with respect to the value of d_{m2} at 300 °C for d_{mi} = 30 nm and 80 nm and to that of d_{m2} at 400 °C for d_{mi} = 150 nm, 250 nm, and 300 nm. For d_{mi} = 300 nm, the mobility size decreased by 6 % as the temperature was changed from 400 °C to 800 °C while for d_{mi} = 150 nm, the change in the mobility size is less than 1 % for the temperature change from 400 °C to 700 °C.

TEM images of particles sintered at various temperatures were analyzed to better assess the degree of coalescence. Figure 6-5 shows representative TEM images of coalesced silver particles with d_{mi} = 80 nm, 150 nm, 250 nm, and 300 nm sintered at 600 °C. Most particles with d_{mi} = 250 nm and 300 nm look ellipsoidal while particles with d_{mi} = 80 nm and 150 nm look spherical. Figure 6-6 shows TEM images of sintered silver agglomerate particles with initial mobility diameter of d_{mi} = 300 nm. As the temperature of the sintering furnace is increased, the shape of particles becomes more spherical. One expects the mobility size to decrease as particle morphology changes from an ellipsoid to a sphere for a fixed mass. This is because a nonspherical particle has a larger mobility diameter compared to a spherical particle with the same volume (Kousaka et al., 1996; Park et al., 2004a; Song et al., 2005; Zelenyuk and Imre, 2007). At 800 °C the 300 nm particles are fully coalesced to a spherical form. As discussed below, this change in particle morphology is the likely cause of most if not all of the 4

nm decrease in size shown in Figure 6-6 as the temperature increases from 600 °C to 800 °C.

The possibility of partial sublimation of the silver particles was also considered. Schmidt-Ott (1988) showed that the peak mobility size of silver particles with initial mobility size d_{mi} smaller than 50 nm can drop down to zero at temperatures above 860 °C. In his study, the possibility of evaporation of agglomerate particles with mobility diameter larger than 50 nm was not investigated. In this study, particle evaporation was modeled with one dataset obtained from a slightly different experiment set-up: (1) generation furnace temperature was set at 1300 °C (2) sintering furnace temperature was varied up to 900 °C (3) A neutralizer was used in front of the second DMA. In the experiments, as temperature is increased from 800 °C to 900 °C the peak sizes of particles with d_{mi} = 300 nm and d_{mi} = 80 nm changed from 151.2 nm to 145.9 nm and from 61.5 nm to 53.3 nm, respectively.

The predicted particle size decrease was also computed based on the rate equation for particle evaporation (Hinds, 1981):

$$\frac{d(d)}{dt} = \phi \frac{8 D_v M}{R \rho_p d} \left(\frac{P_d}{T_d} - \frac{P_\infty}{T_\infty} \right), \tag{6-8a}$$

$$\phi_F = \frac{2\lambda + d}{d + 5.33(\lambda^2 / d) + 3.42\lambda}, \tag{6-8b}$$

$$\left[\frac{1}{2} d^2 + 1.42 \lambda d + 2.49 \lambda^2 \ln(d + 2\lambda) \right]_{d_1}^{d_2} = \frac{8 D_v M t}{R \rho} \left(\frac{P_d}{T_d} - \frac{P_\infty}{T_\infty} \right), \tag{6-8c}$$

where d is particle size, D_v is binary diffusion coefficient for the mixture of silver vapor and nitrogen, M is molecular mass of silver, R is gas constant, P_d is partial pressure of

vapor at the particle surface, T_d is particle temperature, P_∞ is partial pressure of vapor well away from the particle surface, T_∞ is ambient temperature, and ϕ_F is the Fuchs correction factor for $d < 1$ μm. In the calculations, it was assumed that $P_\infty = 0$ and $T_d = T_\infty$. The vapor pressure of silver is found to be 5.1 E-3 Pa and 0.094 Pa for 800 °C and 900 °C, respectively from Panish's study (1961). In the experimental setup, the residence times around the 40 cm center region (where the gas temperature is almost equal to furnace set temperature) are estimated to be 0.74 second and 0.64 second for 800 °C and 900 °C, respectively. At 900 °C the self diffusion coefficients of silver vapor and of nitrogen vapor are estimated to be 3.09 E-4 m^2/s and 2.38 E-4 m^2/s using Biolsi and Holland's (2007) and Cubley and Mason's (1975) results, respectively. The binary diffusion coefficients of silver vapor in nitrogen gas at 900 °C were estimated to be 4.97 E-5 m^2/s using simple kinetic theory.

As the temperature changes from 800 °C to 900 °C, the 151.2 nm and 61.5 nm particles are predicted to be decreased by 27.4 % and by 45.0 %, respectively during the residence time. These estimates are qualitatively similar to the observed change. However, the predicted decreases are larger than the observations. This may be because the particle temperature may be higher than the gas temperature or there is a significant vapor pressure of silver ($P_\infty > 0$).

It is of interest to estimate the decrease in particle size at 800 °C based on the model calculation with the residence time adjusted to give the observed decrease in particle size at 900 °C. For these conditions that for $d_{mi} = 300$ nm the predicted particle size change is from 156.8 nm to 156.5 nm at 800 °C. This indicates that the particle evaporation is negligible at 800 °C. Thus, the observed size change from 156.8 nm to

151.2 nm as the temperature changes from 600 °C to 800 °C is due to the change in particle morphology shown in Figure 6-6.

One curious observation from Figure 6-3 is that the absolute particle concentration decreased by about a factor of 16 as the temperature is increased from 600 °C to 800 °C. Shimada et al. (1993) showed that particle loss inside the heating tube by Brownian diffusion and thermophoresis is less than 20 % for 20 nm particle and less than 5 % for larger particle. The observed decrease is much larger than the expected thermophoretic loss.

To help resolve the cause of the large decrease, a second set of tandem DMA measurements were carried out with a neutralizer in front of the 2nd DMA. In this experiment, the temperature of generation furnace was set at 1300 °C. The resulting size distributions are plotted in the Figure 6-7 for the 1st DMA set to d_{mi} = 300 nm for sintering temperatures in the range 23 °C to 900 °C. One can see two peaks for sintered particles at around 150 nm for the temperatures of 600 °C and 800 °C. It is because the sintered particles turned into singly (+1) and doubly (+2) charged particles after passing through the second neutralizer. For the temperature change from 600 °C to 800 °C, the changes of the peak concentration for singly charged particle in Figure 6-7 are about 25 % while there is a 16 fold decrease in Figure 6-3. The values observed with the neutralizer are consistent with the combination of a drift in the aerosol generation rate and thermophoretic losses unlike the results without the neutralizer.

The change in particle concentration without a neutralizer shown in Figure 6-3 is most likely a result of an anomalous charging behavior, i.e., thermal recharging. Under high temperature conditions inside a tube furnace, negatively as well as positively

charged particles become multiply negatively charged (Magnusson et al., 1999). Thermal ionization can also cause the emission of positive ions from hot metal surfaces, such as iron, nickel or copper (Barnes, 1934). In TDMA experiments without a neutralizer in front of the second DMA, monodisperse particles with a positive charge after the first furnace were classified and passed through the sintering furnace. Then, the particles were classified with a single positive charge in the second DMA. During the sintering process, if positively charged particles become neutralized or negatively charged, the particle concentration measured by the second DMA will be decreased.

One surprising feature of Figure 6-7 is the high particle concentration in the small size range up to 60 nm as sintering temperature increases. Two possible causes of this effect are: (1) silver being deposited on the walls of the second furnace and reevaporated (2) ceramic material emitting particles at high temperature. If the walls inside the sintering tube are coated with silver and the vapor pressure corresponding to the sintering furnace temperature is known, one can estimate the maximum volume concentration of silver converted to aerosol form. Volume concentrations of silver vapor at room temperature for sintering furnace temperatures of 800 °C and 900 °C are found to be 2.16 E10 nm^3/cm^3 and 3.97 E11 nm^3/cm^3. Estimated volume concentrations of silver are two orders of magnitude larger than the observed volume concentrations. In separate experiments, small particles were found to be emitted from the inner surface of a ceramic tube without silver powder present at temperature around 900 °C. Thus, small particles were more likely to be emitted from the inner surface of a ceramic tube, rather than formed by evaporation of silver deposited on the walls.

6-4-2. Comparison of coalesced diameter (d_{co}) with volume equivalent diameter (d_{ve})

The coalesced diameter obtained from TDMA experiment was compared with the volume equivalent diameter from DMA-APM measurement. There are two available datasets for both TDMA and DMA-APM experiments for the same range of mobility size. Both experiments were performed on the same days with the identical particle generation and particle classification conditions. The coalesced diameter of an agglomerate is considered as the mobility diameter (d_{m2}) of the agglomerate measured by the second DMA. TEM image analysis results showed that the agglomerates are fully coalesced at 400 °C for d_{mi} below 100 nm, at 600 °C for d_{mi} = 150 nm, and at 800 °C for d_{mi} = 250 nm, 300 nm. However, for d_{mi} = 250 nm and 300 nm mobility sizes were obtained only at 600 °C on the same day as DMA-APM data. For this set of tests, TDMA data were not collected at 800 °C. In the following analysis (Figures 6-8, 6-9), the results were corrected considering a further decrease in the mobility size at 800 °C. The fully coalesced diameters of particles with d_{mi} = 250 nm, 300 nm were obtained by decreasing the diameters obtained at 600 °C by 3 %.

Figure 6-8 shows the relationship between coalesced diameter (d_{co}) measured from TDMA and volume equivalent diameter (d_{ve}) determined by DMA-APM. The DMA-APM dataset used in this study includes 01/04/08[e], 01/05/08[f], 01/11/08[h], and 01/12/08[i] in the Table 3 of Shin et al. (2009a)'s study when TDMA experiments were conducted on the same days as DMA-APM experiments. The results show that the ratio between the two diameters is in the range 1.00 to 1.08. For d_{mi} = 80 nm and 150 nm, the ratio is very close to 1.0 while for d_{mi} = 250 nm and 300 nm, the ratio exceeds 1.0 by 2 % to 8 % because at 600 °C the shape of the compact particles is not spherical but

ellipsoidal as shown in the Figures 6-5 and 6-6. After the corrections for the fully coalesced diameters for d_{mi} = 250 nm, 300 nm, the ratio is below 1.05.

In TDMA experiments, the uncertainty in the mobility diameter (d_{m2}) of fully coalesced particles measured by the second DMA is dependent on the uncertainty of mobility diameter in the 1st DMA, i.e., 1.7 % because the 2nd DMA is calibrated against the 1st DMA with NIST traceable PSL particles. For the DMA-APM, there are a number of factors that contribute to the uncertainty in the mass measurement. These include measurement repeatability, the calibration uncertainty, and the uncertainty in obtaining the size distribution from inverting the convolution integral. In the previous study (Shin et al., 2009a), the relative combined mass uncertainty is estimated as 6.8 %. So, the relative combined uncertainty in volume equivalent diameter is estimated to be 2.2 %.

6-4-3. Comparison of mass-mobility diameter scaling exponents from TDMA and DMA-APM

Mass-mobility diameter scaling exponent, $D_{fm,}$ characterizes the power law dependence of the mass on the mobility diameter as follows (Park et al., 2004a):

$$m = k_m \, d_m^{D_{fm}}, \tag{6-9}$$

where k_m is a prefactor. The mass data for TDMA were originally converted from coalesced diameters determined by TDMA with a relationship ($m = \rho \, \pi/6 \, d_{co}^{3}$). The average value of D_{fm} measured by TDMA is slightly larger than that measured by DMA-APM method. Corrections were made for fully coalesced diameters of d_{mi} = 250 nm and 300 nm based on the observation that d_{m2} for d_{mi} = 250 nm and 300 nm can be

further reduced by 3 %, as morphology changes from an ellipsoid at 600 °C to a sphere at 800 °C.

In Figure 6-9, masses of agglomerates obtained from both DMA-APM and TDMA experiments are plotted as a function of mobility diameter. The DMA-APM dataset includes 01/04/08[e], 01/05/08[f], 01/11/08[h], and 01/12/08[i] data shown in Table 3 of Shin et al. (2009a)'s study when TDMA experiments were conducted on the same days as DMA-APM experiments. The best fit values of D_{fm} were obtained for each dataset and the best fit curves for each dataset were also plotted in Figure 6-9. For the size range of d_m = 80 nm to 300 nm the best fit value of D_{fm} is found to be 2.126 from the DMA-APM dataset and 2.172 from TDMA dataset after corrections for the fully coalesced diameters of d_{mi} = 250 nm, 300 nm, respectively. Before the corrections, the best fit value of D_{fm} is found to be 2.256 from TDMA dataset.

Following the approach to calculate the uncertainty in D_{fm} (Shin et al., 2009a), DMA-APM method, we obtained the overall measurement uncertainty in D_{fm}, $u_{tot}(D_{fm})$, of 0.028 for datasets including 01/04/08[e], 01/05/08[f], 01/11/08[h], and 01/12/08[i] data shown in Table 3, of Shin et al. (2009)'s study. It corresponds to $D_{fm} = 2.126 \pm 0.061$. In this paper, we only describe the uncertainty analysis for TDMA method briefly.

For TDMA method, the measurement uncertainty in D_{fm} arises from fitting the data to a power law expression, from the propagation of the uncertainties from mobility diameter. The relative uncertainty, $\sigma_A(D_{fm})$, obtained from a linear least square analysis of the variables $\ln(m)$ and $\ln(d_m)$ is 0.0134. The estimated uncertainty in d_m given above was 1.7 % of the value. A constant percentage change in d_m will not affect the slope for a log-log plot for the mass and mobility diameter. However, a more careful analysis

indicates that the likely error in measuring d_m depends slightly on particle size. A likely source of the error in the d_m measurement is an error in the flow measurement. A constant error in the flow measurement will result in a constant error in the mobility, but not quite a constant change in d_m. For example, a flow decrease of 5 % in the DMA will result in 5 % decrease in the electrical mobility and a 3.8 % increase in d_m for d_m equal to 300 nm, but this same change in flow will result in a 3 % increase in d_m for d_m equal to 80 nm. The best fit value for D_{fm} decreases fractionally by 0.002 based on the modified mobility diameters. This value is identified as the relative uncertainty component, $u_F(D_{fm})$. One needs to consider the relative correction uncertainty, $u_C(D_{fm})$ caused by making corrections for the fully coalesced diameter of d_m = 250 nm, 300 nm. The mobility size change of 3 % for the temperature change from 600 °C to 800 °C has a uncertainty level of ± 0.5 %. This value is identified as the relative uncertainty component, $u_C(D_{fm})$. For TDMA method, the total relative uncertainty which is equal to the square root of the sum of squares (RSS) of $\sigma_A(D_{fm})$, $u_F(D_{fm})$, and $u_C(D_{fm})$ is 0.019 and corresponds to D_{fm} = 2.172 ± 0.031.

The value of D_{fm}, 2.172 ± 0.031, measured with TDMA in this study agrees relatively well with the value of D_{fm}, 2.126 ± 0.061, measured with DMA-APM (Shin et al., 2009a). But, the uncertainty range for TDMA is slightly outside the value by DMA-APM. In detail, the total relative uncertainty in D_{fm} measured with TDMA is smaller by 1.4 % than that with DMA-APM.

The measurement size range was extended down to 30 nm in order to check the dependence of D_{fm} on the mobility diameter as shown in Figure 6-9. First, it is of interest to compare our measured value of D_{fm} of 2.123 ± 0.012 by TDMA for the size

range of 30 nm to 100 nm with the previous results by Schmidt-Ott (1988) with TDMA and by Shin et al. (2009a) with DMA-APM. The value of D_{fm} was found to be 2.18 by Schmidt-Ott for the size range of 25 nm to 90 nm. It is outside our 1 sigma limit. However, there is a larger difference between the two measured values (2.123 and 2.18) and the measured value of D_{fm} of 2.074 by Shin et al. (2009a) for the size range of 50 nm to 100 nm (see 50 -100 nm data in Table 3 of Shin et al. (2009a)). It can be attributed to a systematic effect observed for the dataset for 50 -100 nm (see Fig. 7 of Shin et al. (2009a)).

Shin et al. (2009a) found that there is a little dependence of D_{fm} on the mobility size of particles. In the study, D_{fm} changed from 2.055 to 2.074 as the size range changes from 100 – 300 nm to 50 -100 nm. In Figure 6-9, the measured value of D_{fm} with TDMA is 2.123 for the size range of 30 nm to 100 nm and 2.172 for the size range of 80 nm to 300 nm. Thus, the TDMA measurement results confirm Shin et al. (2009a)'s conclusion. Wang and Sorensen (1994) previously reported a similar finding about the constancy of D_{fm} based on three datasets. They found a value of about 0.45 for the exponent χ characterizing the power law dependence of the mobility radius on the number of primary particles. The exponent χ equals $1/D_{fm}$ so that the corresponding value of D_{fm} is 2.22. The total variation in the exponent D_{fm} was about 6 % across the flow regime from free molecular to near continuum.

In Figure 6-9, there is about 30 % difference in terms of mass of particles in the range of d_m = 80 nm to 100 nm between TDMA dataset for d_m = 30 nm to 100 nm and TDMA dataset for d_m = 80 nm to 300 nm. It can be attributed to slight differences between those experimental setups. The two sets of experiments were carried out on

different days. Also, for the dataset for d_m = 30 nm to 100 nm silver agglomerate particles were generated without using an agglomeration chamber. One can expect that primary particle size may grow inside an agglomeration chamber. Shin et al. (2009a) showed that the mass is roughly proportional to primary particle size. However, information about the primary particle size distribution is not available for the dataset for d_m = 30 nm to 100 nm.

6-4-4. Particle alignment

When Eq. (6-4) is used to determine the number of primary particles with a known d_p corresponding to the mobility size of agglomerates, the selection of c^* significantly affects the prediction results of volume. Previous studies assumed that the agglomerates in the size range up to around d_m = 150 nm orient parallel to the electric field due to dipole formation (Lall et al., 2006; Stober et al., 1974, Lall et al., 2008) and thus 6.62 was used as a dimension less drag c^* in Eq. (6-4) rather than 9.17. However, the alignment of realistic agglomerate particle with branches and kinks in electric field has not been investigated.

In this study, the extent of particle alignment for d_m = 300 nm, which is the largest particle size in this study, was investigated. Figure 6-10 indicates that the alignment of 300 nm silver agglomerate particle changes from the partial alignment at the higher electric field E = 9 kV/cm corresponding to Q_{sh} = 9.0 lpm towards a random orientation at lower electric field E = 1 kV/cm. For the electric field lower than E = 1 kV/cm, the agglomerate particles may be more randomly oriented. The results show the mobility size change of 7 % for the corresponding change of sheath flow rate of the

second DMA. Kim et al. (2007) indicate that a factor of 7 increase in the orientational electrical energy for nanowires results in a change from a nearly random orientation to a more aligned orientation with a peak in the angular distribution at about 12°. The factor of 9 change in electrical field would result in a 9 fold change in the energy for the free charge plus a potentially larger contribution from the polarizability of the agglomerate. So it is reasonable that this 9 fold change in voltage includes the nearly random motion to the nearly aligned alignment.

It is of interest to compare the experimental data with the cross model described in the recent study on the estimates of non-ideal effects on the friction coefficient of silver agglomerates (Shin et al., 2009c). The model was designed to estimate the orientation effect. One can compare the mobility diameter for the case of 220 primary spheres (136 in the long direction and 85 in the short direction with one sphere shared) for the aligned orientation and random orientation. The ratio of the friction coefficient for the random orientation to that for the aligned orientation is about 1.09. The ratio of the corresponding mobility diameters is about 1.06. The estimated mobility size change is very close to the observed mobility size change of 7 % for the factor of 9 change in electrical field in Figure 6-10.

It is of interest to check how the observed mobility size change of 7 % would affect the value of D_{fm} determined via both methods. In both cases, the DMA is used to measure the mobility diameter. For both methods, when the agglomerates are not aligned, the mobility size would be equal to 321 nm rather than to 300 nm. For the TDMA datasets, coalesced diameters for d_m = 250 nm, 300 nm were corrected. For the Jan. 12th datasets, D_{fm} decreases by 3.4 % from 2.139 for the aligned orientation versus

a random orientation for DMA-APM method. For the TDMA method, D_{fm} decreases by 2.0 % from 2.104 for the aligned orientation versus a random orientation. Shin et al. (2009c) estimated how this change in orientation would affect the D_{fm} and found that the exponent D_{fm} decreases by 3.9 % from 1.740 to 1.675.

6-4-5. Modeling for the friction coefficient of non-spherical particles

In section 6-4-1, it is seen that the morphology change shown in Figure 6-6 induced by the sintering temperature change from 600 °C to 800 °C is a likely cause for the change of 3 % for mobility size, i.e., the change of 5 % for the friction coefficient. One can approximate the non-spherical particle shown in Figure 6-6(b) as an ellipsoid. It is of interest to estimate the friction coefficient in the free molecular limit for an ellipsoid and for a sphere with the same volume as the ellipsoid.

For the free molecular regime, there is an exact solution for the friction coefficient of a prolate spheroid in the free molecular regime given by Dahneke (1973) as:

$$f_{spheroid,\,free\,mol.} = \frac{\pi \mu a^2 \beta}{\lambda}\left[\begin{array}{l}\sin^2\theta\left(A_p\left\{4+\left(\frac{\pi}{2}-1\right)f_m\right\}+\frac{C_p}{B_p^2}\left\{2+\frac{4B_p^2+\pi-6}{4}f_m\right\}\right)+\\ \cos^2\theta\left(2A_p\,f_m+\frac{C_p}{B_p^2}\left\{B_p^2(4-2\,f_m)-4+\left(3-\frac{\pi}{2}\frac{1}{\beta^2}\right)f_m\right\}\right)\end{array}\right], \tag{6-10}$$

where

$$A_p = \frac{\sin^{-1} B_p}{B_p},$$

$$B_p = \left\{1 - \frac{1}{\beta^2}\right\}^{1/2},$$

$$C_p = \frac{1}{\beta} - A_p,$$

and f_m is the momentum accommodation coefficient (= 0.9) and θ is the angle between the major axis of particle and the flow direction.

For a sphere in the free molecule regime, the friction coefficient is given by Dahneke (1973) as:

$$f_{sphere} = \frac{\pi}{6}\left(8 + \pi\, f_m\right)\frac{\mu\, d}{Kn}. \qquad (6\text{-}11)$$

The averaged values of aspect ratio, β, of the non-spherical particles at 600 °C shown in Figures 6-5 and 6-6 are found to be 1.38 ± 0.30 for d_{mi} = 250 nm and 1.56 ± 0.38 for d_{mi} = 300 nm, respectively from the TEM image analysis of 50 particles for each initial mobility size. It is assumed that an ellipsoid has the same volume as sphere with d = 139 nm. Thus, the sphere equivalent average radius of an ellipsoid with the aspect ratio of 1.56 for d_{mi} = 300 nm is equal to 60 nm. Kim et al. (2007) also assumed that the ellipsoid is more likely to be randomly oriented because the aspect ratio is small. The estimated friction coefficients of an ellipsoid with a random orientation and a sphere in the free molecule regime are 1.50E-11 kg/s and 1.45E-11 kg/s, respectively. The estimated ratio of the friction coefficients between an approximated spheroid and a sphere is 1.034. This value is less than the observed ratio of 1.05. The difference could be from the measurement uncertainty or uncertainty in the approximation of the sintered particles as an ellipsoid.

6-5. Conclusions

The agglomerate volume and mass-mobility diameter scaling exponent were determined using TDMA method together with TEM image analysis for the mobility size of 30 nm to 300 nm. For the flow conditions used in this study, TEM image analysis results indicate that the large agglomerates with d_m = 250 nm and 300 nm require a temperature of 800 °C to form a spherical shape compared to 600 °C for a mobility diameter of 150 nm.

For the mobility size of 80 nm to 300 nm, the value of D_{fm} of 2.172 measured with TDMA in this study agrees with the value of D_{fm} of 2.126 measured with DMA-APM (Shin et al., 2009a). But, the uncertainty range for TDMA barely overlaps the value by DMA-APM. The total relative uncertainty in D_{fm} measured with TDMA is 1.9 % and that measured with DMA-APM is 3.1 %.

TDMA method is more useful than other methods in order to investigate the mechanics of metal agglomerate particles in the small size range below 100 nm together with sintering process. For the small size range, the measured D_{fm} of 2.123 for the size range of 30 nm to 100 nm agrees with Schmidt-Ott's results (the value of D_{fm} is 2.18 for the range of d_m = 25 nm to 90 nm). The Schmidt-Ott's value of D_{fm} is outside the 1 sigma limit in this study.

Two TDMA datasets were used to check the dependence of D_{fm} on mobility diameter. The measured value of D_{fm} is 2.123 for TDMA dataset in the size range of 30 nm to 100 nm and 2.172 for TDMA dataset with the size range of 80 nm to 300 nm.

Thus, the TDMA measurement results confirm Shin et al. (2009a)'s conclusion, i.e., little dependence of D_{fm} on the mobility size of particles (the value of D_{fm} changes about 1 % for the similar change in the size range). The observation from this study is also consistent with Wang and Sorensen (1994)'s finding about the constancy of D_{fm} (the total variation in the exponent D_{fm} was about 6 % across the flow regime from free molecular to near continuum).

Estimates about particle evaporation indicate that sublimation for agglomerates with d_{mi} = 300 nm is negligible (less than 1 % change in the particle diameter) at 800 °C compared to at 900 °C (predicted to be 27 % decrease in particle diameter). Thus, the observed mobility size change as temperature increases from 600 °C to 800 °C is due to a change in particle morphology. However, the observed mobility size change as temperature changes from 800 °C to 900 °C was caused by partial evaporation of particles.

Experimental results indicate that silver agglomerate particle with d_m = 300 nm can be partially aligned in an electric field inside DMA and the observation is in a good agreement with an estimate with a cross chain of spherical particles (Shin, 2009c). The alignment results in a decrease of 7 % in the mobility diameter and a decrease of 2 % in D_{fm}.

A factor of ten decrease in the peak particle concentration with increasing sintering temperature was observed at the exit of a second DMA positioned after the sintering furnace. There was no bipolar charger placed before the 2nd DMA. The large decrease is likely a result of thermal recharging of charged particles in the sintering tube

at high temperatures. This observation agrees well with Magnusson et al. (1999)'s results.

Type	Dimensions	Residence time[a], s	Temperature, °C
Generation tube (1st furnace)	Length : 89 cm I.D. : 1.43 cm	5.7	1150
Agglomeration chamber	Volume: 6.7 L	270	25
Sintering tube (2nd furnace)	Length : 89 cm I.D. : 1.43 cm	5.7	25 to 900

[a] Residence time computed based on a flow of 1.5 L/min at 25 °C and the reactor at 25 °C.

Table 6-1. Experimental condition of aerosol reactor

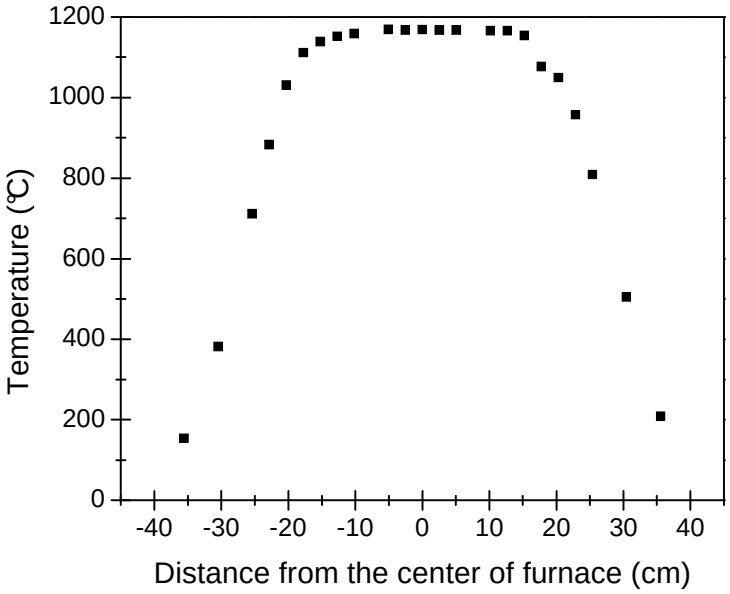

Figure 6-1. Distribution of gas temperature inside a generation tube when the first tube furnace temperature was set to 1150 °C

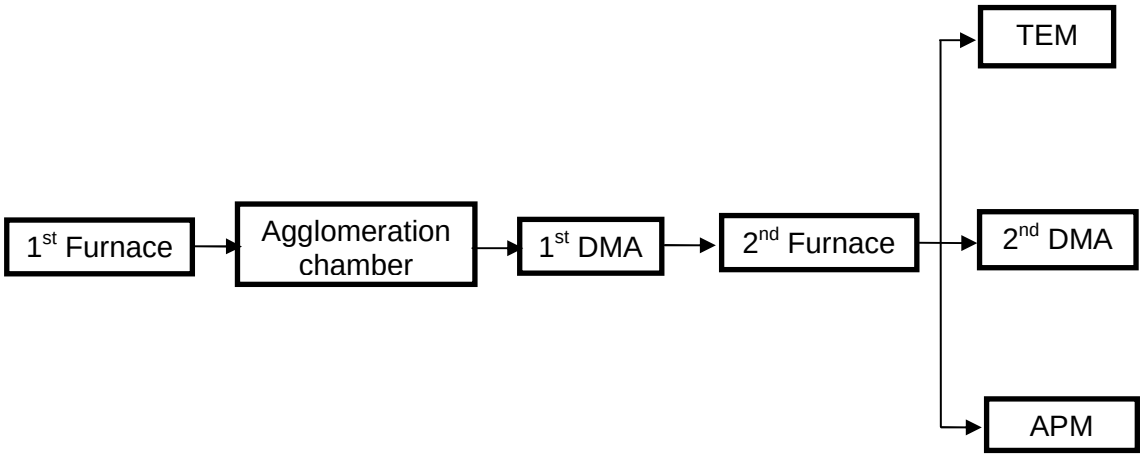

Figure 6-2. Schematic diagram of experimental set-up to measure fully coalesced mobility diameter and particle alignment using TDMA and of volume equivalent diameter using DMA-APM

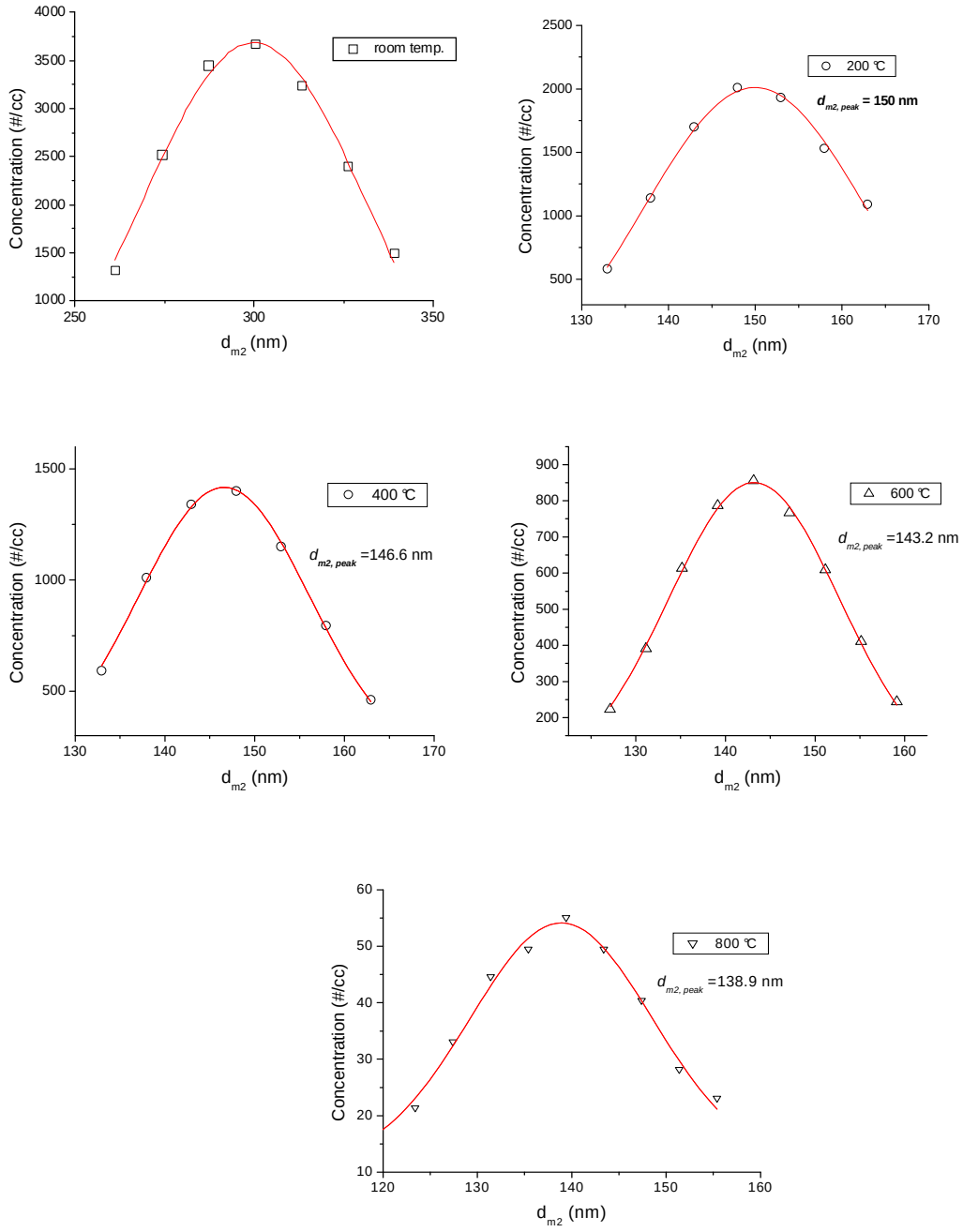

Figure 6-3. Mobility size change after sintering agglomerates with initial mobility size (d_{mi}) = 300 nm at various sintering temperatures (Results were obtained without using a neutralizer in front of the second DMA and each legend indicates a peak mobility size)

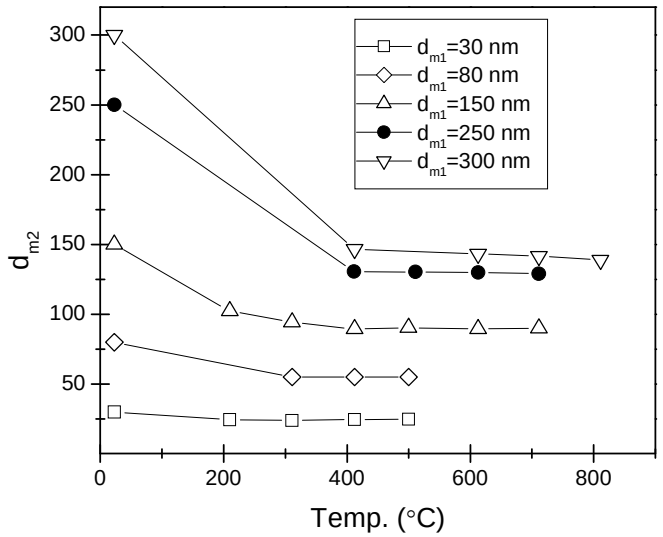

(a)

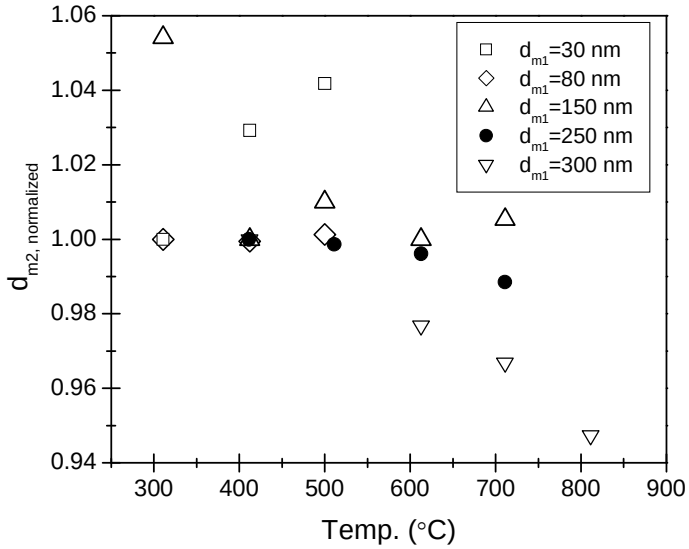

(b)

Figure 6-4. (a) Change in mobility size (d_{m2}) and (b) normalized mobility size vs. sintering temperature for d_{mi} = 30 nm, 80 nm, 150 nm, and 300 nm (Results were obtained without using a neutralizer in front of the second DMA when the temperature of generation furnace was 1150 °C)

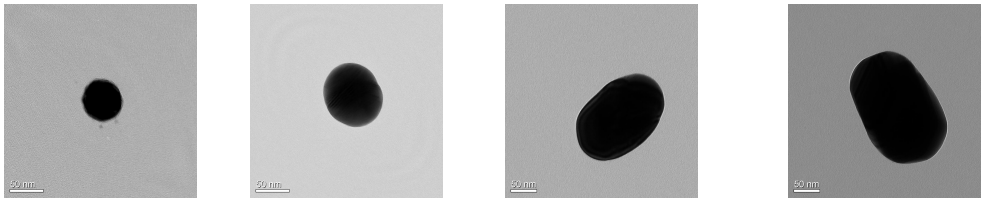

Figure 6-5. Representative TEM images of coalesced silver particles at 600 °C: (a) d_{mi} = 80 nm (b) d_{mi} = 150 nm (c) d_{mi} = 250 nm (d) d_{mi} = 300 nm

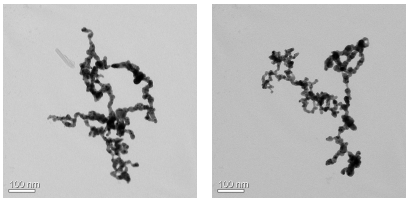

(a)

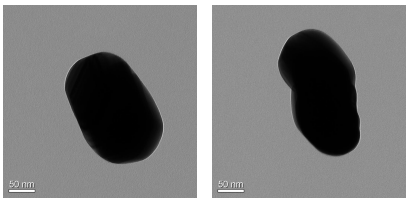

(b)

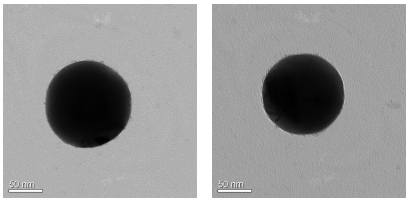

(c)

Figure 6-6. Representative TEM images of silver agglomerate particles with d_{mi} = 300 nm at various sintering furnace temperatures: (a) 20 °C (b) 600 °C (c) 800 °C

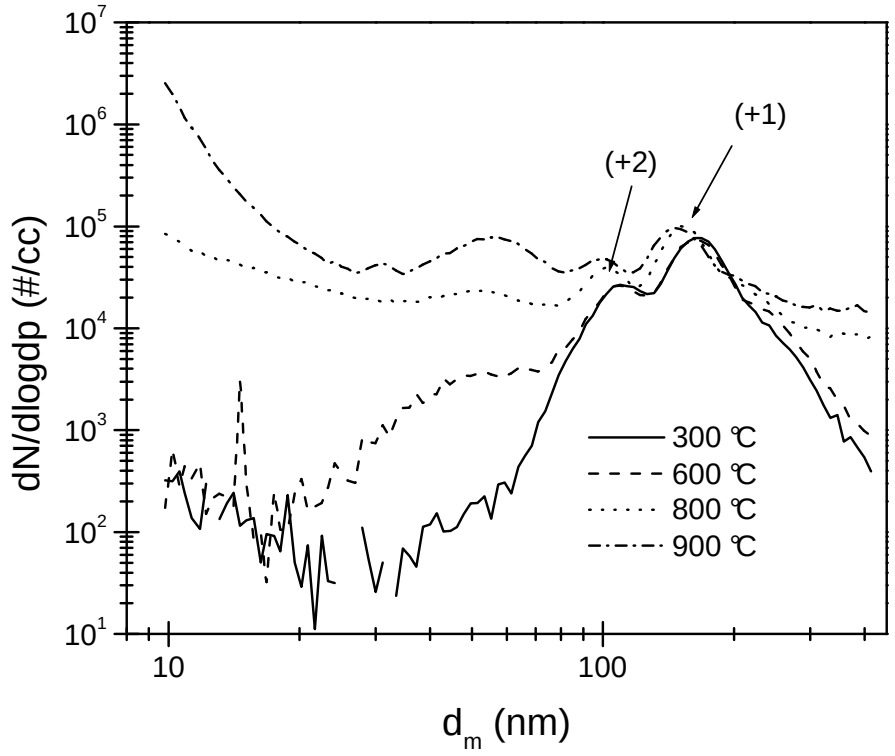

Figure 6-7. Scanned particle size distribution of agglomerates with d_{mi} = 300 nm at various sintering temperatures (Results were obtained using a neutralizer in front of the second DMA when the temperature of generation furnace was 1300 °C)

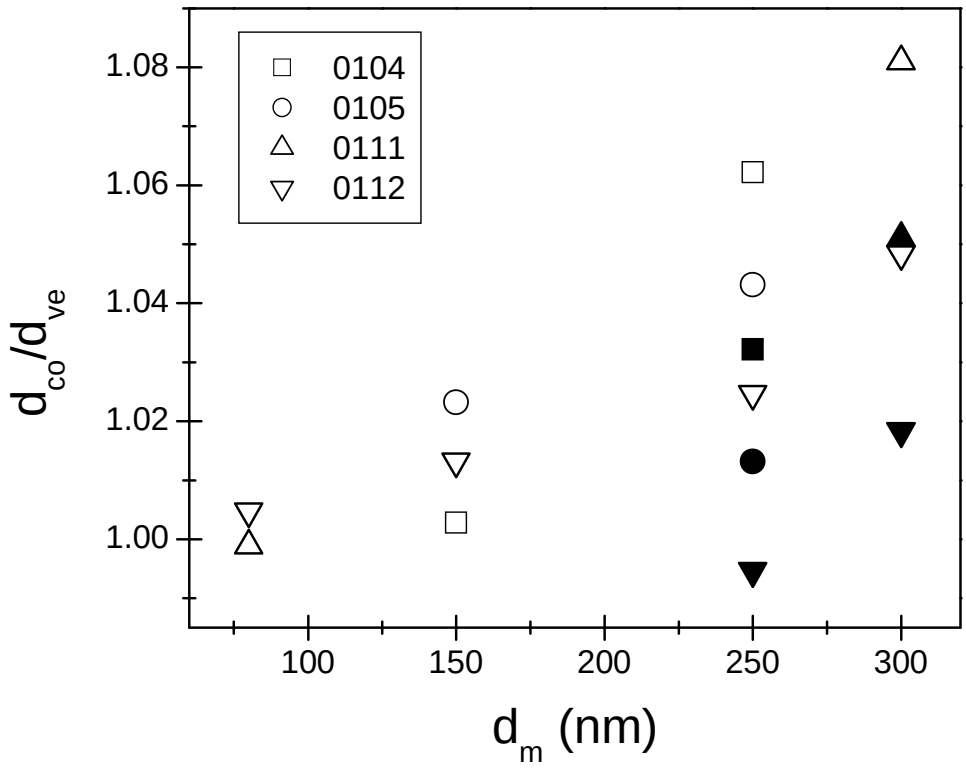

Figure 6-8. The relation between coalesced diameter (d_{co}) and volume equivalent diameter (d_{ve}) of silver agglomerate: solid symbols represent fully coalesced diameters made after corrections for d_{mi} = 250 nm, 300 nm.

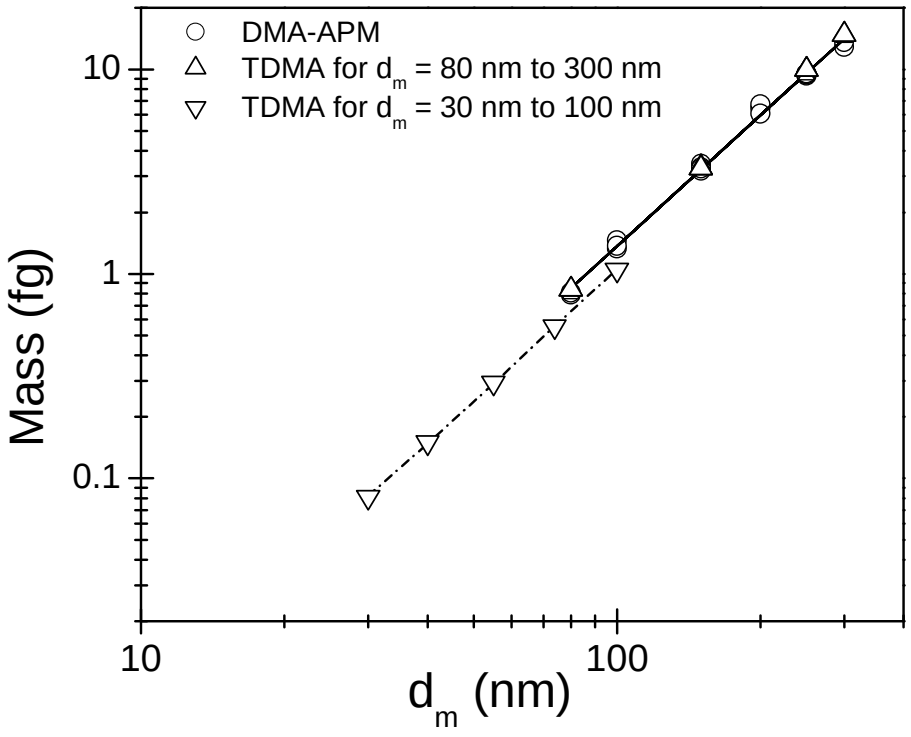

Figure 6-9. Dependence of mass on mobility diameter: For TDMA dataset and DMA-APM dataset for d_m = 80 to 300 nm it is shown that data sit on the top of each other. For the dataset of TDMA for d_m = 80 nm to 300 nm correction was made for fully coalesced diameters for d_{mi} = 250 nm, 300 nm. The slope (D_{fm}) is 2.172 by TDMA for d_m = 80 nm to 300 nm, 2.123 by TDMA for d_m = 30 nm to 100 nm and 2.126 by DMA-APM for d_m = 80 nm to 300 nm.

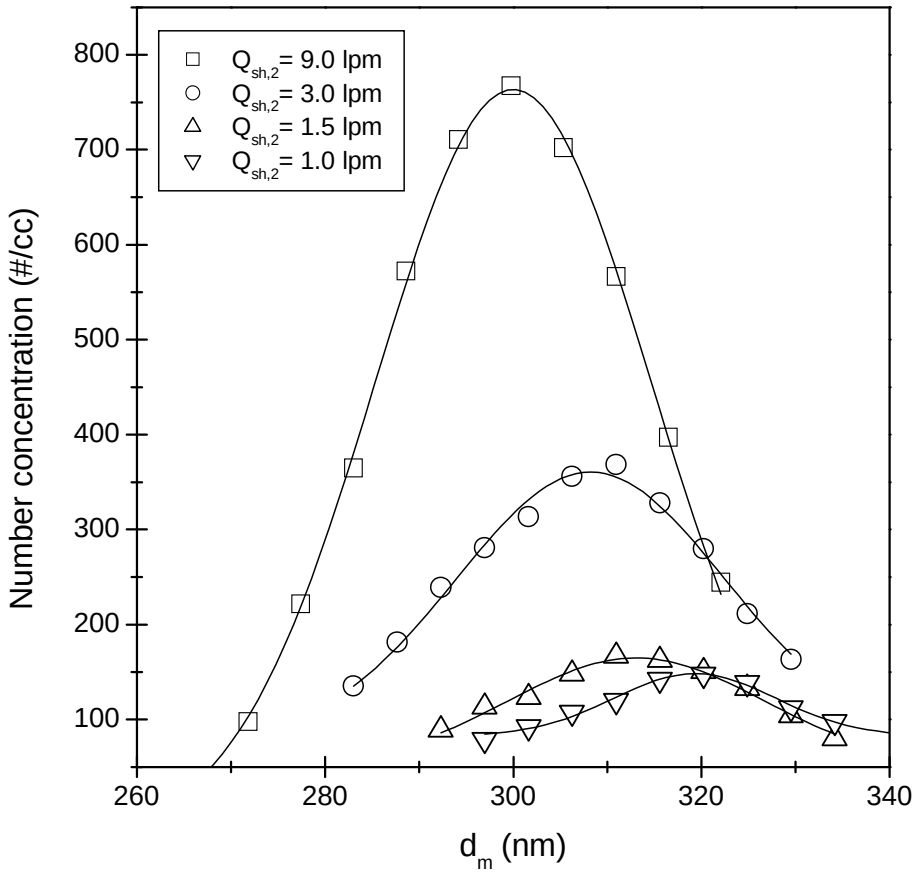

Figure 6-10. The effect of particle alignment on the mobility size of agglomerates with d_{mi} = 300 nm

Chapter 7 The Effect of Dielectric Constant on Unipolar Diffusion Charging of Nanoparticles

7-1. Introduction

Diffusion charging has been widely used in many applications of aerosol science and technology, such as sizing particles in aerosol size spectrometers (Shah and Cocker, 2005), removing toxic particles with Electrostatic Precipitators (Yang et al., 2007), and measuring surface area of particles (Fissan et al., 2007; Shin et al., 2007). Unipolar charging has recently attracted particular attention due to its higher charging efficiency than bipolar diffusion charging for nanoparticles (Chen and Pui, 1999), which are considered as building blocks for nanotechnology.

One of the main advantages of diffusion charging over other charging processes, such as photoionization, is its smaller material dependence, as predicted by diffusion charging theories (Fuchs, 1963; Marlow and Brock, 1975; Davidson and Gentry, 1985). The material dependence described in diffusion charging theories is a weak function of the dielectric constant of materials, which functions through the image force due to the interaction between ions and particles. While Fuchs' theory (1963) has been widely used because of its good agreements with various experimental studies (Pui et al., 1988; Biskos et al., 2005), very few of them (Pui et al., 1988) explored the material dependence of unipolar diffusion charging. Furthermore, most of these experimental

studies focused on the measurement of intrinsic charged fraction only. The intrinsic charged fraction is defined as the possibility of uncharged particles entering the charger to acquire charges in the process independent of their fates (either to penetrate through the charger or to deposit to the wall of the charger). In transition and continuum regime, it becomes difficult to study intrinsic charged fraction for unipolar charging because it reaches close to 100% for many unipolar chargers. Some attempts of measuring the mean charge and the charge distribution on monodisperse particles in transition and continuum regime were made and showed reasonably good agreements with Fuchs' theory under certain conditions (Biskos et al., 2005). However, no material dependence study has been done for mean charge or charge distribution measurements. In addition, problems of missing the information of the charged particle loss in a unipolar charger and the possible effect of particle morphology remain unsolved for these measurements, which make the comparison with Fuchs' theory arguable. Most unipolar chargers have an electrical field in the charging zone which leads to substantial loss of charged particles. Unlike the measurement of intrinsic charged fraction, which can be accurately obtained regardless of the charged particle loss because uncharged particles are actually measured (Romay and Pui, 1992), the measurement of mean charge and charge distribution can be made only for those charged particles that survived through the charger. However, there is no technique available to obtain the charge distributions of the particles lost in the charger. In addition, the presence of an electrical field in the charging zone also involves field charging, which should be avoided if the experimental results need to be compared with Fuchs' theory, which is for diffusion charging only. When testing particles in the transition and continuum regimes, great care needs to be

taken of for particle morphology since flame synthesized (Biskos et al., 2005) and furnace generated aerosols (Shin et al., 2007) often contain agglomerates. It was reported that agglomerated particles have larger mean charge than spherical particles with the same mobility diameter for unipolar charging (Oh et al., 2004). Since the Fuchs' theory assumes that the particles are spherical, it is desirable to make these measurements for particles with spherical or compact morphology in a charger with negligible charged particle loss. In this study, a unipolar diffusion charger that has been implemented in three commercial instruments (Electrical Aerosol Detector, TSI 3070A; Nanoparticle Surface Area Monitor, TSI 3550 and AeroTrak 9000; UFP Monitor, TSI 3031) was used and proved to have minimized particles loss by eliminating electrical field in the charging zone (Medved et al., 2000).

The goal of this work is to examine the effect of dielectric constant on unipolar diffusion charging. Intrinsic charged fraction was measured for particles with the electrical mobility diameter d_m = 10-50 nm and mean charge was measured for particles with d_m = 50-200 nm.

7-2. Theory

In Fuchs' charging theory, the interaction potential at a distance *r* from the center of a particle with *n* elementary charges, i.e. $\phi(r)$, is a key component of the combination coefficient of ions and particles, i.e. β_c, and it is expressed as:

$$\phi(r) = \int_r^\infty F_i \, dr = K_E \left[\frac{ne^2}{r} - \kappa_p \frac{e^2 a^3}{2r^2 (r^2 - a^2)} \right], \qquad (7\text{-}1)$$

where F_i: the ion particle interaction force; $K_E = 1/4\pi\varepsilon_0$ in the SI unit system with the vacuum permittivity ε_0; $\kappa_p = (\varepsilon - 1)/(\varepsilon + 1)$ with the dielectric constant ε; a: the radius of particle, e: elementary charge. In Eq. (1), the first term in the parenthesis corresponds to Coulomb force, while the second term corresponds to image force, where material dependence functions. Particles of three different materials were examined: Ag ($\varepsilon = \infty$), NaCl ($\varepsilon = 6.1$), and Sucrose ($\varepsilon = 3.3$). Hence, the three test materials cover a wide range of κ_p, which is 1.00 for Ag, 0.72 for NaCl and 0.53 for Sucrose. Particle generation was specially designed to ensure particles' spherical or compact morphology as described in the following section.

7-3. Experimental

The particle generation system is shown in Figure 7-1 (a). a sintering process was used to generate spherical Ag particles. Ag wire (purity level 99.9 %) was placed in a ceramic boat which was placed inside a quartz tube of an electric furnace. Dry nitrogen was used as carrier gas passing through the quartz tube and the flow rate was 1.5 L/min. Silver was vaporized in the furnace operating at 1100 °C and primary particles were formed downstream of the furnace by condensation. The primary particles then grew to larger agglomerates by coagulation in the agglomeration chamber. The agglomerates were subsequently fully sintered at 600 °C (Ku and Maynard, 2006) in the second furnace so that the morphology of the particles turned into spherical. To generate NaCl and Sucrose particles, solutions of NaCl and Sucrose

with 0.1 % volume concentration in deionized water were atomized in a home-made Collison atomizer and the droplets were passed through a diffusion dryer to evaporate the water and leave only solid particles. Silica gels in the diffusion dryer were replaced frequently with fresh ones to ensure dry particles formation and the same low relative humidity for all the measurements. Silver, NaCl, and Sucrose nanoparticles are size-classified by a Differential Mobility Analyzer (DMA, Model 3081, TSI Inc.). The sheath flow and aerosol flow rates for the DMA were 5 L/min and 0.5 L/min, respectively, to ensure high monodispersity. Scanning Electron Microscopy (SEM) images of sintered silver particle, NaCl particle, and Sucrose particle are shown in Figure 7-2. The particle morphologies are all compact and almost spherical.

The monodisperse aerosol from the DMA was sent into a Po-210 neutralizer followed by the test unipolar charger The operational flow rate through the test charger was controlled by an aerosol electrometer (model 3068, TSI Inc.) and a UCPC (model 3025A, TSI Inc.) downstream operating at 1.0 and 1.5 L/min, respectively. So the total flow rate through the test charger, i.e., 2.5 L/min, is the same as those used in the corresponding commercial instruments. This charger charges the aerosol particles by diffusion in a chamber with two colliding turbulent jet flows carrying aerosol particles and positive ions, respectively. Downstream of the charger, an ion trap voltage of 20 Volt was used to completely eliminate the highly mobile residual ions in the aerosol stream but ensure a negligible charged particle loss in the ion trap.

Schematic diagram for experimental set-up to obtain intrinsic charged fraction is shown in Figure 7-1 (b). The intrinsic charged fraction η_i is expressed as:

$$\eta_i = 1 - \frac{N_u}{N_T} = 1 - \exp\left(-\beta_{c0}\ N_i\ t\right), \qquad (7\text{-}2)$$

where N_u is the number concentration of uncharged particles downstream of the charger; N_T is the total number concentration of particles; β_{c0} is the combination coefficient between ions and uncharged particles; N_i is the ion concentration; t is the residence time in the ion environment. In the experiment, singly charged monodisperse particles exiting the DMA were passed through a Po-210 neutralizer and the first electrostatic precipitator (ESP) to allow only uncharged particles to enter the test charger. The ESP consists of a metal wire and tube and uses electrostatic forces to eliminate charged particles. N_T and N_u were measured downstream of the charger when it was turned off and on, respectively.

For the test charger, 50 nm particles have intrinsic charged fraction close to 100% for all the three test materials. Hence, it is not appropriate to investigate the material dependence by comparing intrinsic charged fraction of larger particles. Instead, the comparison was made by measuring mean charge per particle. Figure 7-1 (c) shows the experimental set-up to obtain mean charge per particle at the exit of the test charger by measuring number concentration with the UCPC (N_{UCPC}) and electrical current (I) with the aerosol electrometer in parallel. Mean charge per particle N_p is equal to I / $(N_{UCPC}\ Q_e\ e)$, where Q_e is the flow rate into the electrometer, 1.0 L/min.

7-4. Results and discussion

7-4-1. Intrinsic charged fraction

Firstly the charged particle loss in the charger was measured with monodisperse NaCl particles and it was found that there is a very small particle size dependent loss, i.e., particles larger than d_m = 30 nm have less than 10% loss. This observation is in agreement with the work of Medved et al (2000). It enables the meaured mean charges from this study to be compared with estimates based on Fuchs' theory.

The measured intrinsic charged fraction is shown in Figure 7-3. Overall, the results of intrinsic charged fraction are very close for the three tested materials. The small error bars represent the standard deviation of 7 repeat measurements on two different days for each data point, suggesting a good repeatability of the experiment (the same for the error bars in Figure 7-4). As shown in Eq (7-2), intrinsic charged fraction is determined by both β_0 and $N_i t$. From Fuchs' theory, the difference of β_0 is estimated to be about 20 % between Ag and Sucrose, and about 12 % between Ag and NaCl for particles ranging from 10 to 50 nm. However, most unipolar charging processes usually have very large $N_i t$ value, e.g. larger than 10^7 s/cm^3, which becomes the dominant factor of the exponential function in Eq (7-2). Therefore, the difference of β_0 for different materials comes to a diminished difference of intrinsic charged fraction for the studied unipolar charging process as observed in Figure 7-3.

7-4-2. Mean charge per particle

Figure 7-4 shows the mean charge per particle for the three materials. The results from modeling based on Fuchs' theory are also presented to illustrate the estimated material dependence. In this study, obtaining $N_i t$ experimentally for Fuchs'

modeling is not straightforward because the tested charger has a significant turbulent flow due to two cross jets (Medved et al., 2000), which might also lead to an inhomogeneous ion distribution and incomplete mixing. Hence, the $N_i t$ value (2.7×10^7 s/cm^3) was obtained by fitting the experimental result of Ag. The fitting $N_i t$ was then used to calculate the mean charge of the other two materials so that the difference can be compared. The ion properties used in the calculation are: ion mobility of 1.15 cm^2/Vs and ion mass of 290 amu (Wiedensohler, 1988). In Figure 7-4, the results of Fuchs' modeling indicate that the differences of mean charge per particle among different materials in the tested particle size range is very small, i.e., about 10.5 % between Ag and Sucrose; and 5.2 % between Ag and NaCl. The level of the small difference observed from experimental data is consistent with that from Fuchs' modeling as shown in Figure 7-4. The results indicate that the material dependence from experimental data agrees well with that estimated by Fuchs' theory. Obviously, particles with larger dielectric constant can obtain more charges in unipolar charging, and this difference appears to exist consistently for all the sizes studied in this study, but not only for particles smaller than 50 nm as widely believed (Biskos et al., 2005). Since the relationship between mean charge and particle diameter is linear, the slopes calculated from both experimental data and Fuchs' theory were summarized in Table 7-1 so that the comparison can be quantitatively demonstrated. Besides the high $N_i t$ value for unipolar charging as explained previously, multiple charges on particles also contribute to the fact that the material dependence is insignificant. As shown in Figure 7-4, particles larger than 50 nm obtained multiple charges in the unipolar charging process. Once these particles acquire the first charge during charging process, Coulomb force

becomes the dominant term over image force in Eq (7-1). Therefore, the material dependence of unipolar charging, which originates from the image force term, becomes diminished.

7-5. Conclusions

In this chapter, material dependence of unipolar diffusion charging was investigated over a wide range of dielectric constants in terms of intrinsic charged fraction and mean charge per particle. Experimental results show that the material dependence of unipolar diffusion charging for particles ranging from 10 to 200 nm is very small. The level of the small difference is consistent with the estimation from Fuchs' theory.

Materials	Experiment	Fuchs' theory
Ag	0.0500±0.0005	0.0484
NaCl	0.0476±0.0011	0.0459
Sucrose	0.0452±0.0018	0.0433

Table 7-1. Comparison of slopes between mean charge per particle and mobility diameter for different materials

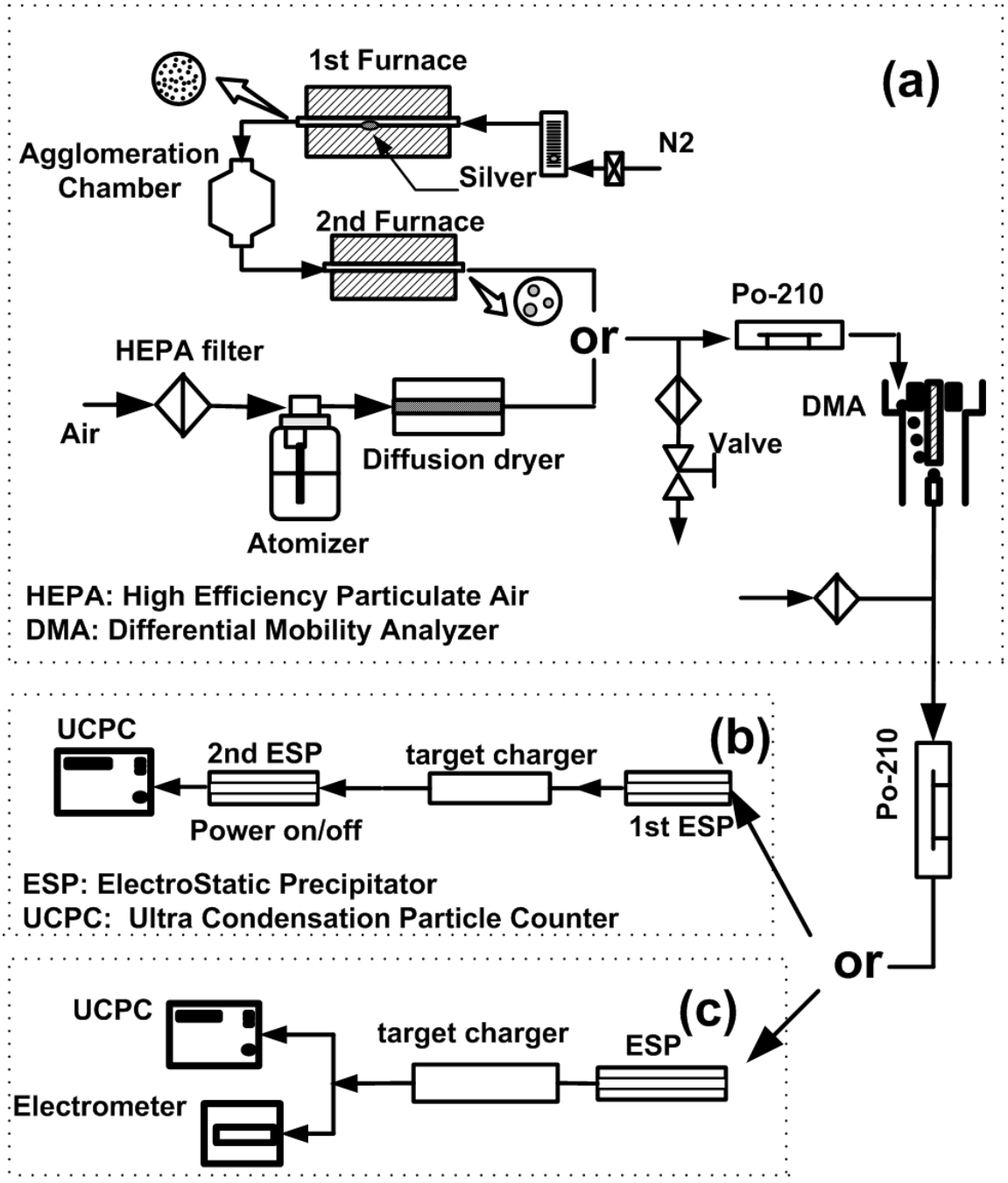

Figure 7-1. Experimental set-up: (a) particle generation of Ag, NaCl, and Sucrose (b) measurement of intrinsic charged fraction (c) measurement of mean charge per particle

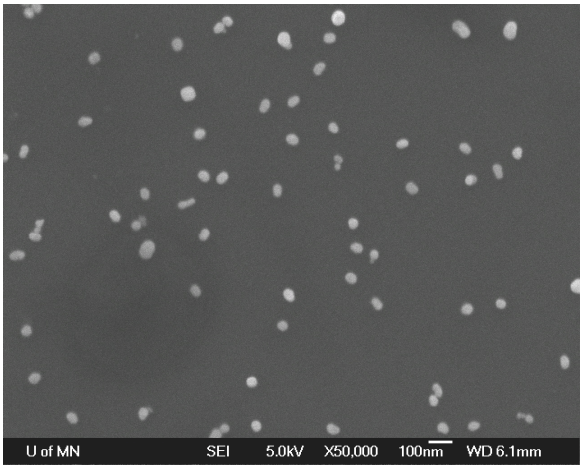

(a)

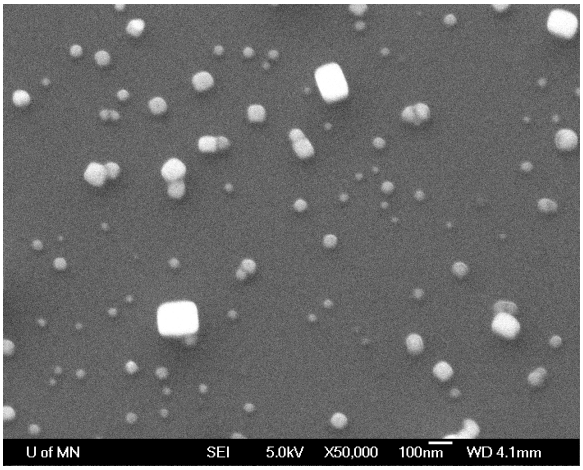

(b)

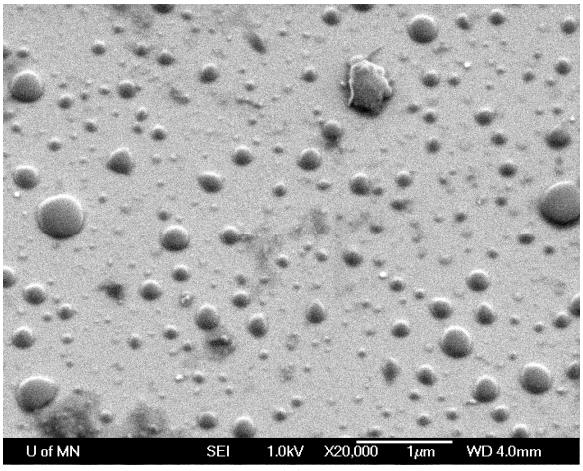

(c)

Figure 7-2. SEM images of polydisperse particles: (a) sintered Ag particles, (b) NaCl particles, (c) Sucrose particles

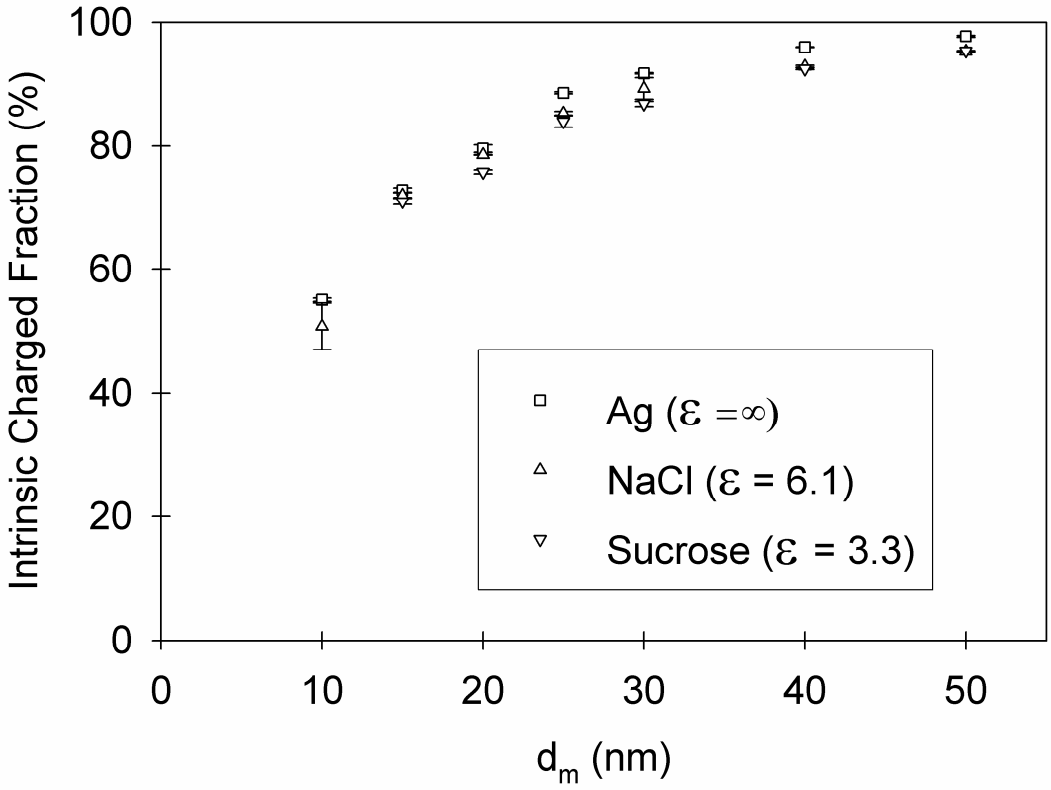

Figure 7-3. Comparison of intrinsic charged fraction for different materials

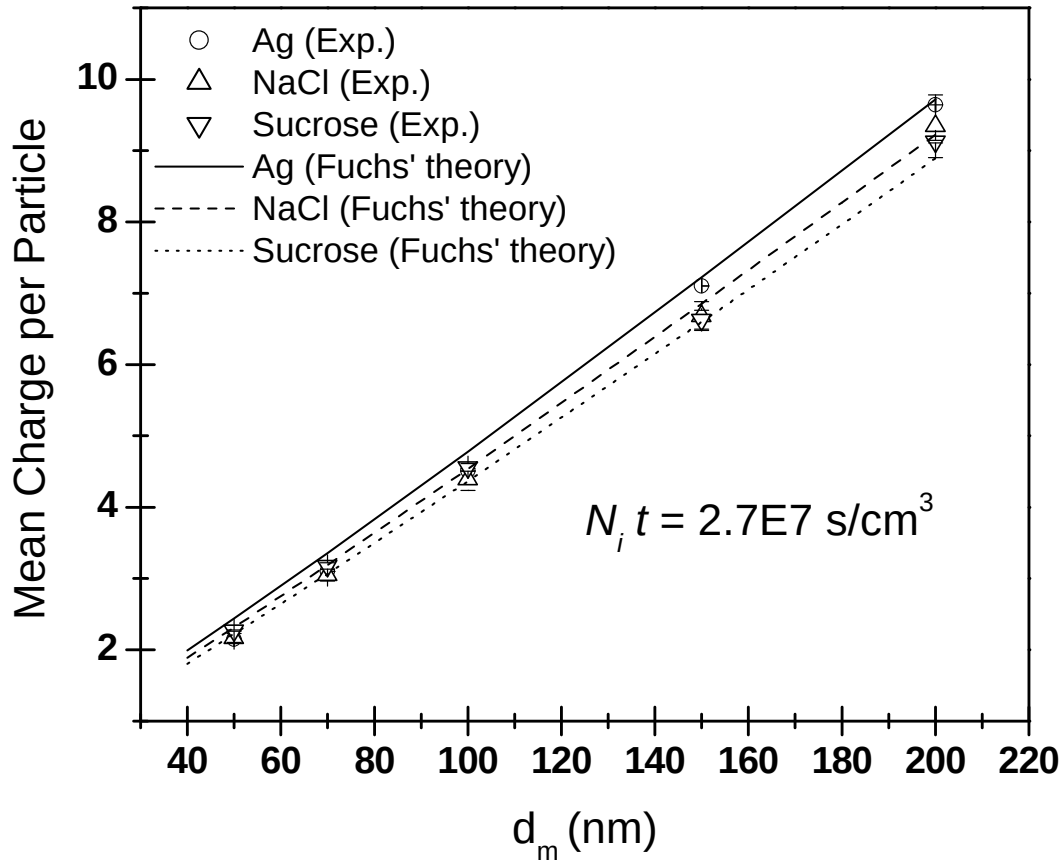

Figure 7-4. Comparison of measured mean charge per particle for different materials

Chapter 8 The Effect of Particle Morphology on Unipolar Diffusion Charging of Nanoparticle Agglomerates in the Transition Regime

8-1. Introduction

Atmospheric and intentionally produced aerosol particles are often nonspherical. Soot particles are agglomerates that are almost always found in the ambient aerosol (Katrinak et al., 1993). Flame and furnace-generated particles such as TiO_2 and Ag particles with industrial applications also have agglomerate morphologies (Pratsinis, 1998; Ku and Maynard, 2006). The physical and chemical characterization of nonspherical and fractal agglomerate particles is an important area of current aerosol research (Friedlander and Pui, 2004).

Most diffusion charging theories assume that particles are spherical. The diffusion charging process is determined by the ionic Knudsen number Kn_{ion}, defined as the ratio of the ionic mean free path λ_i to the particle radius:

$$Kn_{ion} = \frac{\lambda_i}{a}. \tag{8-1}$$

In the continuum regime ($Kn_{ion} \rightarrow 0$), the diffusion charging is well described by the diffusion-mobility theory, which is based on the solution of the continuous diffusion equation for ions in the electric field of a charged particle (Fuchs, 1963). This theory

has been experimentally verified by many researchers (Kirsch and Zagni'tko, 1981; Liu and Pui, 1977). For the transition regime ($0.1 < Kn_{ion} < 10$) and free molecule regime ($Kn_{ion} \rightarrow \infty$), the situation is much more complex. A great number of independent theories were reported. The complexity comes from the breakdown of continuous diffusion theories for distances of the same order as the ionic mean free path, because the transport process is controlled by both continuum and free molecular mechanisms. Among those theories Fuchs' limiting sphere theory (Fuchs, 1963) has been the most widely used. And it has been verified by several experimental studies (Pui et al., 1988; Biskos et al., 2004; Qi et al., 2008; Shin et al., 2009d).

It has been reported that the particle morphology affects both bipolar and unipolar charging processes (Cheng and Yeh, 1981; Wen et al., 1984a, b; Rogak and Flagan, 1992; Laframboise and Chang, 1977; Chang, 1981; Han and Gentry, 1994; Oh et al., 2004; Biskos et al., 2004). Nevertheless, less is still known about the charging of non-spherical particles such as asbestos fibers and fractal agglomerates.

There are several previous studies on the bipolar charging characteristic of non-spherical particles. Cheng and Yeh (1981) developed a theory for the equilibrium bipolar charge distribution on chain aggregates. Wen et al. (1984a) introduced the concept of the charging equivalent diameter for the bipolar diffusion charging and Wen et al. (1984b) found a good agreement of experimental results with the Boltzmann charge distribution when using the charging equivalent diameter derived for conducting prolate speroids. Rogak and Flagan (1992) showed that the uncharged fraction was ~5 % lower for the agglomerates than for spheres with the same mobility in the size range of 100 to 800 nm. From previous results, one can find that there is no much difference

between non-spherical and spherical particles for bipolar diffusion charging characteristic.

Most theories of unipolar diffusion charging (White, 1951; Gunn, 1954; Liu et al., 1967; Gentry, 1972; Pui, 1976; Liu and Pui, 1977; Pui et al., 1988) assume spherical particles. Laframboise and Chang (1977) developed the theory of charge deposition on charged aerosol particles of arbitrary shape for the unipolar charging process. Chang (1981) proposed equations for the mean charge of arbitrarily shaped particles in unipolar diffusion charging process. The proposed equations indicate that in the continuum regime mean charge per particle is determined by the electrical capacitance of particle while in the free molecule regime it is determined by the geometric surface area as well as the capacitance of the particle. Rogak and Flagan (1993) and Filippov (1994) also pointed out that electric capacitance is affected by particle morphology using an analogy between electrostatics and diffusion. Han and Gentry (1994) showed that large surface area and low electric potential enhance the rate of charge acquisition using computational method based on population balance equations. Oh et al. (2004) used an indirect photoelectric charger in their experiments and showed that TiO_2 agglomerates with a low fractal dimension have more charges than spherical particles by about 30 %. Biskos et al.(2004)'s Monte-Carlo simulation results indicate that for non-spherical particles shape and charge distribution on particle are important factors for unipolar diffusion charging.

From the literature, one can find that geometric surface area and electrical capacitance are two important factors, which determine the unipolar charging characteristics of non-spherical particles. For the surface area, Rogak et al. (1993), Oh

et al. (2004), Shin et al. (2009b) showed that projected area equivalent diameter of agglomerate particle is close to mobility diameter of the particle with Si, TiO_2, and Ag agglomerates. Keller et al. (2001) indicated that the geometric surface area of particles increases as the fractal dimension decrease for the same mobility diameter. However, it may be arguable because the relationship may depend on the range of Knudsen number based on mobility diameter of particle. For the same volume diameter one can say that agglomerate particles have larger geometric surface area than spherical particles not depending on particle size. During sintering process the volume of particle is kept the same. For the capacitance of particles, it is known that electrical capacitance of doublet particle is higher than that of singlet sphere (Brown and Hemingway, 1995). There is no exact analytical solution for the capacitance for agglomerates consisting of more than 2 spheres. For the electrical capacitance of loose agglomerate particle consisting of many primary spheres, Brown and Hemingway (1995)'s approach using variational method can be used. The variational calculation gives a better answer than any of the other approximate theories. Brown and Hemingway showed that their analysis results are in a good agreement with their experimental results and their approach can be applied to any agglomerates of spheres of any size and in any spatial configuration.

This study examines the effect of agglomerate morphology on unipolar charging characteristic in terms of the mean charge per particle. In this study, a unipolar diffusion charger that has been implemented in three commercial instruments (Electrical Aerosol Detector, TSI 3070A; Nanoparticle Surface Area Monitor, TSI 3550 and AeroTrak 9000; UFP Monitor, TSI 3031) was used and proved to have minimized particles loss by eliminating electrical field in the charging zone (Medved et al., 2000; Shin et al,

2009d). This charger allows me to compare experimental data with unipolar charging theories assuming no particle loss in the charger. The effect of geometric surface area and electrical capacitance on the unipolar diffusion charging was investigated in more detail using mobility analysis (Lall and Friedlander, 2006). A new model was developed to predict the electrical capacitance of loose agglomerate particles as a function of mobility diameter by combining Brown and Hemingway (1995)'s approach with Lall and Friedlander (2006)'s model. In the experiments, sintering process was used to change agglomerate morphology of silver. Experimental data for the mean charge of silver agglomerate was compared with estimates based on Chang (1981)'s model. In the comparison, the effect of more real morphology, i.e., a branch of agglomerates, on unipolar charging was also investigated. As a baseline, the mean charge of silver sphere was compared with Fuchs' modeling results (1963).

8-2. Theoretical backgrounds

8-2-1. Diffusion charging theory

The theory of charge deposition on charged aerosol particles of arbitrary shape was developed by Laframboise and Chang (1977). The theory assumes a stationary (no flow), constant-property, frozen chemistry environment with no magnetic field, and only slight ionization, and the electric potential, V_p, near a particle obeys Laplace's equation. The particle surface is at a uniform potential as is the case if the particle is conductive. Laframboise and Chang (1977) assumed that ion transport to the particle is

governed by the continuum flux equation and also ions have a sticking probability α per collision with the particle surface. Chang (1981) re-examined the theory of Laframboise and Chang for arbitrarily shaped particle and provided simpler equations depending on the Kn_{ion}. Chang conducted systematical analysis only for oblate and prolate spheroids. Chang (1981) proposed that the mean charge per particle (N_p) which arbitrarily shaped particles obtain from unipolar diffusion charging is governed by the following equations:

in continuum regime ($Kn_{ion} \rightarrow 0$),

$$\begin{aligned} N_p &\cong (C_p N_i D_i t)/\varepsilon_0 \qquad (\varphi_p < 0.1) \\ &\cong \frac{2C_p kT}{e^2}\left[\left(\frac{e^2}{kT}\frac{N_i D_i t}{\varepsilon_0}+1\right)^{0.5}-1\right] \qquad (\varphi_p < 1), \end{aligned} \tag{8-2a}$$

and in free molecule regime ($Kn_{ion} \rightarrow \infty$),

$$N_p = \frac{2C_p kT}{e^2}\ln\left(1+\frac{e^2 N_i \bar{v} S_p t}{4kT C_p}\right), \tag{8-2b}$$

where C_p is capacitance, ε_0 the permittivity of vacuum, D_i the ion diffusion coefficient, k the Boltzmann's constant, φ_p is the nondimensional potential, eV_p/kT (=$(e^2N_p)/(C_p kT)$), $\bar{v}$ is ion mean thermal velocity, and S_p is the geometric surface area of particle. However, for the case of $\varphi_p > 1$, the approximate equation (8-2a) cannot be used.

Original equation to relate the electrical potential with charger parameters is also shown in Chang (1981)'s study as follows:

$$\sum_{j=1}^{\infty}\left\{\frac{\varphi_p^j}{j \cdot j!}\right\} = \frac{e^2}{kT}\frac{N_i D t}{\varepsilon_0}. \tag{8-3}$$

Mean charge per particle can be numerically obtained from Eq. (8-3). Equations (8-2a) and (8-2b) indicate that in the continuum regime mean charge is determined by the electrical capacitance of particle while in the free molecule regime it is determined by the geometric surface area as well as the capacitance of the particle.

8-2-2. Mobility theory for loose agglomerates

For the agglomerate particles with open structure (fractal dimension < 2), many investigators have approximated drag force on the agglomerate consisting of primary particles in the free molecule regime as simply the sum of the drag forces on all the primary particles. In other words, the friction coefficient of loose agglomerate particle is proportional to the number of primary particles. Chan and Dahneke (1981) made Monte Carlo computations for the drag on the basic chain units (BCU) which consists of two hemispheres touching at their poles. For a straight chain, i.e., a loose agglomerate, Lall and Friedlander (2006) assumed that an agglomerate and a sphere trace the same path in the classifier if their migration velocities are equal to each other. Then Lall and Friedlander obtained a relationship between primary particle diameter (d_p) and mobility diameter using Chan and Dahneke (1981)'s expression for the friction coefficient of a loose agglomerate as:

$$N = \frac{12\pi\lambda}{c^* d_p^2} \frac{d_m}{C_c(d_m)}, \tag{8-4}$$

where c^* is constant regarding particle orientation and λ is the mean free path of gas and C_c (d_m) is Cunningham slip correction factor. Lall and Friedlander (2006) obtained a

relationship between N and d_m was as a function of d_m with a known primary particle size.

Shin et al. (2009b) investigated structural properties of silver nanoparticle agglomerates using transmission electron microscopy. It shows that the 2-D fractal dimension of silver agglomerates was measured to be in a range of 1.75 to 1.84. The values are close to 1.78, i.e., the fractal dimension for self-similar aggregates produced by diffusion limited cluster aggregation (DLCA) in aerosols (Jullien and Botet, 1987). The fractal dimensions obtained from projections are 10-15 % lower than the fractal dimensions of the three dimensional agglomerates (Samson et al., 1987). Thus, it is still worthwhile to make use of Lall and Friedlander (2006) for the mobility analysis. Shin et al. (2009b) also pointed out that there are several characteristics of real agglomerates that are not incorporated in existing models for agglomerate dynamics: (1) It is not a chainlike agglomerate (2) There are significant neckings between primary particles. Neck formation can occur in silver agglomerates (Weber and Friedlander 1997; Lall et al. 2006) (3) Primary particles are polydisperse. These non-ideal effects may cause a discrepancy between experimental results and theoretical predictions.

8-3. The relationship between the number of primary particles and electrical capacitance and surface area of agglomerate particle

In this section, using a newly developed model based on Lall and Friedlander (2006) and Brown and Hemingway (1995) mean charge of loose agglomerate particle is

predicted. The model relates the number of primary particles, *N*, with electrical capacitance and geometric surface area of agglomerate particle.

8-3-1. The effect of particle morphology on electrical capacitance

The electrical properties of aerosol particles depend on their capacitance and spatial charge distribution. Brown and Hemingway (1995) developed a model to calculate electrical capacitance of agglomerate and charge distribution on the agglomerate which minimizes the electrostatic energy of the chain agglomerate using a variational method. Also, their calculation and measurements were in a good agreement to each other for the electrical capacitance. Brown and Hemingway indicated that the theory can be applied to agglomerates of spheres of any size and in any spatial configuration.

In this study, normalized capacitance is defined as total electrical capacitance divided by electrical capacitance of single primary sphere expressed as:

$$C_p = 4\pi\varepsilon_o a, \tag{8-5}$$

where a is primary particle radius. From Brown and Hemingway's results one can find that the normalized capacitance, N_c, is smaller than the number of primary particles of agglomerate, N. In this study, the relationship between the number of primary particles of agglomerate, N, and the normalized capacitance, N_c, was modeled by combining mobility analysis based on Lall and Friedlander (2006)'s model with Brown and Hemingway's approach. The total capacitance of agglomerate particle can be expressed as:

$$C_{p,aggl.} = N_c\, C_p = \mathit{func}(N) C_p \ . \tag{8-6}$$

In Brown and Hemingway (1995)'s study, their assumptions are as follows: (1) materials are conductive; (2) Charge Q_i is located at the center of each primary particle. The calculations were compared with direct measurements of capacitance made on large-scale experimental simulations of aerosols, composed of steel sphere stuck together.

In this study, the electrical capacitance of planar and loose agglomerates made up of a few primary particles up to several hundred was estimated as a function of number of primary spheres, *N*. In this study, four different morphologies for agglomerates were considered including a spheroid as an approximate morphology for a chain agglomerate as shown in Figure 8-1. Silver agglomerate used in this study is closer to the morphology like Figure 8-1(e). The approximation chosen for planar and loose agglomerate is that each primary sphere in the agglomerate is given its own given electric charge Q_i, with the i_{th} spheres, of radius a_i and with its center at the point r_i.

For each chain agglomerate, cross agglomerate, and branched chain agglomerate with an aspect ratio β, the relationship between *N*, and N_c is obtained by solving the following three equations (8-7) and (8-9):

$$\sum_{i=1}^{N} Q_i = Q_{tot} \ , \tag{8-7}$$

$$\Phi_s = \sum_{i=1}^{N} \frac{Q_i^2}{8\pi\varepsilon_0 a_i} , \tag{8-8a}$$

$$\Phi_i = \frac{1}{2}\sum_{i=1}^{N}\sum_{\substack{i=1 \\ i\neq j}}^{N} \frac{Q_i Q_j}{4\pi\varepsilon_0 \left| r_i - r_j \right|} , \tag{8-8b}$$

$$\frac{\partial}{\partial Q_i}\left[\Phi_i + \Phi_s + k_l\left(\sum_{i=1}^{N} Q_i - Q_{tot}\right)\right] = 0 \text{ for all } i, \tag{8-9}$$

where Φ_s is the self energies of all the spheres in the agglomerate, Φ_i the pairwise interaction electrostatic energy of i_{th} primary sphere, k_l a Lagrangian multiplier, and Q_{tot} total charge on agglomerate particle. Equations (8-7) and (8-9) are linear simultaneous equations in $\{Q_i\}$ and k_l. The minimum electrostatic energy is obtained by minimizing electrostatic energy Φ ($=\Phi_s + \Phi_i$) with respect to each Q_i subject to the constraint in Eq. (8-7). After an approximation for the charge distribution, given by the $\{Q_i\}$is obtained, the capacitance of agglomerates is given by:

$$C = \frac{Q^2}{2\Phi} \text{ .} \tag{8-10}$$

The normalized capacitance of a spheroid is obtained by using Chang (1981)'s result:

$$C_p = 4\pi\varepsilon_0 a_s \sqrt{\beta_s^2 - 1} / \ln[\beta_s + (\beta_s^2 - 1)^{1/2}] \text{ for}(\beta_s \geq 1), \tag{8-11}$$

where a_s is the radius of the minor axis of the prolate spheroids and β_s is the aspect ratio of spheroids. In the analysis, chain agglomerates are approximated as long prolate spheroids following Wen et al. (1984a)'s approach. The length of the minor axis of the prolate spheroids is approximated by the diameter of primary particles in an agglomerate. For the straight chain, the length of the major axis is the sum of the diameters of all the primary spheres equal $N*a$. The aspect ratio β_s can thus be approximated by the total number of primary particles, N.

Figure 8-2 shows the effect of agglomerate morphology on the normalized capacitance, N_c. The values of normalized capacitances of chain agglomerate and spheroidal particles are close to each other and larger than those of cross-shaped agglomerate and a branched chain agglomerate with an aspect ratio, β = 1.6. From TEM image analysis of 50 particles, the silver agglomerates are found to have the aspect ratio of 1.6. This is as would be expected, since the less compact agglomerate allows the charge to be more widely spread, reducing the potential energy. In the range of $N \leq 300$, the difference of the magnitude of capacitance between chain agglomerate and cross-shape agglomerate is about 10 -15 %. The normalized capacitance was fitted to number of primary particles with a power law, i.e., $N_c = aN^b$. The power law equations for the range of $N \leq 300$ are shown as follows:

$$N_c = 0.5789\, N^{0.7692} \text{ for a chain agglomerate} \quad (8\text{-}12)$$

$$N_c = 0.4703\, N^{0.7874} \text{ for a branched chain agglomerate with } \beta\text{=1.6.} \quad (8\text{-}13)$$

Eqs. (8-12) and (8-13) were used to calculate the capacitance of agglomerate particle in the following analysis.

In this study, the relationship between the mobility diameter of agglomerate, d_m and the normalized capacitance, N_c, was modeled by combining mobility analysis based on Lall and Friedlander (2006)'s model with Brown and Hemingway's approach. In Figure 8-3, the electrical capacitance of agglomerates was plotted as a function of mobility diameter for the primary particle diameter d_p = 19.5 nm with a standard deviation of 6.1 nm, which was from 254 primary spheres. The difference in the magnitude of electrical capacitance between chain agglomerates and spheres becomes much larger as mobility size becomes larger. One can expect that the larger capacitance

of agglomerate particles makes the mean charge of the agglomerate particle larger compared to that of spherical particles with the same mobility diameter during diffusion charging process.

In Eq. (8-7), the electrical capacitance of agglomerate consisting of primary particles is a function of number of primary particles *N*. As primary particle size becomes larger, the electric capacitance becomes smaller because the number of primary particle size, *N*, becomes smaller. One can show that the electric capacitance of a chain agglomerate roughly changes by $1/\sqrt{d_p}$ for the same mobility size from the following relations:

$$N \sim 1/d_p^2 \quad ,$$
$$C_{p,aggl.} = N_c C_p \sim N^{0.77} C_p \sim d_p^{-1.54} d_p \sim d_p^{-0.54} \quad . \tag{8-14}$$

8-3-2. Geometric surface area of chain-like agglomerates

In the Eq. (8-2b), the geometric surface area affects the magnitude of mean charge per particle. For sphere, because mobility diameter is equal to geometric diameter, one can calculate geometric surface area of sphere, S_{sph} as follows:

$$S_{sph.} = \pi d_m^2 . \tag{8-15}$$

For loose agglomerate, the geometric surface area equals to the sum of that of primary particles of the agglomerate and is given as:

$$S_{aggl.} = N \pi d_p^2 . \tag{8-16}$$

The ratio of geometric surface area between sphere and agglomerate is expressed as:

$$R(d_m) = \frac{S_{aggl.}}{S_{sph.}} = \frac{12\pi\lambda}{c^* C_c(d_m)\, d_m}. \quad (8\text{-}17)$$

From Eq. (8-17), the ratio of geometric surface areas between loose agglomerates and spherical particles is not dependent on the primary particle size of agglomerates. Figure 8-5 shows that the geometric surface area of agglomerate particle is larger than that of sphere for d_m < 80 nm. More likely in the free molecule regime, the larger geometric surface area of agglomerate particles can contribute to make the mean charge of agglomerates larger compared to spheres with the same mobility diameter.

8-4. Experimental

The particle generation system is shown in Figure 8-6. A sintering process was used to generate spherical Ag particles. Ag wire (purity level 99.9 %) was placed in a ceramic boat which was placed inside a quartz tube of an electric furnace. Nitrogen gas was used as carrier gas passing through the quartz tube and the flow rate was 1.5 L/min. Silver was vaporized in the furnace operating at 1150 °C and primary particles were formed downstream of the furnace by condensation. The primary particles then grew to larger agglomerates by coagulation in the agglomeration chamber. The agglomerates were subsequently fully sintered at 600 °C in the second furnace so that the morphology of the particles turned into spherical (Ku and Maynard, 2006). Silver nanoparticles were size-classified by a Differential Mobility Analyzer (DMA, Model 3081, TSI Inc.). The

sheath flow and aerosol flow rates for the DMA were 5 L/min and 0.5 L/min, respectively, to ensure high monodispersity.

For the test charger, particles larger than 30 nm have intrinsic charged fraction close to 100% for three different test materials (Shin et al., 2009d). Hence, it is not appropriate to investigate the morphology dependence by comparing intrinsic charged fraction of larger particles. Instead, the comparison was made by measuring mean charge per particle. Figure 8-6 shows the experimental set-up to obtain the mean charge per particle at the exit of the test charger. The operational flow rate through the test charger was 2.5 L/min, is the same as those used in the corresponding commercial instruments. In the experiments, UCPC (TSI model, 3025) was operated with the inlet flow rate of 1.5 lpm and an electrometer operated with the inlet flow rate of 1.0 lpm. The monodisperse aerosol from the DMA was sent into a Po-210 neutralizer and Electrostatic Precipitator (ESP) followed by the test unipolar charger. The ion trap voltage was fixed at 20 V to remove extra ions coming from the unipolar charger chamber. By measuring number concentration with a UCPC (N_{UCPC}) and electrical current (I) with an aerosol electrometer in parallel, mean charge of the particle was determined. Mean charge per particle N_p is expressed as:

$$N_p = \frac{I_e}{N_{UCPC}\, Q_{UCPC}\, e}, \tag{8-18}$$

where N_{UCPC} is particle number concentration measured by UCPC.

8-5. Results and discussion

The value, $N_i t$, is an important parameter to obtain mean charge as shown in Eq. (8-2). The value, $N_i t$, is not changed depending on particle morphology because it is the characteristic of the charger. The charger uses two impinging jets to charge aerosol particles with positively charged unipolar ions. The turbulent flow caused by the two cross-jets makes measurement of the representative value of $N_i t$ very difficult. Thus, in this study, the value of $N_i t$ was obtained by passing through spherical particles into the target charger and then fitting the data points of mean charge per particle with Fuchs' theory. The obtained value of $N_i t$ is 2.5 E7/cm^3. The same method of fitting $N_i t$ was used by the previous studies (Qi et al., 2009; Shin et al., 2009d).

A similar charger operating with a different flow rate was reported to have very high transmission efficiency (Medved et al., 2000) due to the elimination of electrical field in the charging zone. The charged particle loss in the charger was measured with monodisperse NaCl particles and the result was reported in Shin et al. (2009d)'s study. It is demonstrated that particles larger than d_m = 30 nm have less than 10 % loss. This very small particle loss in the charger enables one to compare measurement results with Fuchs' theory for spherical particles.

In Figure 8-7, Transmission Electron Microscopy (TEM) images show that the morphology of silver agglomerate particles becomes more compact as the particles are sintered at higher temperatures. Almost a spherical particle was obtained at 600 °C while a loose agglomerate particle at room temperature condition. One thing one needs to note is that an agglomerate particle shown in Figure 8-7(a) is not completely transparent or loose in that agglomerate has some necking between primary particles

and primary particles are not completely spherical. These may cause a deviation of estimates of charging property from experimental results.

Experimental results showed that the mean charge per particle of a loose agglomerate is larger than that of a spherical particle, i.e., a fully sintered particle. Several experimental studies that examine arbitrarily-shaped particles show a significant difference in charging properties between non-spherical and spherical particles. Vomela & Whitby (1967) showed that diffusion charges of smoke particles are about 70 % higher than that of the equivalent sphere with the same volume. Oh et al. (2004) also showed that mean charge per particle of a loose agglomerate particle is about 30 % higher than that of a sphere with the same mobility diameter. Experimental data show that mean charge is proportional to mobility size in the size range of d_m = 30 nm to 200 nm. Mean charge per particle of silver agglomerates can be fitted with $0.0584 * d_m$ while that of spherical particles follows $0.0473 * d_m$. The averaged difference in the mean charge between the spherical particles and the agglomerates is approximately 23.5 % in terms of slope between the mean charge and the mobility diameter. Also, the mean charge per particle was theoretically estimated as a function of mobility diameter using Chang (1981)'s theory. In the Section 8-3, geometric surface area and electric capacitance were obtained with a newly developed model which combines Lall and Friedlander (2006)'s model with Brown and Hemingway (1995)'s approach. Figure 8-8 indicates that the mean charge per particle of a chain agglomerate is larger than that of a spherical particle. As discussed in the Section 8-3, the higher mean charge per particle of silver agglomerates is mainly due to the larger capacitance of agglomerate compared to that of spherical particle, not due to geometric surface area.

Fuchs' modeling result is in good agreement with experimental data for spherical particles. In order to obtain Fuchs' modeling results, the ion properties used in the calculation are: ion mobility of 1.15 cm^2/Vs and ion mass of 290 amu (Wiedensohler, 1988). In Figure 8-8, estimates of mean charge of agglomerate particle are plotted for two different agglomerate morphologies, i. e., a chain agglomerate and a branched chain agglomerate with an aspect ratio $\beta = 1.6$. When the aspect ratio, $\beta = 1.6$ is considered, the estimated mean charge is in a better agreement with experimental data. The range of Kn_{ion} in the experiments is 0.13 -0.51 based on the mobility diameter. Overall, for both spherical and agglomerate particles the comparison shows that Chang's continuum expression agrees better with the experimental results in this range.

8-6. Conclusions

The effect of particle morphology on the unipolar diffusion charging of agglomerate particles was investigated. In unipolar diffusion charging process, both geometric surface area and electrical capacitance are known as two important parameters to determine the mean charge of non-spherical particles.

The geometric surface area of loose agglomerates was estimated based on Lall and Friedlander (2006). A new model which can predict the electrical capacitance of agglomerate particles was developed based on Lall and Friedlander (2006) and Brown and Hemingway (1995)'s models. Analysis results show that for the same mobility diameter the geometric surface area of chain-like agglomerates is only larger than that

of spherical particles in the mobility size range below d_m = 80 nm. As particles have a looser morphology and becomes larger, the electrical capacitance becomes significantly larger compared to spherical particles with the same mobility diameter. Thus, the electrical capacitance contributes to increase the mean charge per particle of agglomerates more than the geometric surface area, especially in the transition regime.

Overall, experimental data show that the mean charges of silver agglomerates are by about 30 % larger compared to those of silver spheres. The estimates of geometric surface area and electrical capacitance were used to predict the mean charge from Chang (1981)'s model and the predicted results are reasonably in good agreement with experimental data.

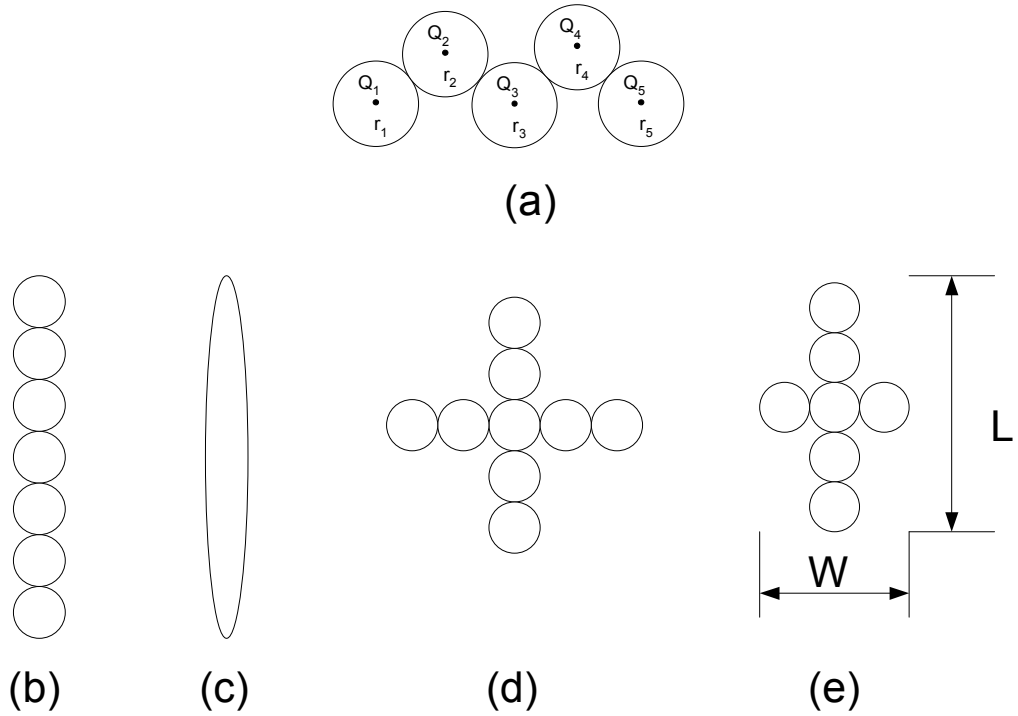

Figure 8-1. (a) Typical agglomerate parameters used in the calculation (b) a chain agglomerate (c) a prolate spheroid (d) cross agglomerate (e) a branched chain agglomerate with aspect ratio ($\beta = L/W$)

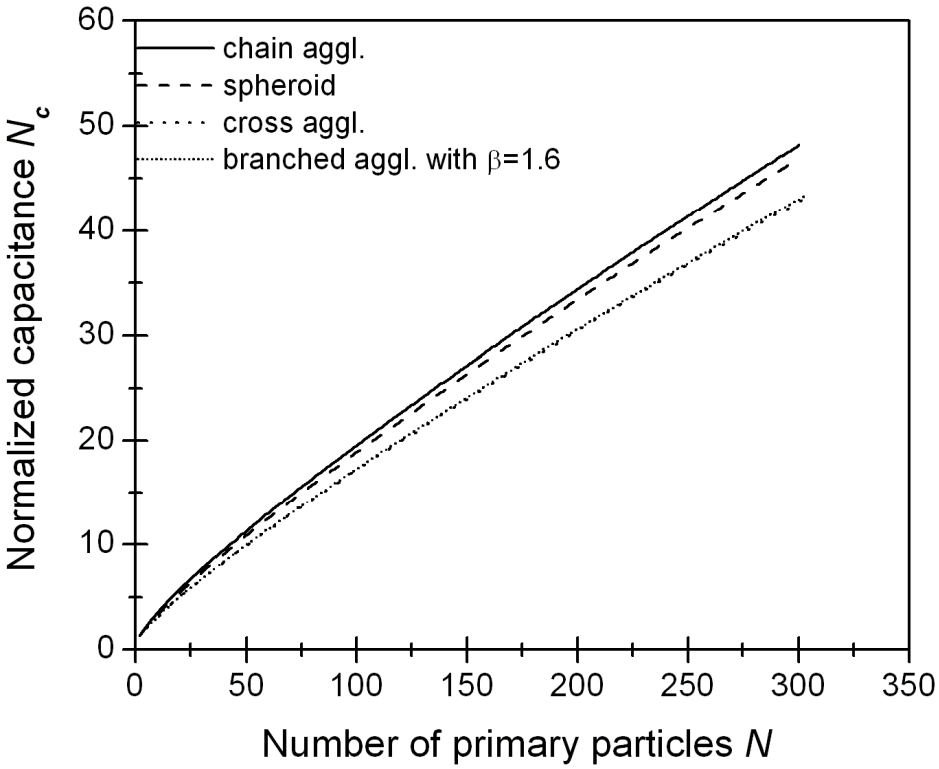

Figure 8-2. The relationship between normalized capacitance N_c and number of primary particles N

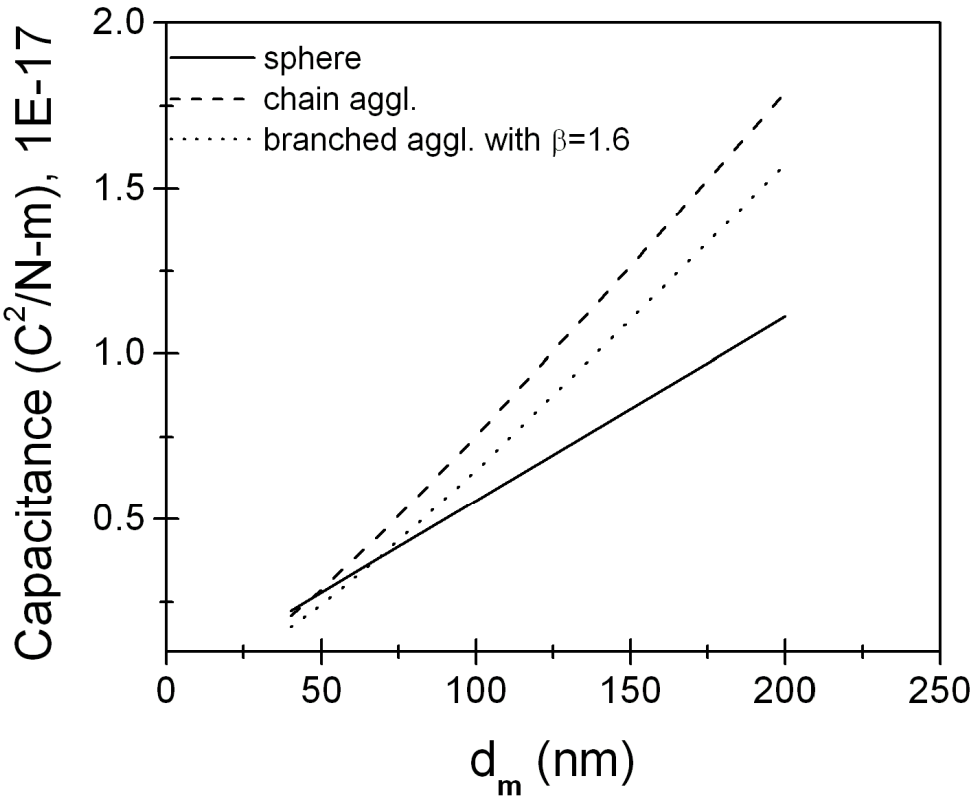

Figure 8-3. The effect of particle morphology on electrical capacitance as a function of mobility diameter

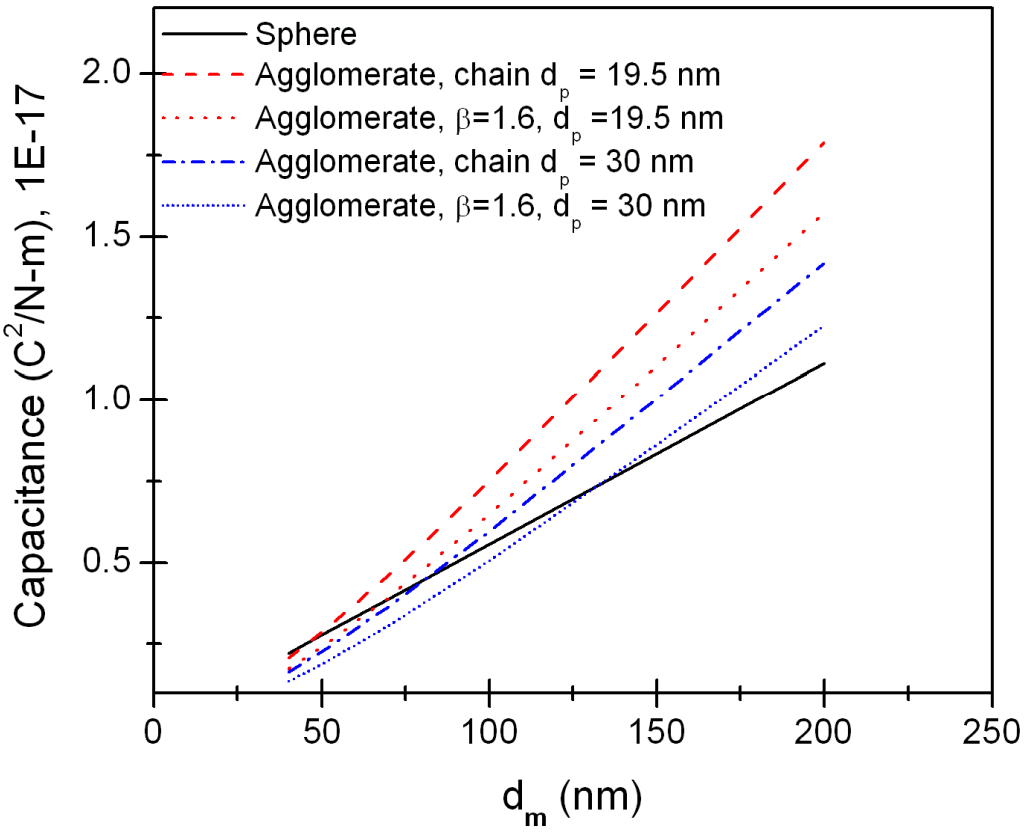

Figure 8-4. The effect of primary particle size on electrical capacitance as a function of mobility diameter

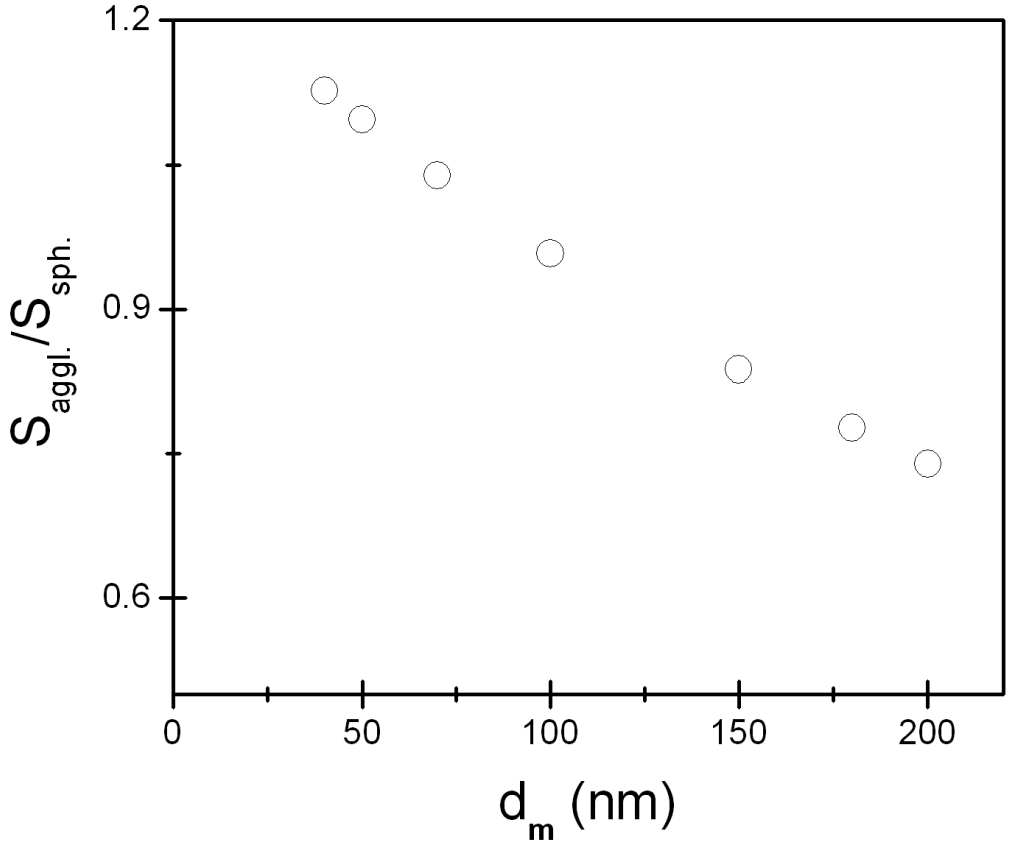

Figure 8-5. The ratio of geometric surface areas of agglomerate particle and spherical particle as a function of mobility diameter

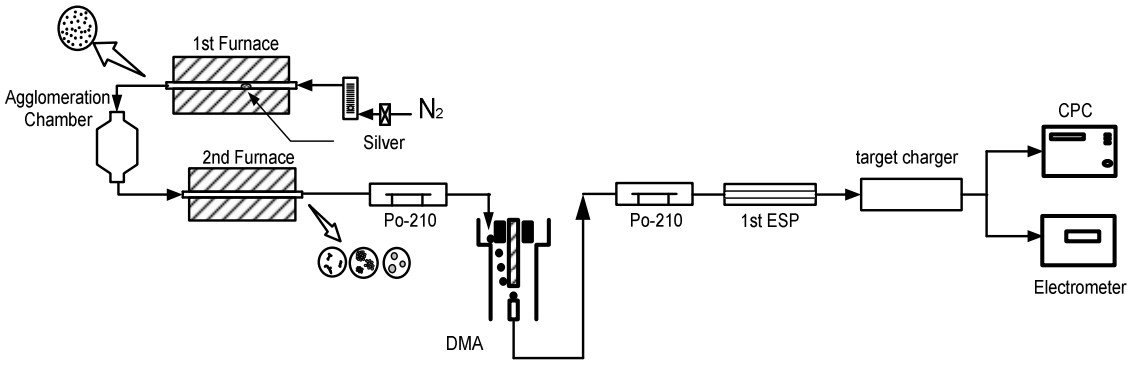

Figure 8-6. Schematic diagram for the measurement of mean charge per particle

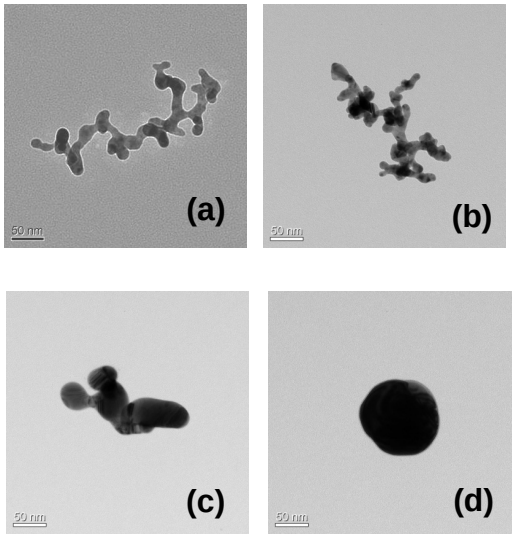

Figure 8-7. TEM images with different particle morphologies of silver nanoparticle for d_m = 120 nm (a) room temp. (b) 100 °C (c) 300 °C (d) 600 °C

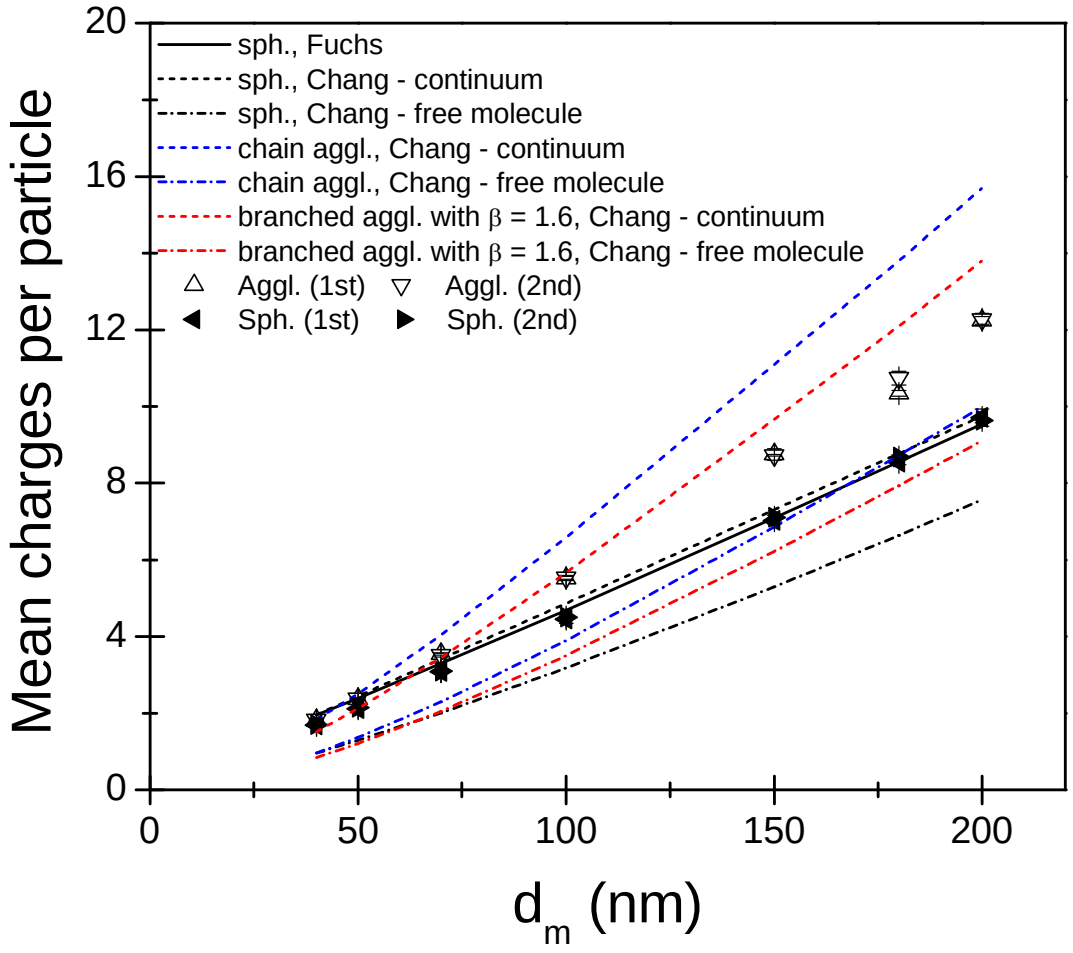

Figure 8-8. Comparison of mean charge per particle for agglomerates and spheres as a function of mobility diameter

Chapter 9 Conclusions and Recommendations

9-1. Summary and conclusions

In the first part of this thesis (Chapters 2, 3, 4, 5, and 6), studies on the mechanics of agglomerates particles were described. The friction coefficient f is a key quantity for describing the motion of an aerosol particle including its diffusion, electrical mobility, sedimentation, thermophoresis, and coagulation rate. Although understanding transport of real agglomerate particles is important for those processes, its quantitative studies are limited. Also, the existing models on the friction coefficient of agglomerates are limited to the free molecular regime. The accuracy of the existing models has not been investigated when the models are used for particles in the transition regime.

As a first step for quantitative studies, intensive TEM image analysis was conducted in order to obtain the structural properties of silver agglomerates such as projected area equivalent diameter (d_{pa}), fractal dimension (D_f), and number (N) of primary particles on an agglomerate (Chapter 2). The structural properties obtained from the TEM analysis of projected images were related to mobility analysis based on Lall and Friedlander (2006). 2-D structural properties obtained from TEM image analysis are comparable to those from Lall and Friedlander's model. However, the number of primary particles obtained from projected images may be an underestimate for real agglomerates because real agglomerates are not completely loose and

transparent. It indicates that 3-D approach is required. The results in Chapter 2 show that silver agglomerates used in this study are cluster-cluster agglomerates.

Using DMA-APM technique, a quantitative method for measuring dynamic shape factor κ and the exponent η was developed for agglomerates with mobility diameter in the range 50 nm to 300 nm (Chapter 3). The exponent η characterizes the relationship between friction coefficient and number of primary particles of agglomerates. Free molecular based models for cluster-cluster agglomerates are expected to lead to different results. The measured value of η in the size range less than 100 nm agrees within a few percent with the predictions based on Meakin et al. (1989)'s model. For larger agglomerates with d_m from 100 nm to 300 nm, the measured η decreases by 15 % while the predicted value increases by about 1 %. An empirical equation is given for the N dependence of the ratio of the measured friction coefficient to the Meakin free molecular expression. The observed decrease in η with increasing agglomerate size suggests a flow interaction between the primary particles not included in the existing models which are based on free molecular dynamics.

Using DMA-APM technique, the mass-mobility diameter scaling exponent D_{fm} was quantitatively measured with an uncertainty of about 3 % for the exponent for agglomerates with mobility diameter in the range of 50 nm to 300 nm (Chapter 4). For the exponent D_{fm}, the measured value decreases by about 1 % as the size ranged is increased while the predicted value based on Meakin et al. (1989) decreases by about 15 %. The near constancy of D_{fm}, which has also been discussed by Wang and Sorensen, is shown to result from both the exponent η and δ decreasing with increasing N. The

exponent δ characterizes the relationship between friction coefficient and mobility diameter.

Four non-ideal effects on the friction coefficient of agglomerates are estimated as perturbations to the Chan and Dahneke model (Chapter 5). These four non-ideal effects include polydispersity of primary particles, necking between primary particles, dependence of primary particle size on agglomerate size, and particle alignment. The variable primary sphere size effect results in the largest change from the idealized model with about a 10 % increase in both the friction coefficient scaling exponent η and mass-mobility diameter scaling exponent D_{fm}. This is also the characteristic with the most uncertainty. The second largest change is a 4 % decrease in the exponent η and a 4 % increase in mass-mobility diameter scaling exponent D_{fm} from the alignment in the electric field. The effects of necking between particles and polydispersity of the primary particles are negligible for the two exponents. The combined effect, excluding the variable primary particle size, results in a 17.5 % decreases in the dynamic shape factor for agglomerates with a 300 nm mobility diameter. Adjusting the model by this amount provides a significant improvement in the agreement between the model and silver agglomerate measurements for the dynamic shape factor.

Another independent measurement method, TDMA technique, was used together with TEM analysis in order to determine agglomerate volume, mass mobility diameter scaling exponent (Chapter 6). TDMA results are in a good agreement with DMA-APM data (Chapters 4) in terms of agglomerate volume and mass mobility diameter scaling exponent. TDMA results also show that the mass mobility diameter

scaling exponent is not dependent on mobility size range unlike prediction based on free molecular models and it reconfirms the results obtained using DMA-APM (shown in Chapter 4). Using TDMA technique, the extent of particle alignment in the electric field of DMA was measured for real agglomerates such as silver agglomerate particles with d_m = 300 nm. The alignment is shown to be consistent with model predictions in Chapter 5. The alignment results in a decrease in the mass-mobility diameter scaling exponent by 2 %.

In the second part of this thesis (Chapters 7 and 8), studies on the effect of dielectric constants of materials and the effect of particle morphology on unipolar diffusion charging were described.

In Chapter 7, the dependence of unipolar diffusion charging of nanoparticles on the dielectric constant of the particle material was experimentally investigated. The examined nanoparticles (10 – 200 nm) cover a wide range of dielectric constant but have almost the same spherical or compact morphology. Measurements of both intrinsic charged fraction and mean charge per particle show very small differences among different materials. The level of the small difference is consistent with the estimation by Fuchs (1963)' theory.

The effect of particle morphology on the unipolar diffusion charging of nanoparticle agglomerates was investigated in Chapter 8. Nanoparticle agglomerates consist of multiple primary spheres. In the unipolar diffusion charging of non-spherical agglomerates, geometric surface area and electrical capacitance of particles, which are related to particle morphology, are known as important parameters to determine mean

charge per particle. From mobility analysis the geometric surface area of chain-like agglomerates is found to be only larger than that of spherical particles with the same mobility diameter for mobility size range below d_m = 80 nm. Estimates of the electrical capacitance of agglomerates were calculated with a newly developed model based on electrostatics and mobility theories. The results show that the electrical capacitance of chain-like agglomerates becomes significantly larger compared to that of spheres with the same mobility diameter as particles become larger. Analysis results indicate that loose agglomerates have larger mean charge per particle compared to compact particles with the same mobility diameter because the electrical capacitance of agglomerates becomes larger as particle morphology becomes looser. Experimental data show that the mean charge of silver agglomerates is larger than that of fully coalesced silver spheres by about 30 %. The experimental data is reasonably in good agreement with the estimates of the mean charge of silver agglomerates.

9-2. Future work recommendations

Although this research has revealed many interesting aspects regarding mechanics and unipolar diffusion charging of agglomerate particles, there are still many issues to be addressed in the future.

This research on the mechanics of agglomerate particles showed that estimates of dynamic properties of agglomerates based on a free molecular analysis deviate from the measured results. In the existing free molecular models, flow interaction between

primary particles and non-ideal effects are not included. Therefore, new simulation techniques need to be developed to address the abovementioned issues. Examples of such a study could be on the friction coefficient of agglomerate particles with necking between primary particles or consisting of polydisperse primary particles. In this study, it was found that silver agglomerates with d_m = 300 nm are partially aligned in the electric field intensity of 9 kV/cm. However, the magnitude of electric field intensity making agglomerates fully aligned or randomly oriented is not known. Therefore, an investigation of particle alignment effect on the mobility size of real agglomerates for a wider range of electric field intensity could be of particular interest.

This research on the unipolar diffusion charging of real agglomerate particles showed that electrical capacitance of an agglomerate is a morphology related parameter which affects the charging property. One can expect that this phenomenon would be more significant for carbon nanotubes and nanorods with a large aspect ratio. This issue needs to be further analytically and experimentally investigated. It also could help the development of a new unipolar charging model or modification of existing models.

Bibliography

[1] Baltensperger, U., Gäggeler, H. W. and Jost, D. T. (1988) The epiphaniometer, a new device for continuous aerosol monitoring. J. Aerosol Sci. 19(7), 931-934.

[2] Barnes, L. L. (1934) The Emission of Positive Ions from Heated Metals. *Phys. Rev.* 42:487-491.

[3] Biolsi, L. and Holland, P. M. (2007) Theoretical calculation of the low-density transport properties of monatomic silver vapor. Int. J. Thermophys. 28:835 -845.

[4] Biskos, G., Mastorakos, E., and Collings, N. (2004) Monte-Carlo simulation of unipolar diffusion charging for spherical and non-spherical particles. Journal of aerosol science 35: 707-730.

[5] Biskos, G., K. Reavell, K., and Collings, N. (2005). Unipolar diffusion charging of particles in the transition regime. J. Aerosol Sci. **36**, 247-265.

[6] Boisdron, Y. and Brock, J. R. (1970) On the stochastic nature of the acquisition of electrical charge and radioactivity by aerosol particles. Atmospheric environment 4:35-50.

[7] Brasil, A. M., Farias, T. L., Carvalho, M. G. (1999) A recipe for image characterization of fractal-like aggregates. J Aerosol Sci 30:1379-1389.

[8] Brown, R. C. and Hemingway, M. A. (1995) Electric charge distribution and capacitance of agglomerates of spherical particles: theory and experimental simulation. J Aerosol Sci 26: 1197-1206.

[9] Brunauer, S., Emmett, P. H. and Teller, E. (1938) Adsorption of gases in multimolecular layers. J. Am Chem. Soc. 60, 309-319.

[10] Burtscher, H., Reis, A., and Schmidt-Ott, A. (1986) Particle Charge in Combustion Aerosols. J Aerosol Sci 17: 47-51.

[11] Cai, J., Lu, N., and Sorensen, C. M. (1993) Comparison of size and morphology of soot aggregates as determined by scattering and electron microscope analysis. Langmuir 9:2861-2867.

[12] Cai, J. and Sorensen, C.M. (1994) Diffusion of fractal aggregates in the free molecular regime, Phys. Rev. E. 50:3397-3400.

[13] Chan, P. and Dahneke, B. (1981) Free molecule drag on straight chains of uniform spheres. Journal of applied physics 52: 3106-3110.

[14] Chang, J.-S. (1981) Theory of diffusion charging of arbitrarily shaped conductive aerosol particles by unipolar ions. J Aerosol Sci 12: 19 -26.

[15] Chen, D. R. and Pui, D. Y. H.,(1999) A high efficiency , high throughput unipolar aerosol charger for nanoparticles. *Journal of Nanoparticle Research,* 1, 115-126.

[16] Cheng, Y.-S. and Yeh, H.-C. (1981) Equilibrium bipolar charge distribution of aerosols consisting of chains of uniform spheres. Journal of colloid and interface science 84:444-450.
[17] Cubley, S. J. and Mason, E. A. (1975) Atom-molecule and molecule-molecule potentials and transport collision integrals for high-temperature air species. Physics of fluids 1109:1111.
[18] Dahneke, B. E. (1973) Slip correction factors for nonspherical bodies-II free molecule flow. J Aerosol Sci 4:147-161.
[19] Davison, S. W. and Gentry, J. W. (1985). Differences in diffusion charging of dielectric and conducting ultrafine aerosols. Aerosol Sci. Technol. **4**, 157-163.
[20] Dixkens, J. and Fissan, H. (1999) Development of an electrostatic precipitator for off-line particle analysis. Aerosol Sci Technol 30:438-453.
[21] Donaldson, K., Li, X.Y. and MacNee, W. (1998) Ultrafine (nanometer) particle mediated lung injury. J. Aerosol Sci. 29(5-6), 553-560.
[22] Ehara, K., Hagwood, C., and Coalkey, K. J. (1996) Novel method to classify aerosol particles according to their mass-to-charge ratio-aerosol particle mass analyzer. J Aerosol Sci 27:217-234.
[23] Emery, Mark S. (2007) Theoretical Analysis of Data from DMA-APM System, Plan B Masters of Mechanical Engineering Project, University of Minnesota.
[24] Fissan, H. and Kuhlbusch, T. (2005) Strategies and instrumentation for nanoparticle exposure control in air at workplaces. 2nd International symposium on nanotechnology and occupational health, Minneapolis, USA, October 3-6, 2005.
[25] Fissan, H., Neumann, S., Trampe, A., Pui, D.Y.H., and Shin, W.G. (2007). Rationale and principle of an instrument measuring lung deposited nanoparticle surface area, *J. Nanoparticle Res.* 9: 53-59.
[26] Filippov, A. V. (1994) Charge distribution among non-spherical particles in a bipolar charging environment. J Aerosol Sci 25:611-615.
[27] Friedlander, S. K., Pui, D. Y. H. (2004) Emerging issues in nanoparticle aerosol science and technology. J Nanoparticle Res 6:313-320.
[28] Friedlander, S. K. and Wu, M. K. (1994) Linear rate law for the decay of the excess surface area of a coalescing solid particle. Physical review B 49**:** 3622-3624.
[29] Froeschke, S., Kohler, S., Weber, A. P., and Kasper, G. (2003) Impact fragmentation of nanoparticle agglomerates. J Aerosol Sci 34:275-287.
[30] Fuchs, N. A. (1963). On the stationary charge distribution on aerosol particles in bipolar ionic atomosphere. Geofis. Pura Appl., **56**,185-193.
[31] Fuchs, N. A. (1964) The mechanics of aerosols. New York: Macmillan.
[32] Gentry, J. W. (1972) Charging of aerosol by unipolar diffusion of ions. Journal of aerosol science 3:65-76.
[33] Gunn, R. (1954) Diffusion charging of atmospheric droplets by ions and the resulting combination coefficients. Journal of meteorology 11: 339-347.
[34] Gwaze, P., Schmid, O., Annegarn, H. J., Andreae, M. O., Huth, J., and Helas, G. (2006) Comparison of three methods of fractal analysis applied to soot aggregates from wood combustion. J. Aerosol Sci 37:820-838.

[35] Han, H. S., Chen, D. R., Anderson, B. E. and Pui, D. Y. H. (2000) A nanometer aerosol size analyzer (nASA) for rapid measurement of high concentration size distributions. J. Nanoparticle Research 2:43-52.
[36] Han, R. J. and Gentry, J. W. (1994) Evolution of charge distribution of non -spherical particles undergoing unipolar charging. Journal of aerosol science 25: 499-508.
[37] Hanel, G. (1977) Mean bulk densities of samples of dry atmospheric aerosol particles-summary of measured data. Pure and applied geophysics 115 : 799 -803.
[38] Hering, S. V., Flagan, R. C., Friedlander, S. K. (1978) Design and evaluation of a new low pressure impactor. 1. Environ Sci Technol 12: 667-673.
[39] Hering, S. V. and Stolzenburg, M. R. (1995) Online determination of particle size and density in nanometer size range. Aerosol science and technology 23:155-173.
[40] Heyder, J., Gebhart, J., Rudolf, G., Schillerd, C. F. and Stahlhofen, W. (1986) Deposition of particles in the human respiratory tract in the size range 0.005 -15μm. J. Aerosol Science 17, 811-825.
[41] Hinds, W. C. (1999) *Aerosol Technology*, Wiley, New York.
[42] Hirschfelder, J. O., Curtiss, C. F., and Bird, R. B. (1954) Molecular theory of gases and liquids. New York: Wiley.
[43] ICRP. (1994) International Commission on Radiological Protection Publication 66 Human Respiratory Tract Model for Radiological Protection. Oxford, Pergamon: Elsevier Science Ltd.
[44] James, A. C., Bailey, M.R. and Dorrian, M-D. (2000) LUDEP Software, Version 2.07: Program for implementing ICRP-66 Respiratory tract model. RPB, Chilton, Didcot, OXON. OX11 ORQ UK.
[45] Jullien, R. and Botet, R. (1987) Aggregation and fractal aggregates. Singapore: World Scientific Co Inc.
[46] Jung, H. J. and Kittelson, D. B. (2005) Characterization of aerosol surface instruments in transition regime. Aerosol Sci. Tech. 39 (9), 902-911.
[47] Kasper, G. (1982) Dynamics and measurement of smokes. I Size characterization of nonspherical particles. Aerosol science and technology 1:187-199.
[48] Katrinak, K. A., Rez, P., Perkes, P. R., and Buseck, P. R. (1993) Fractal geometry of carbonaceous aggregates from an urban aerosol. Environ Sci Technol 27:539-547.
[49] Kaufman, S.L., Medved, A., Pöcher, A., Hill, N., Caldow, R. and Quant, F.R. (2002) An electrical aerosol detector based on the corona-jet charger. AAAR conference (poster).
[50] Keller, A., Fierz, M,, Siegmann, K., Siegmann, H. C., and Filippov, A. (2001) Surface science with nonosized particles in a carrier gas. J. Vac. Sci. Technol. A 19:1-8.
[51] Kelly, W. P. and McMurry, P. H. (1992) Measurement of particle density by inertial classification of differential mobility analyzer-generated monodisperse aerosols. Aerosol science and technology 17:199-212.

[52] Kim, J. H., Mulholland, G. W., Kukuck, S. R., and Pui, D. Y. H. (2005) Slip correction measurements of certified PSL nanoparticles using a nanometer differential mobility analyzer (Nano-DMA) for Knudsen number from 0.5 to 83. Journal of research of the national institute of standards and technology 110:31-54.

[53] Kim, S. C., Wang, J., Emery, M. S., Shin, W. G., Mulholland, G.W. and Pui, D. Y. H. (2009) Structural Property Effect of Nanoparticle Agglomerates on Particle Penetration through Fibrous Filter. Aerosol science and technology 43:344-355.

[54] Kim, S. H., Mulholland, G. W., and Zachariah, M. R. (2007) Understanding ion-mobility and transport properties of aerosol nanowires. Journal of aerosol science 38:823-842.

[55] Kirsch, A. A. and Zagnit'ko, A. V. (1981) Diffusion charging of submicrometer aerosol particles by unipolar ions. Journal of colloid and interface science 80:111-117.

[56] Kittelson, D. B. (1998) Engines and nanoparticles: A review. Journal of aerosol science 29: 575-588.

[57] Knutson, E. O. and Whitby, K. T. (1975) Aerosol classification bye electrical mobility: apparatus theory and application. J Aerosol Sci 6:443 -451.

[58] Koch, W. and Friedlander, S. K. (1990) Particle growth by coalescence and agglomeration. Journal of aerosol science 21:S73-S76.

[59] Kousaka Y., Endo, Y., Ichitsubo, H., and Alonso, M. (1996) Orientation-specific dynamic shape factor for doublets and triplets of spheres in the transition regime. Aerosol science and technology. 24: 36-44.

[60] Koylu, U. O., Faeth, G. M., Farias, T. L., Carvalho, M. G. (1995) Fractal and projected structure properties of soot aggregates. Combustion Flame 100:621 -633.

[61] Ku, B. K. and Maynard, A. D. (2005) Comparing aerosol surface-area measurements of monodisperse ultrafine silver agglomerates by mobility analysis, transmission electron microscopy and diffusion charging. Journal of aerosol science 36: 1108-1124.

[62] Ku, B. K. and Maynard, A. D. (2006) Generation and investigation of airborne silver nanoparticles with specific size and morphology by homogeneous nucleation, coagulation, and sintering. J Aerosol Sci 37(4): 452 -470.

[63] Laframboise, J. G. and Chang, J. (1977) Theory of charge deposition on charged aerosol particles of arbitrary shape. J Aerosol Sci 8: 331-338.

[64] Lall, A. A., Friedlander, S. K. (2006) On-line measurement of ultrafine aggregate surface area and volume distributions by electrical mobility analysis: I. Theoretical analysis. J. Aerosol Sci 37: 260-271.

[65] Lall, A. A., Rong, W., Madler, L., Friedlander, S. K. (2008) Nanoparticle aggregate volume determination by electrical mobility analysis: Test of idealized aggregate theory using aerosol particle mass analyzer measurements. J Aerosol Sci 39: 403-417.

[66] Lall, A. A., Seipenbusch, M., and Friedlander, S. K. (2006) On-line measurement of ultrafine aggregate surface area and volume distributions by electrical mobility analysis: II. Comparison of measurements and theory. J Aerosol Sci 37:272-282.
[67] Lehtinen, K. E. J., Windeler, R. S., and Friedlander, S. K. (1996) A note on the growth of primary particles in agglomerate structures by coalescence. Journal of colloid and interface science 182: 606-608.
[68] Liu B.Y.H. and D.Y.H. Pui (1977) On unipolar diffusion charging of aerosols in the continuum regime. J. Colloid Interface Sci. 58, 142-149.
[69] Liu, B. Y. H, Whitby, K. T., and Yu, H. H. S. (1967) On the theory of charging of aerosol particles by unipolar ions in the absence of an applied electric field. Journal of colloid and interface science 23: 367-378.
[70] Mackowski, D.W. (2006) Monte Carlo simulation of hydrodynamic drag and thermophoresis of fractal aggregates of spheres in the free-molecule flow regime. Journal of aerosol science, 37: 242 – 259.
[71] Magnusson, M. H., Deppert, K., Malm, J.-O., Bovin, J.-O., and Samuelson, L. (1999) Gold nanoparticles: production, reshaping, and thermal charging. Journal of nanoparticle research 1:243-251.
[72] Mandelbrot, B. B. (1982) The fractal geometry of nature. San Francisco: Freeman.
[73] Marlow, W. and Brock, J. (1975). Unipolar diffusion charging of small aerosol -particles. J. Col. Int. Sci. 50, 32-38.
[74] Maynard A.D. (2003) Estimating aerosol surface area from number and mass concentration measurements. Annals of Occupational Hygiene 47, 123–144.
[75] Maynard A.D. and E.D. Kuempel (2005) Airborne nanostructured particles and occupational health. J. Nanoparticle Research 7(6), 587-614.
[76] McMurry, P. H., Wang, X., Park, K., and Ehara, K. (2002) The relationship between mass and mobility for atomospheric particles: A new technique for measuring particle density. Aerosol science and technology 36: 227-238.
[77] Meakin, P., Donn, B., and Mulholland, G. W. (1989) Collisions between point masses and fractal aggregates. Langmuir 5:510-518.
[78] Medved, A., Dorman, F., Kaufman, S. L. and Poecher (2000) A new corona -based charger for aerosol particles. J. Aerosol Sci. **31**, S616-S617.
[79] Megaridis, C. M. and Dobbins, R. A. (1990) Morphological description of flame-generated materials. Combustion Sci Technol 71:95-109.
[80] Mountain, R.D., Mulholland, G.W., and Baum, H.R. (1986) "Simulation of aerosol agglomeration in the free molecular and continuum flow regimes," J. of Colloid and Interface Science 114: 67-81.
[81] Nakamura, R. and Hidaka, Y. (1998) Free molecular gas drag on fluffy aggregates. Astron. Astrophys. 340: 329–334.
[82] Neimark, A. V., Koylu, O. U., and Rosner, D. E. (1996) Extended characterization of combustion-generated aggregates: Self-affinity and lacunarities. J Colloid and Interface Sci 180:590-597.

[83] Oberdorster G. (1996) Significance of particle parameters in the evaluation of exposure-dose-response relationships of inhaled particles. Particulate Sci. Technol. 14(2), 135-151.
[84] Oberdorster G., Gelein, R.M., Ferin, J. and Weiss, B. (1995) Association of particulate air pollution and acute mortality: involvement of ultrafine particles. Inhal. Tox. 7, 111-124.
[85] Oberdörster G., Oberdörster, E., and Oberdörster, J. (2005) Invited review: Nanotechnology: an emerging discipline evolving from studies of ultrafine particles. Environ Health Perspect 113(7), 823-839.
[86] Oh, C. and Sorensen, C. M. (1997) The effect of overlap between monomers on the determination of fractal cluster morphology. J Colloid and Interface Sci 193:17-25.
[87] Oh, H., Park, H., and Kim, S (2004) Effects of particle shape on the unipolar diffusion charging of nonspherical particles. Aerosol Sci Technol 38:1045 -1053.
[88] Okuyama, K., Kousaka, Y., Wu, J. J., Flagan, R. C., and Seinfeld, J. H. (1986) Production of ultrafine metal oxide aerosol particles by thermal decomposition of metal alkoxide vapors. AIChe Journal 32:2010-2019.
[89] Panish, M. B. (1961) Vapor pressure of silver. J. Chem. Eng. Data 6: 592-594.
[90] Park, K., Kittelson, D. B., and McMurry, P. H. (2004a) Structural properties of diesel exhaust particles measured by transmission electron microscope (TEM): relationships to particle mass and mobility. Aerosol science and technology. 38:881-889.
[91] Park, K., Kittelson, D. B., Zachariah, M. R., and McMurry, P. H. (2004b) Measurement of inherent material density of nanoparticle agglomerates. Journal of nanoparticle research, 6: 267-272.
[92] Pratsinis, S. E. (1998) Flame aerosol synthesis of ceramic powders. Progress in Energy and Combustion Science 24:197-219.
[93] Pui, D. Y. H. (1976) Experimental study of diffusion charging of aerosols. The University of Minnesota PhD thesis.
[94] Pui, D. Y. H., Fruin, S., and McMurry, P. H. (1988) Unipolar diffusion charging of ultrafine aerosols. Aerosol Sci. Technol. 8, 173-187.
[95] Qi, C., Asbach, C., Shin, W. G., Fissan, H., and Pui, D. Y. H. (2009) The effect of particle pre-existing charge on unipolar charging and its implication on electrical aerosol measurements. Aerosol Science and Technology, 43:232 -240.
[96] Rogak, S. N. and Flagan, R. C. (1992) Bipolar diffusion charging of spheres and agglomerate aerosol particles. J Aerosol Sci 23(7): 693-710.
[97] Rogak, S. N., Flagan, R. C., and Nguyen, H. V. (1993) The mobility and structure of aerosol agglomerates. Aerosol Sci Technol 18:25-47.
[98] Romay, F. J. and Pui, D. Y. H. (1992) On the combination coefficient of positive ions with ultrafine neutral particles in the transition and free-molecule regime. Aerosol Sci. Technol. 17, 134-147.
[99] Samson, R. J., Mulholland, G. W., and Gentry, J. W. (1987) Structural analysis of soot agglomerates. Langmuir 3:272-281.

[100] Scheibel, H. G. and Porstendorfer, J. (1983) Generation of monodisperse Ag -aerosol and Nacl-aerosol with particle diameters between 2-nm and 300-nm. J Aerosol Sci 14(2):113-126.
[101] Schmidt-Ott, A. (1988) New approaches to in situ characterization of ultrafine agglomerates. J Aerosol Sci 19: 553-563.
[102] Schwade, B. and Roth, P. (2003) Simulation of nano-particle formation in a wall -heated aerosol reactor including coalescence. J Aerosol Sci 34: 339–357.
[103] Shah, S. D. and Cocker, D. R. (2005). A fast scanning mobility particle spectrometer for monitoring transient particle size distributions. Aerosol Sci. Technol. **39**, 519-526.
[104] Shi, J. P., Harrison, R. M. and Evans, D. (2001) Comparison of ambient particle surface area measurement by epiphaniometer and SMPS/APS. Atmospheric Environment 35, 6193-6200.
[105] Shimada, M., Seto, T., and Okuyama, K. (1993) Thermophoretic and evaporational losses of ultrafine particles in heated flow. AIChE Journal 39:1859-1869.
[106] Shimada, M., Seto, T., and Okuyama, K. (1994) Size change of very fine silver agglomerates by sintering in a heated flow. Journal of chemical engineering of Japan 27:795-802.
[107] Shin, W. G., Mulholland, G. W., Kim, S. C., Wang, J., Emery, M. S., and Pui, D. Y. H. (2009a) Friction Coefficient and Mass of Silver Agglomerates in the Transition Regime. J Aerosol Sci 40:573-587.
[108] Shin, W. G., Mulholland, G. W., Kim, S. C., Wang, J., Emery, M. S., and Pui, D. Y. H. (2009c) Estimates of Non-ideal Effects on the Friction Coefficient of Agglomerates. Submitted to Journal of aerosol science.
[109] Shin, W. G., Pui, D. Y. H., Fissan, H., Neumann, S., and Trampe, A. (2007). Calibration and numerical simulation of nanoparticle surface area monitor (TSI Model 3550 NSAM). *Journal of Nanoparticle Research, 9*, 61-69.
[110] Shin, W. G., Qi, C., Wang, J., Fissan, H., and Pui, D. Y. H. (2009d) The effect of dielectric constant of materials on unipolar diffusion charging of nanoparticles. J Aerosol Sci 40:463-468.
[111] Shin, W. G., Wang, J., Mertler, M. Sachweh, B., Fissan, H., and Pui, D. Y. H. (2009b) Structural properties of silver nanoparticle agglomerates based on transmission electron microscopy: Relationship to particle mobility analysis. Journal of Nanoparticle Research, 11:163-173.
[112] Song, D. K., Lenggoro, I. W., Hayashi, Y., Okuyama, K., and Kim, S. (2005) Changes in the shape and mobility of colloidal gold nanorods with electrospray and differential mobility analyzer methods. Langmuir 21(23): 10375-10382.
[113] Stöber, W., Boose, C., and Prodi, V. (1974) Über die Orientierung und den dynamischen Formfaktor von kettenförmigen Aerosolteilchen in Ladungsspektrometern, Water, Air and Soil Pollution 3, 493.

[114] Tang, I. N., Munkelwitz, H. R. and Davis, J. G. (1977) Aerosol growth studies —II. Preparation and growth measurements of monodisperse salt aerosols. J. Aerosol Sci. 8(3), 149-159.
[115] Tence, M., Chevalier, J. P., Jullien, R. (1986) On the measurement of the fractal dimension of aggregated particles by electron microscopy : Experimental method, corrections and comparison with numerical models. J Physique 47:1989-1998.
[116] Vomela, R. A. and Whitby, K. T. (1967) The charging and mobility of chain aggregate smoke particles. Journal of colloid and interface science 25:568 -576.
[117] Wang, G.M. and Sorensen, C.M. (1994) Diffusive mobility of fractal aggregates over the entire Knudsen number range, Phys. Rev. E. 60:3036-3044.
[118] Weber, A. P., Baltensperger, U., Gaggeler, H. W., and Schmidt-Ott, A. (1996) In situ characterization and structure modification of agglomerated aerosol particles. J. Aerosol Sci 27:915-929.
[119] Weber, A. P. and Friedlander, S. K. (1997) In situ determination of the activation energy for restructuring of nanometer aerosol agglomerates. J Aerosol Sci 28:179-192.
[120] Wen, H. Y., Reischl, G. P., and Kasper, G. (1984a) Bipolar diffusion charging of fibrous aerosol particles-I. Charging Theory. J Aerosol Sci 15(2): 89-101.
[121] Wen, H. Y., Reischl, G. P., and Kasper, G. (1984b) Bipolar diffusion charging of fibrous aerosol-particles-II. Charge and electrical mobility measurements on linear chain aggregates. Journal of aerosol science. 15(2): 103-122.
[122] Wentzel, M., Gorzawski, H., Naumann, K. H., Saathoff, H., and Weinbruch, S. (2003) Transmission electron microscopical and aerosol dynamical characterization of soot aerosols. J Aerosol Sci 34:1347-1370.
[123] White, H. J. (1951) Particle charging in electrostatic precipitation. Transactions of American institute of electrical engineers 70:1186-1191.
[124] Wiedensohler, A. (1988) An approximation of the bipolar charge distribution for particles in the submicron size range," J Aerosol Sci 19, 387-389.
[125] Wilson, W. E., Han, H.-S., Stanek, J., Turner, J. and Pui, D. Y. H. (2003) The Fuchs surface area measured by charge acceptance of atmospheric particles may be a useful indicator of the quantity of particle surface area deposited in the lung. Abstracts of the European aerosol conference. S421-S422. Madrid, Spain.
[126] Wilson, W. E., Han, H.-S., Stanek, J., Turner, J., Chen, D.-R. and Pui, D. Y. H. (2004) Use of electrical aerosol detector as an indicator for the total particle surface area deposited in the lung. Symp. On air quality measurement methods and technology sponsored by air and waste management association. Research triangle park, NC. Paper #37.
[127] Woo, K.-S., Chen, D.-R., Pui, D. Y. H. and Wilson, W. E. (2001) Use of continuous measurements of integral aerosol parameters to estimate particle surface area. Aerosol Sci. Tech. 34, 57-65.

[128] Yang, H. H., Chien, S. M. , Lee, H. L., Chao, M. R., Luo, H. W., Hsieh, D. P. H., and Lee, W. J. (2007). Emission of trans, trans-2, 4-decadienal from restaurant exhaust to the atmosphere. Atmospheric Env. 41, 5327-5333.
[129] Zelenyuk, A. and Imre, D. (2007) On the effect of particle alignment in the DMA. Aerosol science and technology. 41(2): 112-124.

Appendix A. Calibration and Numerical Simulation of Nanoparticle Surface Area Monitor (TSI Model 3550 NSAM)

A.1. Introduction

Occupational health risks associated with the manufacturing and application of nanoparticles is one of the critical issues for nanotechnology development. Demands for nanomaterials are rapidly increasing and so especially workers may be exposed to specific harmful nanoparticles. Several recent studies have shown that the toxicity of inhaled nanoparticles may be more appropriately associated with particulate surface area (Oberdorster et al., 1995, 1996, 2005; Donaldson et. al, 1998; Maynard and Kuempel, 2005). Nanoparticles defined to be below 100nm have increasing surface area with decreasing particle size for the same amount of mass. From the viewpoint of nanoparticle toxicity, an instrument which measures nanoparticle surface area deposited in human lung is very desirable.

Relatively few techniques are available to monitor exposures with respect to aerosol surface area (Maynard, 2003; Jung and Kittelson, 2005; Shi et. al, 2001). The BET method based on a gas adsorption method is not suited for a rapid evaluation of aerosol surface area at lower concentration (Brunauer et al., 1938). It can be used only for powders, not for particles in the gasborne state. It does not have on-line capabilities. The first instrument designed to measure aerosol surface-area was the epiphaniometer

(Baltensperger et al., 1988). The epiphaniometer is not well suited to widespread use in the workplace because of the inclusion of radioactive source and the lack of effective temporal resolution. One of other possible methods is diffusion charging (DC). Instruments using DC include LQ1-DC diffusion charger (Matter Engineering, Switzerland) and TSI model 3070a Electrical Aerosol Detector (EAD). Those diffusion chargers were recently evaluated (Jung and Kittelson, 2005; Ku and Maynard, 2005). Several studies using atmospheric field data have shown that EAD can be used as a useful indicator of the quantity of particle surface area deposited in the lung (Woo et al., 2001; Wilson et al., 2003, 2004). Recently, it was found that response functions of EAD can be changed to match with particle surface area deposited in the lung through the adjustment of ion trap voltage in EAD (Fissan et al., 2005). Based on the observation, TSI Nanoparticle Surface Area Monitor (NSAM) model 3550 has been developed to measure the nanoparticle surface area deposited in two regions such as trancheobronchial (TB) and alveolar (A) of the human lung of a reference worker (Fissan et. al, 2007) through adjusting ion trap voltage. In all other cases such as kids and asthmatics errors will occur, which still have to be defined. NSAM provides a simple and fast solution for measuring the surface area dose in different parts of the inhalation system.

The schematic of NSAM is shown in Figure A-1. The major components of NSAM consist of a diffusion charger chamber, an ion trap, an electrometer filter, and other sharp bending parts to transport the nanoparticle stream. The total inlet flow rate of 2.5 lpm is divided into 1.5 lpm for aerosol and 1.0 lpm for sheath air surrounding a corona needle. In the charger chamber the aerosol stream and the ion stream opposing

each other are mixed. After a unipolar ion charging of atmospheric aerosols occurs in the charger chamber, the flow with a flow rate of 2.5 lpm enters the ion trap. Excess particles with high electrical mobility and ions are removed in the ion trap. Particles which penetrate the ion trap are collected by the electrometer filter. The delivered charges create a current, which is measured by electronic circuit.

Modifications of the Electrical Aerosol Detector (EAD) with different ion trap voltages have been tested with the goal of determining the deposited nanoparticle surface area for different regions of the human inhalation system (Fissan et al., 2005, 2007). The response function curve of EAD for an ion trap voltage of 100 V matched with TB deposition and an ion trap voltage of 200 V with A deposition.

This study consists of two parts. In the first part, response functions and calibration factors of NSAM for TB and A regions are experimentally obtained. The effects of particle materials and shape on the response function and calibration factor of NSAM are investigated. Also, both polydisperse and monodisperse tests are compared with each other using Ag particle agglomerates. In the second part, numerical simulation results for response function of NSAM are compared with experimental data.

A.2. Experimental

In order to obtain both response function and calibration curve of NSAM where the input is particle number concentration (N_{UCPC}) and the output (I) is electrometer current, a test facility was constructed to generate Ag particle agglomerates with an

electrical mobility size range from 7 to 100 nm (Figure A-2). Ag wire (purity level 99.9 %) was placed in a ceramic boat in the furnace. Nitrogen with a flow rate of 3.0 lpm was used as a carrier gas passing through the electric furnace. The flow rate of the carrier gas was regulated by combinations of needle valve, pressure gauge, and rotameter. Silver was vaporized in the electric furnace followed by particle formation by condensation and coagulation (Han et. al, 2000). Different experimental setup was added behind the electric furnace depending on monodisperse or polydisperse test. In monodisperse test Ag particles are introduced to both Ultra Condensation Particle Counter (UCPC) and NASM after primary particles were classified by a Differential Mobility Analyzer (DMA) set at a fixed voltage corresponding to particle size. In polydisperse test scanning mobility particle sizer (SMPS) and UCPC are used to measure particle size distribution and polydisperse Ag particles are directly introduced to NSAM after passing through a neutralizer. For all experiments, the carrier gas flow rate was fixed at 3.0 lpm. In order to change particle size distributions, the electric furnace temperature was varied from 950 ºC to 1200 ºC and the dilution flow using compressed nitrogen gas (1.0 lpm) was also introduced in front of UCPC and NSAM. Aerosol flow after the dilution was split into UCPC (1.5 lpm) and NSAM (2.5 lpm) flow. For the generation of monodisperse particles, particles larger than peak size of a given particle size distribution were subsequently selected with a DMA (Model 3080, TSI, Inc.). A Kr-85 neutralizer was used to get a defined charge distribution.

Experimental setup shown in Figure A-2 was modified to evaluate NSAM response using NaCl particles with a size range from 17 to 100 nm. A constant output atomizer (Model 3075, TSI, Inc.) was used to generate NaCl particles and pure and dry

air compressed at 37 psi was passed through the atomizer. In order to change particle size distributions, the concentration of NaCl solutions varied from 0.0001 g/cc to 0.01 g/cc. The flow rate from the atomizer was about 3.0 lpm. Aerosol flow was passed through diffusion dryer to get solid NaCl particles and then through a neutralizer to prevent particle loss due to highly charged status. In order to get higher monodispersity, primary particles larger than peak size of a given particle size distribution were subsequently selected with an electrostatic classifier (Model 3080, TSI, Inc.). In order to minimize the effect of humidity during the measurement, silica gel in diffusion dryer was regenerated frequently. The humidity was kept as low as 30~50 % during all experiments. Therefore, NaCl particles could not change in size during or after DMA classification (Tang et al., 1977). Splitting of aerosol flow rate after the dilution was the same as the case of Ag particle agglomerates.

The particle number concentration and electrometer current were simultaneously measured from UCPC and NSAM for all experiments using both Ag particle agglomerates and NaCl particles. The data integration time for all instruments was set to 2 minutes.

A.3. Normalized sensitivity and calibration factor of NSAM

For the NSAM, the input is particle number concentration (N_{UCPC}) and the output (I) is electrometer current. Therefore, the size dependent sensitivity (S) of NSAM is given by

$$S(d_m) = \frac{I(d_m)}{N_{UCPC}(d_m)}, \qquad \text{(A-1)}$$

where d_m is a particle diameter. All sensitivity data are normalized with respect to sensitivity for 100nm particles. In other words, the sensitivity for 100nm particles is used as a reference point. Normalized sensitivity (*NS*) is given by

$$NS(d_p) = \frac{S(d_m)}{S(100nm)} \quad . \qquad \text{(A-2)}$$

Calibration factor of NSAM is necessary to convert NSAM electrometer current signal into nanoparticle surface area deposited in human lung. Therefore, the calibration factor (*CF*) is given by

$$CF = \frac{Surface\ area\ deposited\ in\ human\ lung}{Electrometer\ current}, \qquad \text{(A-3)}$$

where *CF* has a unit of $\mu m^2/(cm^3 * pA)$.

A.4. Experimental results and discussion

Response function curves of NSAM for each d_m^2 weighted TB or A region are respectively shown (Figure A-3, Figure A-4). Response function curves are plotted in terms of the normalized sensitivity. It is very useful to determine how well a response function curve of NSAM is matched with an ideally wanted response function curve obtained from a theoretical lung deposition efficiency curve for TB or A region. The deposition efficiencies in TB and A regions (η_{TB} and η_A) were obtained using the UK National Radiological Protection Board's (NRPB's) LUDEP Software (James et. al,

2000), based on the recommendations of ICRP Publication 66 (ICRP, 1994). The lung deposition efficiency curves of spherical nanoparticles were derived for a reference worker (Fissan et. al, 2007). For particles below 100nm, particle density has no influence on the particle lung deposition efficiency curve because the dominant mechanism of particle lung deposition is only diffusion in the size range (Heyder et. al, 1986).

As shown in Figure A-3 and Figure A-4, experimental data are compared with Fissan et al. (2007)'s results for EAD because EAD is principally the same instrument as NSAM. For Ag particle agglomerates, the two experimental data sets show a good agreement with each other for both the TB and A regions. Response function curves of NSAM are well matched with those of the ideally wanted lung deposition efficiency curves for both TB and A regions. There is a small difference between Ag particle agglomerates and NaCl particles in terms of normalized sensitivity.

Even though Ag particle agglomerates below 10 nm show larger deviation from the ideally wanted response function curve in Figure A-3 and Figure A-4, it has no significant contribution to integrated surface area measurement deposited in human lung because of the d_m^2 dependency. The surface area contribution of a 10 nm particle is only 1 % of that of a 100 nm particle (Fissan et. al, 2007).

Calibration curve of NSAM for TB is plotted in Figure A-5. Calibration factor is considered as the fitted slope magnitude between the particle surface area deposited in human lung and the NSAM electrometer current. Using particle size measurement and

particle penetration efficiency, the particle surface area deposited in human lung (*DS*) is calculated by

$$DS(d_m) = \pi\, d_m^2\, \eta_l\,(d_m) \qquad \text{for monodisperse,}$$

$$DS = \Sigma\, \pi\, d_m^2\, \eta_l\,(d_m) \qquad \text{for polydisperse,} \qquad \text{(A-4)}$$

where $\eta_l\,(d_m)$ is particle lung deposition efficiency in TB or A region of human lung. As shown in Figure A-5, there exists a linear relationship between NSAM electrometer current signal and particle surface area deposited in human lung. However, there may be a small dependency of calibration factor on particle material. Calibration factors of NSAM for different parts of the inhalation system and different particle materials are summarized in Table A-1. The differences of calibration factors between Ag particle agglomerates and NaCl particles are below 13 % for both the TB and A regions. Several factors such as particle morphology, the change of particle size, and particle materials can have influence on this difference. But, it is believed that the first two factors have no influence on the difference of calibration factor in this experiment. Ku and Maynard (2005) showed that diffusion charging responses of the LQ1-DC (Matter Engineering, Switzerland) and DC2000CE (EcoChem, USA) were proportional to the mobility diameter squared, regardless of the morphology for monodisperse Ag particle agglomerates below 100 nm. Based on the result, the NSAM response for Ag particle agglomerates is assumed to be very close to that for spherical monodisperse Ag particle. Also, NaCl particles could not be changed in size during or after DMA classification because humidity was kept lower than the deliquescent point above which NaCl particles only can grow (Tang et al., 1977). Experimental data suggests that the

difference of 13% between Ag particle agglomerates and NaCl particle may be attributed to the small dependence on materials. The dielectric constant of the particle materials has a second order effect on particle charging rate (Liu and Pui, 1977).

Calibration result of NSAM using polydisperse Ag particles is in agreement with that of NSAM using monodisperse Ag particles for TB region (Figure A-6). It demonstrates the huge linear range of the instrument. It also demonstrates that polydisperse NaCl-aerosol can be more easily used for calibration. Therefore, it allows any monodisperse and polydisperse aerosol only in the size range where the response function is comparable with the needed response function to be used for the calibration purpose of NSAM for both the TB and A regions.

A.5. Numerical simulation results of NSAM flow path and discussion

Using a commercial CFD s/w Fluent 6.2, numerical simulations of fluid flow and particle trajectories inside NSAM were performed to estimate response functions of NSAM under different ion trap voltages. As shown in Figure A-1, there is a very complex geometry inside NSAM and an extremely complicated charging process involving turbulent mixing of airborne particles with unipolar ions produced from a corona needle inside NSAM. Therefore, the full geometry model of NSAM is too complex but simplified into flow path without the diffusion charger chamber. The simplified geometry model starts from the exit of charger chamber and ends in front of electrometer filter. It is assumed that the exit of the charger chamber exactly matches

with the inlet of ion trap part. Flow variables are uniform at the inlet boundary and the inlet velocity is 2.61 m/s. Navier-Stokes equations were solved using implicit solver in Fluent 6.2. The flow is in the laminar flow regime. The second order upwind scheme was used for the velocity equations.

Derivation of normalized sensitivity is necessary to compare experimental data with numerical simulation results. The current signal (I) measured by the electrometer filter inside NSAM in the experiment can be given by

$$I(d_p) = N_{in}(d_m)\, Q_{in}\, N_p\, e\, \eta_{tot}(d_m), \qquad \text{(A-5)}$$

where N_{in}: particle number concentration at the inlet of NSAM,

Q_{in} : total flow rate (2.5 lpm) entering into the inlet of NSAM,

N_p: particle mean charge level,

e: charge on an electron,

$\eta_{tot}(d_p)$: total penetration efficiency of particle in NSAM.

The mean charge level per delivered particle from diffusion charger in EAD (Medved et. al, 2000; Kaufman et al., 2002), which is proportional to particle diameter for the size range of 10 to 100 nm, was used in the Fluent simulations. Eq. (A-5) is substituted into Eq. (A-1) and then the sensitivity (S) can be given by

$$S(d_m) = \frac{N_{in}(d_m)\, Q_{in}\, N_p\, e\, \eta_{tot}(d_m)}{N_{in}(d_m)} = Q_{in}\, N_p\, e\, \eta_{tot}(d_m). \qquad \text{(A-6)}$$

Eq. (A-6) is substituted into Eq. (A-2) and then the normalized sensitivity (NS) can be given by

$$NS(d_m) = \frac{Q_{in}\, N_p(d_m) e\, \eta_{tot}(d_m)}{Q_{in}\, N_p(100nm)\, e\, \eta_{tot}(100nm)} = \frac{N_p(d_m)}{N_p(100nm)} \frac{\eta_{tot}(d_m)}{\eta_{tot}(100nm)} \quad . \qquad \text{(A-7)}$$

The normalized sensitivity is expressed as the ratio of mean charge levels multiplied by that of total penetration efficiencies. Total penetration efficiency can be given by

$$\eta_{tot}(d_m) = \eta_{flowpath}(d_m) \times \eta_{charger}(d_m), \qquad \text{(A-8)}$$

where $\eta_{flowpath}(d_m)$ is flow path penetration efficiency and $\eta_{charger}(d_m)$ is charger chamber penetration efficiency of particles in NSAM.

Eq. (A-8) is substituted into Eq. (A-7) and then the normalized sensitivity is given by

$$NS(d_m) = \frac{N_p(d_m)}{N_p(100nm)} \frac{\eta_{flowpath}(d_m)}{\eta_{flowpath}(100nm)} \frac{\eta_{charger}(d_m)}{\eta_{charger}(100nm)}. \quad \text{(A-9)}$$

If the ratio of charger chamber penetration efficiencies in the Eq. (A-9) is assumed to be equal to 1, the normalized sensitivity (*NS*) is simplified by

$$NS(d_m) = \frac{N_p(d_m)}{N_p(100nm)} \frac{\eta_{flowpath}(d_m)}{\eta_{flowpath}(100nm)}. \quad \text{(A-10)}$$

The flow path penetration efficiency in Eq. (A-10) was obtained through particle trajectory calculations using Fluent discrete phase model. The effect of Brownian motion was included in the simulations. Ag particles used in Fluent simulations are in the range of 10 to 100 nm. In order to investigate electrophoresis effect, user defined subroutine was run at the same time during Fluent calculation. It adds electric force to the existing body force term of discrete phase model in Fluent and thus enables the application of electric field on the ion trap part. It also makes particles injected from the inlet boundary have mean charge level proportional to particle size. In each particle

trajectory calculation, 1000 spherical Ag particles which have the same size were released from the inlet boundary surface of the model and each particle has the mean charge level proportional to particle size. Material properties of Ag have the density of 10.5 kg/m^3, the thermal conductivity of 429 W/mK, and the specific heat of 235 J/kg-K. The flow path penetration efficiency was calculated by dividing the number of particles arriving at the end point by the number of injected particles for each particle size. For each particle size, the procedure of particle trajectory calculation was repeated over 20 times to get more exact value. The normalized sensitivity was obtained by multiplying the ratio of flow path penetration efficiency determined from numerical simulations by that of mean charge level as shown in Eq. (A-10).

A comparison of response function curves obtained by Fluent simulation and experimental measurement can be found in Figure A-3 and Figure A-4. Fluent simulation results are relatively well matched with experimental results in the size range between 10 and 100 nm. Because particles range below 10nm do not contribute to particle surface area deposited in human lung, the particles were not modeled. Normalized sensitivity estimated by Fluent simulation is larger than that obtained by experimental measurement in both cases of TB and A regions. The deviation between the model and the experimental results points to the importance of the charger chamber for the whole system. With the next version of the model the effects within the charger chamber will be modeled.

A.6. Conclusions and discussion

The response functions and calibration factors of a modified EAD, the TSI Model 3550 Nanoparticle Surface Area Monitor (NSAM), have been experimentally investigated for the measurement of nanoparticle surface area deposited in the human lung. Also, normalized sensitivity of NSAM have been analytically derived to compare experimental data with numerical simulation results and have investigated the usefulness of numerical simulation results as well.

NSAM shows a linear relationship between the particle surface area deposited in human lung and the electrometer current for both TB and A regions of a reference worker. The results look promising in that NSAM gives a real-time quantitative measurement of particle surface area deposited the human lung and thus can be used to correlate with epidemiological studies for nanoparticles below 100 nm. From the experimental data, there is little dependency of response function curves of NSAM on particle materials. Also, the NSAM calibration factors for both the TB and A regions show small dependency on particle materials. The differences between Ag particle agglomerates and NaCl particles are below 13%. For calibration monodisperse nanoparticles in the size range where the response function is comparable with the needed response function, but also more practically polydisperse nanoparticles can be used.

Fluent simulations results matched reasonably well with experimental results in terms of response function. It demonstrates that Fluent simulation can be used to optimize the NSAM response qualitatively. However, in order to get more exact results quantitatively from numerical simulation, the charger chamber penetration efficiency

also needs to be considered in the numerical simulations. Furthermore, it is suggested that modification of ion trap configurations can be considered to improve the matching response function of NSAM with ideally wanted response function curve.

Region	Ag	NaCl
TB	83.97	95.67
A	385.24	422.68

Table A-1. Summary of calibration factors ($\mu m^2/(cm^3 * pA)$) of NSAM

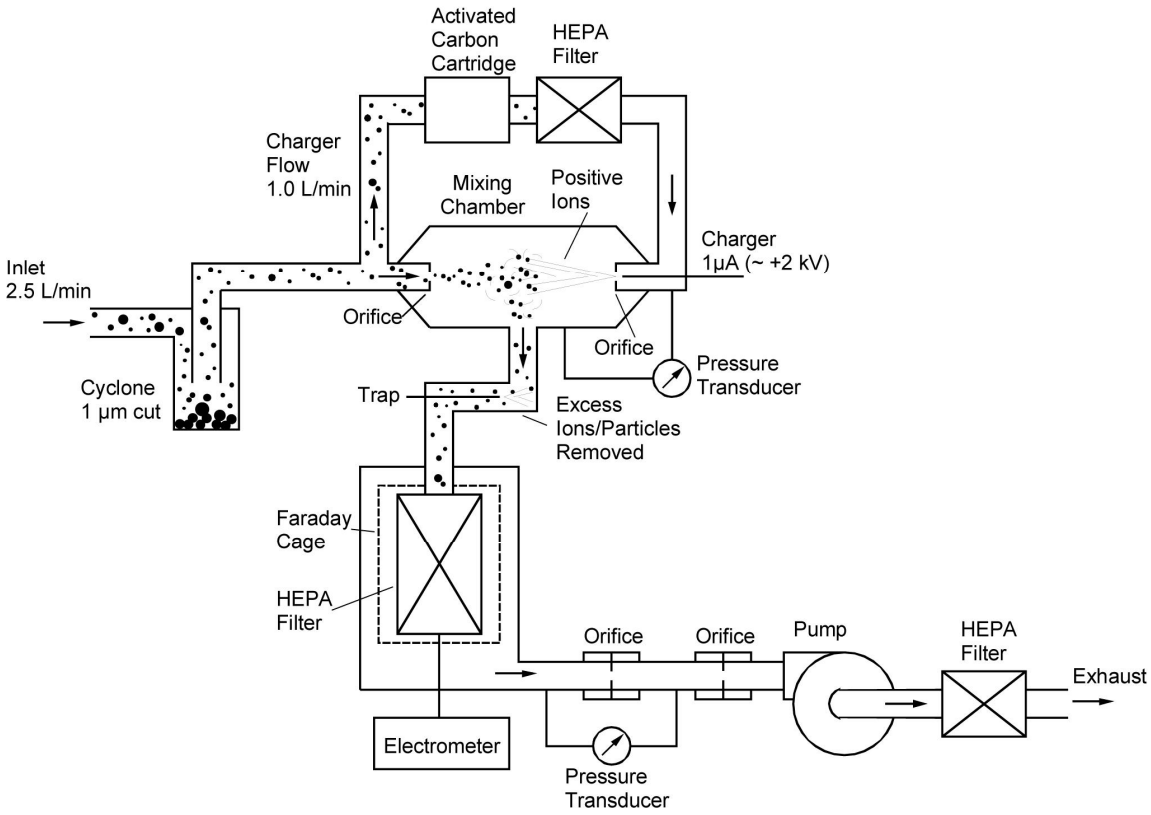

Figure A-1.The schematic of NSAM

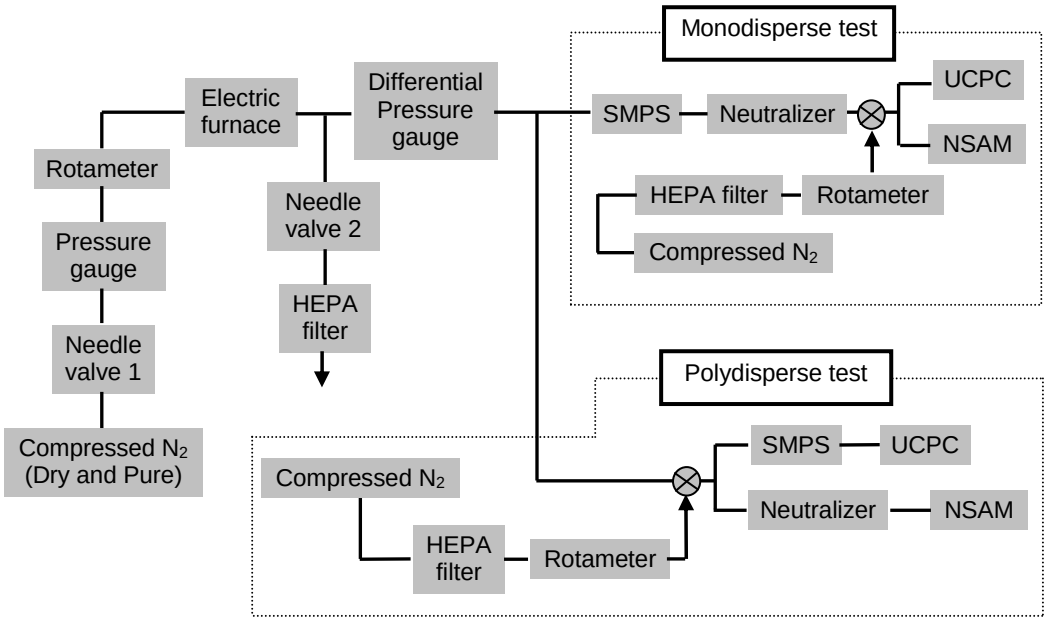

Figure A-2. Experimental setup to evaluate NSAM response using monodisperse or polydisperse Ag particle agglomerates.

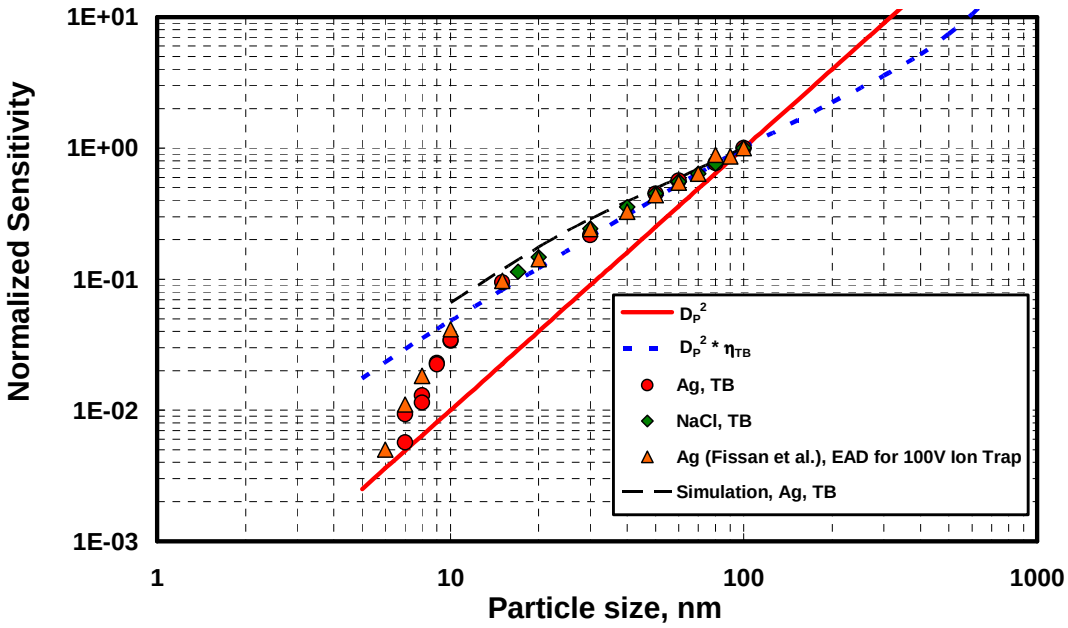

Figure A-3. Comparison of response function curves of NSAM for TB region

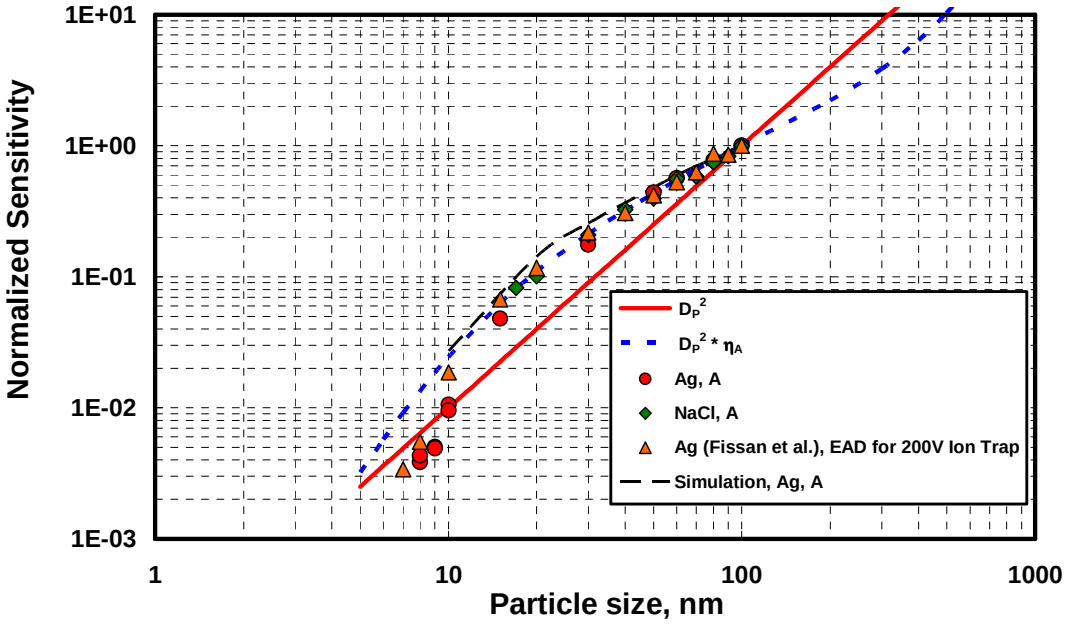

Figure A-4. Comparison of response function curves of NSAM for A region

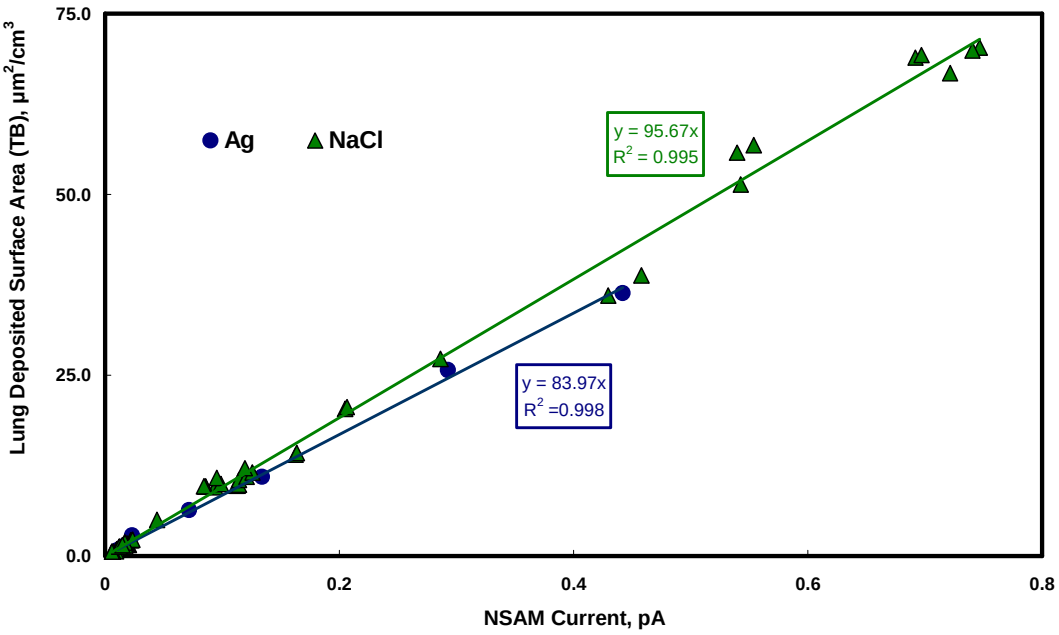

Figure A-5. Calibration factor of NSAM for TB region

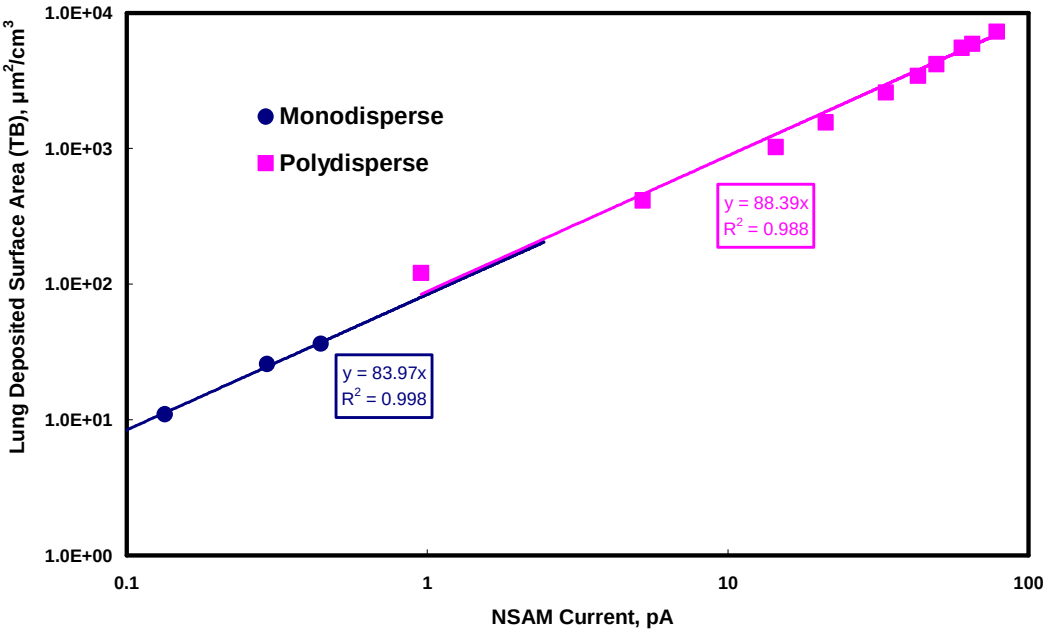

Figure A-6. Comparison of calibration factors of NSAM for TB region using polydisperse and monodisperse Ag particle agglomerates.

Appendix B. List of Publications and Copyright Permissions

B.1. List of publications used in this thesis

Chapter 2: W. G. Shin, J. Wang, H. Fissan, and D. Y. H. Pui "Structural Property of Silver Nanoparticle Agglomerates Based on Transmission Electron microscopy: Relationship to Particle Mobility Analysis," Journal of Nanoparticle Research, 11:163-173, 2009.

Chapters 3 and 4: W. G. Shin, G. W. Mulholland, S. C. Kim, J. Wang, M. S. Emery, and D. Y. H. Pui Friction coefficient and mass of silver agglomerates in the transition regime. J Aerosol Sci 40:573-587.

Chapter 5: W. G. Shin, G. W. Mulholland, S. C. Kim, J. Wang, M. S. Emery, and D. Y. H. Pui Estimates of non-ideal effects on the friction coefficient of agglomerates" submitted to J Aerosol Sci 2009.

Chapter 6: W. G. Shin, G. W. Muholland, and D. Y. H. Pui, "Determination of Volume, Mass Mobility Diameter Scaling Exponent, and Particle Alignment of Nanoparticle Agglomerates using TDMA Method" submitted to Journal of aerosol science.

Chapter 7: W. G. Shin, C. Qi, J. Wang, H. Fissan, and D. Y. H. Pui (2009), "The effect of dielectric constants of materials on the unipolar diffusion charging of nanoparticles" J Aerosol Sci 40:463-468.

Chapter 8: W. G. Shin, J. Wang, H. Fissan, and D. Y. H. Pui, "The effect of particle morphology on unipolar diffusion charging of nanoparticle agglomerates in the transition regime" submitted to Journal of aerosol science.

Appendix A: W.G. Shin, D.Y.H. Pui, Fissan H, S. Neumann, and A. Trampe "Calibration and Numerical Simulation of Nanoparticle Surface Area Monitor (TSI Model 3550 NSAM)," J. Nanoparticle Research, 9:61-69, 2007.

B.2. Copyright permission for the reprint of Chapter 2

This is a License Agreement between Weon Gyu shin ("You") and Springer ("Springer") provided by Copyright Clearance Center ("CCC"). The license consists of your order details, the terms and conditions provided by Springer, and the payment terms and conditions.

All payments must be made in full to CCC. For payment instructions, please see information listed at the bottom of this form.

License Number: 2152610731923
License date: Mar 19, 2009
Licensed content publisher: Springer
Licensed content publication: Journal of Nanoparticle Research
Licensed content title: Structural properties of silver nanoparticle agglomerates based on transmission electron microscopy: relationship to particle mobility analysis
Licensed content author: Weon Gyu Shin
Licensed content date: Jan 1, 2009
Volume number: 11, Issue number: 1, Pages: 163 - 173
Type of Use Thesis / Dissertation
Details of use: Print
Requestor Type: Individual
Portion of the article: Full text
Title of your thesis / dissertation: Mechanics and Charging of Nanoparticle Agglomerates
Expected completion date: May 2009

B.3. Copyright permission for the reprint of Chapters 3 & 4

License Number: 2205180528024
License date: Jun 10, 2009
Licensed Chapter Title:
Licensed Chapter ID:
Licensed content publisher: Elsevier
Licensed content publication: Journal of Aerosol Science
Licensed content title: Friction coefficient and mass of silver agglomerates in the transition regime
Licensed content author: W.G. Shin, G.W. Mulholland, S.C. Kim, J. Wang, M.S. Emery and D.Y.H. Pui
Licensed content date: July 2009
Volume number: 40
Issue number: 7
Pages: 15
Type of Use: Thesis / Dissertation
Portion: Full article
Format: Both print and electronic
You are the author of this Elsevier article: Yes
Are you translating? No
Order Reference Number:
Expected publication date: Jun 2009
Elsevier VAT number: GB 494 6272 12
Billing type: Invoice

Company: Weon Gyu shin
Billing address: Department of Mechanical Engineering, The University of Minnesota , Minneapolis, MN 55414 United States
Customer reference info:
Permissions price: 0.00 USD
Value added tax 0.0%: 0.00 USD
Total: 0.00 USD

B.4. Copyright permission for the reprint of Chapter 7

This is a License Agreement between Weon Gyu shin ("You") and Elsevier ("Elsevier") provided by Copyright Clearance Center ("CCC"). The license consists of your order details, the terms and conditions provided by Elsevier, and the payment terms and conditions.

All payments must be made in full to CCC. For payment instructions, please see information listed at the bottom of this form.

Supplier: Elsevier Limited The Boulevard,Langford Lane
Kidlington,Oxford,OX5 1GB,UK
Registered Company Number: 1982084
Customer name: Weon Gyu shin
Customer address: Department of Mechanical Engineering, Minneapolis, MN 55414
License Number: 2205180110943
License date: Jun 10, 2009
Licensed content publisher: Elsevier
Licensed content publication: Journal of Aerosol Science
Licensed content title: The effect of dielectric constant of materials on unipolar diffusion charging of nanoparticles
Licensed content author: Weon Gyu Shin, Chaolong Qi, Jing Wang, Heinz Fissan and David Y.H. Pui
Licensed content date: May 2009
Volume number: 40
Issue number: 5
Pages: 6
Type of Use: Thesis / Dissertation
Portion: Full article
Format: Both print and electronic
You are an author of the Elsevier article: Yes
Are you translating? No
Order Reference Number:
Expected publication date: Jun 2009
Elsevier VAT number: GB 494 6272 12
Permissions price: 0.00 USD

Value added tax 0.0%: 0.00 USD
Total: 0.00 USD

B.5. Copyright permission for the reprint of Appendix A

SPRINGER LICENSE
TERMS AND CONDITIONS

Mar 19, 2009

This is a License Agreement between Weon Gyu shin ("You") and Springer ("Springer") provided by Copyright Clearance Center ("CCC"). The license consists of your order details, the terms and conditions provided by Springer, and the payment terms and conditions.

All payments must be made in full to CCC. For payment instructions, please see information listed at the bottom of this form.

License Number: 2152610090006
License date: Mar 19, 2009
Licensed content publisher: Springer
Licensed content publication: Journal of Nanoparticle Research
Licensed content title:
Calibration and numerical simulation of Nanoparticle Surface Area Monitor (TSI Model 3550 NSAM)
Licensed content author: W. G. Shin
Licensed content date: Jan 1, 2007
Volume number: 9, Issue number: 1, Pages: 61 - 69
Type of Use: Thesis / Dissertation
Details of use: Print
Requestor Type: Individual
Portion of the article: Full text
Title of your thesis / dissertation: Mechanics and Charging of Nanoparticle Agglomerates
Expected completion date: May 2009